TECHNISCHE UNIVERSITÄT WIEN

LOW-TEMPERATURE CO-FIRED CERAMIC-BASED COILS IN PROBE HEADS FOR NUCLEAR MAGNETIC RESONANCE SPECTROMETRY

Dissertation

ausgeführt zum Zwecke der Erlangerung des akademischen Grades eines Doktors der technischen Wissenschaften von

Pero Krivić
Matr. No. 1128846

eingerichtet an der Technischen Universität Wien
Fakultät für Elektrotechnik und Informationstechnik

Oktober 2015

Abstract

Over the last few decades, nuclear magnetic resonance (NMR) has had a tremendous impact on research in physics, chemistry, biology and medicine. Although this invaluable technique for quantitative structure analysis, NMR spectrometry suffers from an inherent lack of sensitivity compared to other popular analytical techniques like fluorescence and mass spectrometry or electron spin resonance. The sensitivity of the NMR spectrometer is defined through the signal-to-noise ratio (*SNR*) and is dependent on sample conditions and spectrometer parameters. One decisive parameter for the sensitivity improvement of the NMR experiment is the quality of the sensing element of the spectrometer - a coil in the probe head.

Low temperature co-fired ceramics (LTCC) offer prototyping and rapid development of various passive electronic components and, thanks to an inherent low dielectric loss of the ceramic and applicability of highly conductive silver, it is a technology of choice for the development of high quality radio frequency inductors. The possibility to fabricate multi-layered three dimensional structures, the remarkable electrical and thermo-mechanical properties of LTCC make this material desirable for the production of the coils suited for NMR experiments. This thesis deals with the optimization of the coil design for given NMR samples.

The optimization starts with a mathematical description of the field generated by the coil and an attempt to get the end result - the *SNR* of the experiment in an analytical expression. Further analysis by means of finite element method simulations delivers a deeper insight in coil's properties as for instance inductance, quality factor, field homogeneity and self-resonant frequency. All these features are used to get the geometrical parameters of the coil in terms of diameter, track width, or number of windings for which the coil yields the best possible NMR sensitivity.

After thorough analysis the various sets of coils are produced in the Laboratory for Ceramic Technology, characterized electrically and employed in the NMR spectrometer. The production of the coils tested the limits of established LTCC technology for both large and small dimensioned structures were successfully fabricated. Coil characterization and NMR measurements confirmed the predictions from theoretical analysis. A high frequency coil with a nano-liter sample volume was tested in the NMR spectrometer and yielded an *SNR* convincingly higher than the copper wire coil that is usually used for this purpose. The extreme working conditions, such as temperatures as low as 80 K and voltages of few kilovolts have proven superiority of LTCC for this application.

Contents

List of Symbols and Abbreviations

Abbreviations

2D	Two-dimensional
3D	Three-dimensional
FEM	Finite element method
FFT	Fast Fourier transform
FID	Free induction decay
HTCC	High temperature co-fired ceramics
LTCC	Low temperature co-fired ceramics
MEMS	Micro-electro-mechanical system
MUMPS	Multifrontal massively parallel sparse direct solver
Nd:YAG	Neodymium-doped yttrium aluminum garnet
NMR	Nuclear magnetic resonance
NQR	Nuclear quadrupolar resonance
PARADISO	Parallel direct sparse solver
PET	Polyethylene terephthalate
RF	Radio frequency
SMA	SubMiniature version A radio frequency connector
SNR	Signal-to-noise ratio
SNR_{puv}	Signal-to-noise ratio per unit volume

Chemical formulæ

Al_2O_3	Aluminum (VI) oxide or *alumina*
B_2O_3	Boron (VI) oxide
BaO	Barium (II) oxide
CaO	Calcium (II) oxide
CuO	Copper (II) oxide
K_2O	Potassium oxide
Na_2O	Sodium oxide
SiO_2	Silicon (IV) oxide or *silica*
ZnO	Zinc (II) oxide
ZrO_2	Zirconium (IV) oxide or *zirconia*

Physical constants

e	Electron charge	$1.602 \times 10^{-19}\,\mathrm{C}$
ε_0	Electrical permitivtty of the free space	$8.854 \times 10^{-12}\,\mathrm{F/m}$
γ	Gyromagnetic ratio	for Cu $11.25\,\mathrm{MHz/T}$
$\hbar$	Reduced Planck constant	$1.054 \times 10^{-34}\,\mathrm{J\,s}$
k_B	Boltzmann constant	$1.380 \times 10^{-23}\,\mathrm{J/K}$
μ_0	Magnetic permeability of the free space	$4\pi \times 10^{-7}\ \mathrm{Tm/A}$

Symbols

A	Surface	m^2
B_0	Static magnetic field	T
B_1	RF magnetic field of the coil	T
$\hat{B_1}$	RF magnetic field produced by the unit current	T/A
C	Capacitance	F
d	distance	m
η	Filling factor	-
F	Noise figure	-
f	Frequency	Hz
I	Spin quantum number	-
I	Electrical current	A
k_0	Homogeneity factor	-
L	Inductance	H
M	Magnetization	A/m
M_0	Magnetization in thermal equilibrium	A/m
M_z	Longitudinal magnetization component	A/m
M_{xy}	Transversal magnetization component	A/m
N	Number of layers	-
N_s	Number of spins	-
m	Magnetic moment	$\mathrm{A/m}^2$
Q	Quality factor	-
Q_{ij}	Quadrupole moment tensor	$\mathrm{C\,m}^2$
ρ	Electrical resistivity	$\Omega\,\mathrm{m}$
ρ_n	Nucleus charge density	$\mathrm{C/m}^3$
R	Electrical resistance	Ω
R	Coil radius	m
r, θ, z	Polar coordinates	m, rad, m
R_S	Surface electrical resistance	Ω
T	Temperature	K
$\tan\delta$	Dielectric loss	-
V	Volume	m^3
w	Track width	m
x, y, z	Distances in Cartesian coordinates	m
ω	Frequency	rad/s
ω_0	Larmor frequency	rad/s

Chapter 1

Introduction

Nuclear magnetic resonance (NMR) is a phenomenon that has deeply changed the way we approach the study of nature. Originating at the very core of basic natural elements, it provides plentiful information about the inter- and intra molecular interactions that are central to many chemical and biological processes. The basic principle of NMR analysis is the excitation of the nuclear magnetic dipoles within the sample. The nuclear magnetic momenta, placed in a static magnetic field, are excited by means of electromagnetic radiation in which their quantum state is changed. Once excited, the nucleus falls back to its initial energy state, radiating excessive energy. The radiation is an electromagnetic wave in the range of radio frequencies and can be picked up using standard radio frequency detection techniques, such as a heterodyne receiver. The sensing element of the receiver is most often an inductor, a single copper wire coil.

This coil has been subject to many investigations throughout decades since the discovery of the NMR phenomenon in 1940-s. Optimization in fabrication of the copper coil improved sensitivity of the receiver and gained increase in information obtained from the NMR. In this thesis, for the first time, analysis, production and application of the NMR coils have been carried out in ceramic technology that has proven to be promising for radio-frequency components - the low-temperature co-fired ceramics, or LTCC.

State-of-the-Art in NMR Spectrometry

NMR spectrometry is a tool for analysis of many biological and chemical samples which is based on sensing extremely low electromagnetic fields. For a long time the sensing element was a simple solenoid coil wound around the sample, and its properties were taken for granted. The noise generated by the coil presents the limits of the coil usability and it were D.I. Hoult and R. E. Richards who were first to lay out the analysis of the sensitivity of the simple solenoid and saddle coils in [1] in 1980s. Using the so called *principle of reciprocity*, they managed to express the signal to noise ratio of the coil in dependence on its geometrical parameters. In 1994 T. Peck, R. Magin and P. Lauterbur presented an analysis of skin and proximity effects on the solenoidal coil as a limiting factor to the sensitivity [2]. Peck and Magin later turned to integrated NMR systems on a chip, while Lauterbur proceeded in developing the first NMR imaging tool, for which he was awarded the Nobel prize in 2003. Another notable work on signal-to-noise calculation was extensively and in pure mathematical language provided by H. Vesselle and R. Collin [3, 4].

Although the NMR is a valuable analytical technique, it suffers from an inherent lack of sensitivity compared to other popular analytical techniques like fluorescence and mass spectrometry or electron spin resonance. Sensitivity of the NMR spectrom-

eter is defined through two figures, one is the signal-to-noise ratio of the receiver and the other is the spectral resolution or the linewidth. For a given receiver bandwidth, temperature, sample volume and concentration, nuclear species and magnet strength, the *SNR* per unit volume (SNR_{puv}) of the RF coil is proportional to:

$$SNR_{puv} \propto \frac{\hat{B}_1}{\sqrt{R}}.$$

where $\hat{B}_1$ is magnetic field within the coil produced by a unit current and R is the coil's ohmic resistance. These are the key technical design parameters of the coil that can be manipulated to improve the signal to noise ratio. This translates to the question of choosing the proper coil geometry for any given sample. Keeping that in mind, the optimization of the coil geometry reduces to maximizing the *SNR* per unit volume.

This is where the LTCC made coils come in handy. This versatile technology enables production of the mechanically stable, reproducible, low-loss coils with variable geometry parameters that can be well adapted to various NMR samples. The possibility of integrating additional RF-circuit elements makes design of fully packed NMR probe heads in a single ceramic substrate viable.

Radio-frequency sensors and components in LTCC

Low-temperature co-firing is a material processing technique that creates electronic and mechanical structures by converting thin, flexible mixture of the ceramic powder and plasticizer into the firm ceramic substrate called a *low-temperature co-fired ceramic*, or LTCC. The substrate formation is obtained by sintering different kinds of ceramic and metal materials at temperatures of up to 900 °C. LTCC technology evolved from HTCC (high-temperature co-firing ceramics) and introduced possibility of using materials such as silver or gold, which, due to the evaporation, can not be used in HTCC where sintering processes require the temperatures above 1100 °C.

Over the last two decades, the LTCC technology has shown to be stupendously valuable in sensor production, especially with the sensors dealing in radio-frequency signals [5, 6]. Its multi-layering feature and interconnection capabilities allow us to design passive components down to the micro-scale level [7]. Low dielectric losses of the ceramic substrates made it possible for high quality micro-sized inductors and capacitors to emerge on the scene, and compatibility with different resistive pastes put up a scene for various resistor designs for both radio frequency and microwave bands [8, 9] and [10]. Design of microwave components was based on screen-printing circuit elements on the dielectric substrate. This way, filters with distributed parameters could be produced. The LTCC process is compatible with the magnetic materials (ferrites). High inductance inductors with the ferrite cores also developed in LTCC technology have been reported and are finding their way to the market in the scope of the work at the Vienna University of Technology: some were either planar [11, 12] or three-dimensional [13]. High mechanical and thermal stability put a trend to use LTCC substrate as a wafer for the solid-state chip packages including power amplifiers or high-power transmitters ([14, 15] and [16]). Thermal management by the use of thermal vias in LTCC is a well-established technique, and liquid cooling channels in the LTCC substrate provide efficient additional means for high-power device cooling. When targeting for thermally controlled systems, thermal bridge structures can be used to isolate critical devices from the main structures.

Various other sensor types have been successfully produced in LTCC technology. Capacitive pressure sensors have been designed and manufactured at the Vienna University of Technology by W. Smetana, G. Radosavljević, M. Unger and others [17, 18], as well as in other research groups [19, 20]. In all of these designs of

a great value was a property of LTCC to produce cavities within a dielectric by stacking multiple layers of un-fired tape. Some of these sensors ([18]) use the resonant behavior of LTCC based LC-circuits to wirelesslly readout the value of the sensing element. Again, the possibility of multi layered structures enables production of the fine micro-channels on the sub-millimeter scale for micro-fluid measurements. Usage of LTCC based sensors in micro-fluidic applications have been shown by W. Smetana, I. Atassi and B. Balluch [21], [22] at the same department in Vienna. Of special interest was usage of piezoelectric effects of ceramic crystals such as ZrO_2 for design of force sensors [23, 24]. LTCC is often used as a packaging and sealing substrate for different sensors. It has successfully served as a package for *micro electro-mechanical systems* or MEMS [25], gas sensing [26] or surface acoustic wave measuring [27] applications. Combining LTCC with some of the industrially available polymer based pastes will provide inherently hermetic substrate allowing the possibility of hermetic encapsulation [25].

Objectives and outlines

After looking onto the previously listed characteristics of LTCC appliances and the needs in NMR sensor attributes, it is reasonable to expect that multiple benefits may be extracted by introducing LTCC based coils in NMR spectrometry. The objective of this PhD thesis is to design, develop, produce and characterize coils in LTCC technology that might be employed in NMR spectrometers. Chapter 2 gives a basic introduction into the principles underlying phenomenon of NMR and its measuring techniques. Most importantly, it shows what is necessary to perform a valid NMR experiment and how sensor performance influence the obtained data. A special branch of NMR, called nuclear quadrupole resonance, or NQR has been exploited for the purpose of this thesis and is also briefly discussed.

Chapter 3 gives an overview of the LTCC technology in order to understand its potentialities and limitations. It presents material characteristics and manufacturing details that are gathered in the decade-long work at the Institute of Sensor and Actuator Systems. The chapter also tries to explain which available materials (tapes and pastes) are most suitable for the intended purpose.

Chapter 4 kicks off the coil design with the three dimensional, so called *quasi-solenoidal* coil. This coil is made by stacking many via-connected layers of LTCC tape, where semi-circular track is printed. The overall achievement is the solenoid where each half turn comes in discrete steps, instead continuously as in conventional solenoid. A variation of this coil is the spiral 3D coil, where each layer consists of Archimedean type of the spiral instead of the semi-circular track. Additional coil types presented in this chapter are surface spiral coil, twin horseshoe coil which are actually built-in resonators designed as stacked, oppositely looking horseshoes, and a system of four spiral coils designed to achieve circularly polarized magnetic field within the sample placed above them. Using mathematical analysis (Biot-Savart law) backed by the *Matlab* computational tool, I'll try to present coil characteristics in dependence on its geometry parameters (number of layers, track width, inner diameter, spacing between the layers, etc.). This analysis will try to answer the question: which coil parameters give the best (optimum) performances in NMR experiment? How to design coil with the highest possible signal-to-noise ratio for the given sample? How will the inductance and quality factor of the coil depend on these parameters. The calculation is verified by the FEM simulation, performed in *Comsol Multiphysics* software.

In chapter 5 the coil production and characterization with the network analyzer are laid out. Details of the production are given in order to fully understand the difficulties encountered on the way of coil fabrication. The coils were produced in the size of few millimeters to few centimeters and this variety in size made it necessary

to investigate different fabrication approaches. Fabrication analysis is also given in form of discussion of microscopically observed samples. The fabricated coils were electrically characterized with the vector network analyzer and fitting of measured values to the analytical model from chapter 5 is examined.

Final NMR measurements are presented in chapter 6. A brief overview of the measuring equipment is given. The measurements are performed at the Karl Franzens University in Graz, in a broad band solid state pulse spectrometer. The output data that has been taken using LTCC coils as the sensing elements is laid out and compared to the analytical values from chapters 4 and 5. A focus on the data comparison is still signal-to-noise ratio in dependence on different geometry parameters. Finally, chapter 7 gives a conclusion and discussion about the research works and proposes some feasibility studies concerning some different sensor variables and production techniques.

Chapter 2

Nuclear magnetic resonance

Nuclear magnetic resonance (NMR) is an invaluable technique for quantitative structure analysis and for the study of the inter- and intramolecular interactions that are central to many chemical and biological processes. Various disciplines in science where this phenomenon has taken strong roots have had a tremendous impact on research in physics, chemistry, biology and medicine. In chemistry and biology, NMR spectroscopy has become a standard tool for structural analysis thanks to the abundance of information it delivers on the localized scale. In contrast to spectrometry, which delivers a one-dimensional dataset (frequency spectrum), imaging techniques such as NMR microscopy and MRI (magnetic resonance imaging) have changed the diagnostic and visualization approaches in modern-day medicine and microbiology. The analysis presented in this chapter gives a phenomenological description of NMR processes as adapted from [28, 29] and [30] and methods of its detection.

2.1 Overview of NMR theory

2.1.1 Nuclear magnetic moments

There are numerous atomic isotopes, such as the nucleus of the hydrogen atom, that posses a property of an angular momentum $\vec{J}$, also called a *spin*. A nucleus with a nonzero spin creates a magnetic field represented by a nuclear magnetic dipole moment $\vec{m}$, also referred to as the magnetic moment. Spin angular momentum and magnetic moment vectors are related to each other by $\vec{m} = \gamma\vec{J}$ where γ is a physical constant known as the *gyromagnetic factor*. The amplitude of the magnetic moment is $\gamma\hbar\sqrt{I(I+1)}$, where $\hbar$ is the reduced Planck constant and I is a nuclear spin quantum number.

When subjected to the external static magnetic field $\vec{B}_0$, the magnetic moments are experiencing a torque $\vec{m} \times \vec{B}_0$ that results in turning the dipole towards the field $\vec{B}_0$. Since the dipole posses a certain angular momentum, the external force will impose a precessional motion, called a *Larmor precession* around the field $\vec{B}_0$, with a frequency $\omega_0 = \gamma B_0$ called *Larmor frequency*. All possible angles between the field and the precessing magnetic moment represent different quantum states whose energy difference is $\hbar\omega_0$. For the most simple case of hydrogen isotope ^{1}H there are two possible spin orientations: parallel, where the z-component of the magnetic moment points to the direction of $\vec{B}_0$ and energy (Hamiltonian) equals $-1/2 \cdot \hbar\omega_0$ and anti-parallel, where here the z-component of the magnetic moment points opposite to the direction of the $\vec{B}_0$ and energy is $1/2 \cdot \hbar\omega_0$. This discrete energy split under the influence of magnetic field is called *Zeeman splitting*.

A system of nuclei, as seen on macroscopic scale exhibits bulk magnetization $\vec{M}$ equal to the sum of all momenta per volume V of the sample: $1/V \sum_{n=1}^{N_s} \vec{m}_n$, where

N_s is the total number of nuclear spins. The spin population in each state can be statistically described with the help of Boltzmann statistics that shows probability of the dipole to have an energy E is proportional to $\exp(-E/k_BT)$, where k_B is the Boltzmann constant and T is the temperature of the sample in Kelvin scale. In the first order approximation, where $E \ll k_BT$ the magnetization will take the following expression:

$$\vec{M} = \frac{N_s\gamma^2\hbar^2 I(I+1)}{3Vk_BT}\vec{B}_0. \tag{2.1}$$

The magnetization takes the direction of the external field $\vec{B}_0$. This happens because the magnetic momenta add up their z-components which are parallel or anti-parallel to $\vec{B}_0$, while x- and y- components cancel out in average, due to their randomly uniform distribution. For nuclear magnetization to take place, there has to be a small excess of parallel oriented dipoles. Usually this surplus is about 3×10^{-6} of total nuclei, what makes nuclear magnetization an extremely weak effect. In example, hydrogen isotope ^{1}H in water sample at 1 T, where γ is 42.6 MHz/T and $I = 1/2$, gives the magnetization of $1.6 \cdot 10^{-3}$ A/m. For comparison, a typical electronic magnetization is a thousand times stronger than the nuclear. The fraction in eq. (2.1) corresponds to the static magnetic susceptibility (χ_0) divided by μ_0 that is permeability of the vacuum. It can be seen that it follows the Curie law of temperature dependence ($1/T$) that implies the paramagnetic nature of nuclear magnetization.

2.1.2 RF excitation

The inequality among spin populations leads to a net absorption of the electromagnetic energy by the spin system [28]. In order to excite such a system of spins and therefore acquire information about substance containing it, an alternating magnetic field $\vec{B}_1(t) = B_1\cos(\omega t)$ is introduced whose frequency corresponds to the energy difference of the spin states. The time-dependent behavior of $\vec{M}$ in the presence of total applied magnetic field $\vec{B}_{tot} = \vec{B}_0 + \vec{B}_1(t)$ is described quantitatively on the macroscopic level by the *Bloch equation*:

$$\frac{d\vec{M}}{dt} = \gamma\vec{M} \times \vec{B}_{tot}. \tag{2.2}$$

Assuming that $\vec{B}_0$ is directed along the z-axis and $\vec{B}_1(t)$ is applied perpendicularly to it, the equation 2.2 can be rewritten in the rotating coordinate system in which $\vec{B}_1$ is static. Then it takes a form:

$$\frac{d\vec{M}}{dt} = \gamma\vec{M} \times \left[\left(B_0 - \frac{\omega}{\gamma}\right)\vec{a}_z + B_1\vec{a}_x\right] = \gamma\vec{M} \times \vec{B}_{eff}. \tag{2.3}$$

Physically, equation (2.3) states that in the rotating frame the moments experience effectively a static magnetic field B_{eff}. The magnetization therefore precesses in a cone of fixed angle about the direction of B_{eff} at angular frequency γB_{eff}. When the resonance condition $\omega = \omega_0 = \gamma B_0$ is fulfilled, the effective field is simply $B_1\vec{a}_x$, and the magnetization vector that is parallel to the static field initially will precess in the y-z plane.

As a result of the forced precession, the bulk magnetization $\vec{M}$ is tipped away from the z-axis, creating a measurable transverse component $\vec{M}_{xy}$. The flip angle α at the end of the excitation pulse is $\gamma B_1\tau_p$ assuming that field had a constant amplitude through the pulse duration τ_p. Standard pulse technique uses the advantage of 90° pulse, that is the pulse that creates a flip from z- to y-axis.

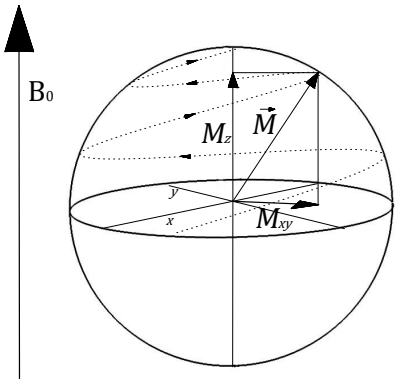

Figure 2.1: Precession of the magnetization vector $\vec{M}$ from the plane perpendicular to the $\vec{B_0}$ to the direction parallel with $\vec{B_0}$. As described by eq. (2.5), the transversal component of $\vec{M}$, M_{xy} decays while longitudinal component M_z recovers.

2.1.3 Free precession and relaxation

After the magnetized spin system has been perturbed from its initial or thermal equilibrium state, it will start to relax, provided the external force is removed and sufficient time given. This process is characterized by the precession of $\vec{M}$ about the B_0 field, called *free precession*; a recovery of the longitudinal magnetization M_z called *longitudinal relaxation*; and the destruction of the transversal magnetization M_{xy} called t*ransverse relaxation* [29] (Figure 2.1). Both relaxation processes are caused by time dependent microscopic magnetic fields in the surrounding of the nucleus as a result of the random thermal motions present in object. Relaxation processes are described as a first-order processes, specifically:

$$\begin{aligned} \frac{dM_z}{dt} &= -\frac{M_z - M_0}{T_1} \\ \frac{dM_{xy}}{dt} &= -\frac{M_{xy}}{T_2} \end{aligned} \tag{2.4}$$

Time constants T_1 and T_2 depend on the sample composition, structure and surrounding, while M_0 is the initial magnetization from eq. (2.1). Solving equations (2.4), we obtain the following time evolution of for the transverse and longitudinal magnetization components:

$$\begin{aligned} M_{xy}(t) &= M_{xy}(\tau_p)e^{-t/T_2}e^{-j\omega_0 t} \\ M_z(t) &= M_0\left(1 - e^{-t/T_1}\right) + M_z(\tau_p)e^{-t/T_1} \end{aligned} \tag{2.5}$$

Equation (2.5)phenomenologically describes what happens to the magnetization vector after the RF pulse of length τ_p: the transversal component of $\vec{M}$ decays with the time constant T_2 while the longitudinal component returns to the z-direction with the time constant T_1. It is important to emphasize that while $\vec{M}$ spirals back to the z-direction, its amplitude is not preserved because of different rate of these two relaxation processes. The signal that originates from the decay of the transversal component is referred to as the *free induction decay*, or FID.

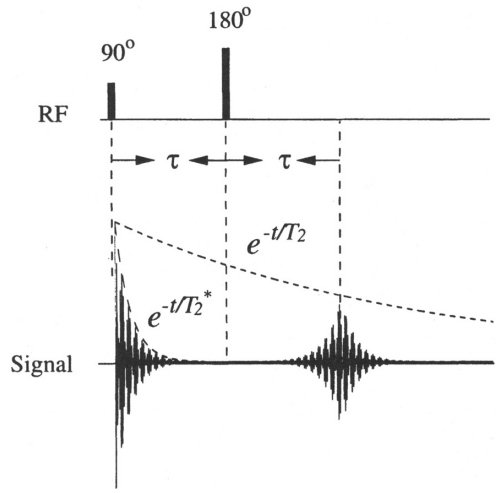

Figure 2.2: Formation of a spin echo signal by a 90° – τ – 180° pulse sequence. The application of a 90° pulse produces the FlD, which quickly disappears as the spins dephase. The application of a 180° pulse at a time τ after the 90° pulse produces an echo at a time 2τ after the 90° pulse. Image taken from [29].

2.1.4 Reduced relaxation time

Due to the inhomogeneities of the static field B_0 over the volume of the sample under test, many nuclei will have different Larmor frequencies. After excitation pulse, these nuclei will tend to recover to their initial states at the different precession frequencies, what will lead to desynchronization and destruction of net magnetization. The FID will thus decay at a much faster rate, specifically T_2^*, that is described as

$$\frac{1}{T_2^*} = \frac{1}{T_2} + \gamma \Delta B_0 \tag{2.6}$$

where ΔB_0 stands for the static field inhomogeneities over the sample of nuclei.

2.1.5 Spin echoes

Because the inhomogeneities of the static magnetic field cause faster destruction of the magnetization vector, FID will decay at much faster rate. But the coherence of the spin assembly can be recovered by applying 180° pulse some time after the initial 90° pulse. After a 180° pulse, all spins are flipped 180 degrees around y-axis putting all the spins that were ahead to the tail position of in the precession motion. During this the free precession, the faster spins pick up with the slower ones making whole assembly coherent once again. This coherence will result in a transverse magnetization M_{xy} precessing. This magnetization induces a signal shaped like two FIDs placed back to back, which is called a *spin echo* (Figure 2.2). Discovered by E. Hahn in 1950's, it was one one of the most influential discoveries in the field of NMR ([31]).

A sequence of 180°-pulses may be applied after initial spin echo. It will result in repeated appearance of the spin echoes, but with ever decreasing envelope amplitude. This decay is the product of original T_2 relaxation. The spin echo technique is extensively exploited in almost all modern NMR spectrometry devices.

2.2 Nuclear quadrupolar resonance

Nuclear quadrupole resonance (NQR) spectroscopy is a branch of NMR spectroscopy and is concerned with the absorption of electromagnetic waves by the nuclei of solid-state matter in zero magnetic field. The reason for the introduction to this topic is the availability of the NQR spectrometer for purposes of this thesis research instead of "classical" NMR spectrometer. Since the thesis is not focused on the physical depth of the NMR but on coil design, only the basic introduction to the NQR will be delivered.

2.2.1 Quadrupole moment and electric field gradient

Nuclear quadrupole moments arise when the charge distribution within the nucleus acquires an ellipsoidal shape rather than spherical. This distribution results in two anti-parallel electric dipoles. In an electric field, each of these experiences a torque tending to align them along the field but since the two turning torques are equal and opposite, there is no net effect. However, in an electric field gradient, axially symmetric about ellipsoid long axis, the two torques are not equal and a net turning torque exits which is proportional to the electric field gradient and to the extent to which nuclear charge distribution departs from spherical symmetry. Since all quadrupole nuclei also have an angular momentum, the situation is comparable to the precessional model for nuclear magnetic moment in static magnetic field. By analogy, the nuclear quadrupole responds to that torque by precessing about the direction of maximum electric field gradient.

For a nucleus of charge density ρ_n per volume element $dV = dxdydz$ placed inside of the electric potential U produced by the electronic charge distribution, potential energy will be $-\int \rho_n U dV$. Since the U varies over the nuclear volume, it may be expressed by the means of Taylor series expansion evaluated at the center of the nucleus:

$$U(\vec{r}) = U_0 + \left(\vec{r}\cdot\vec{\nabla}\right)U + \frac{1}{2}\left(\vec{r}\cdot\vec{\nabla}\right)^2 U + \cdots \tag{2.7}$$

Higher terms may be important in certain cases, but in the simple description they may be omitted. The term $\vec{\nabla}U$ stands for electric field $\vec{E}$ and $\vec{\nabla}^2 U$ for electric field gradient $\vec{\nabla}\cdot\vec{E}$. By putting eq. (2.7) in the integral $-\int \rho_n U dV$ and performing a multi-pole expansion of the charge density according to [32, p. 99], we get the total potential energy

$$P.E. = -ZeU_0 - \vec{p}\cdot\vec{E} - \frac{1}{2}\sum_{ij} Q_{ij}\frac{\partial E_j}{\partial x_i} \tag{2.8}$$

where x_i stands for coordinates x, y and z. Ze is the total nucleus charge ($\int \rho_n dV$), $\vec{p}$ is electric dipole moment ($\int \vec{r}\rho_n dV$) and Q_{ij} is a *quadrupole moment tensor* defined as $Q_{ij} = \int \rho_n x_i x_j dV$. From the expansion above it is visible how various multipoles interact with the external electric field - the charge with the potential, the dipole with the field, the quadrupole with the field gradient and so on. The first term is a scalar and does not depend on orientation so it can be ignored in NMR study. The second term vanishes because the electric dipole moment of positively charged nucleus is zero.

2.2.2 Energy states of nuclear quadrupole moments

The energy level or states of a nucleus are defined by the quantum number of angular momentum I and its projection I_z along the z-axis [33]. The z-axis is taken to be in the direction of the maximum principal component of electrical field gradient $\partial^2 U/\partial z^2$. This gradient is proportional to the elementary charge e by factor q. The field gradient qe plays the role of B_0 in NMR.

Transition between the states is induced by the alternating magnetic field in the same fashion as with the ordinary NMR experiment. Returning to equilibrium the radiation of frequency that corresponds to the energy difference is emitted. For a spin number $I = 3/2$ (^{63}Cu) there are two possible energy levels i.e., only one quadrupole transition at frequency:

$$\omega_0 = \frac{1}{2}\frac{qe^2Q}{\hbar} \tag{2.9}$$

The technique is very sensitive to the nature and symmetry of the bonding around the nucleus. The energy level shifts are much larger than the chemical shifts measured in NMR. Due to symmetry, the shifts become averaged to zero in the liquid phase, so NQR spectra can only be measured for solids.

2.3 Signal detection

In a typical NMR experiment, where a static magnetic field B_0 is assumed to point in z-direction, the sample's magnetization will align itself with the static field. When the magnetization in an elementary volume dV centered at any point $\vec{r}$ is perturbed from its thermal equilibrium value M_0, its transverse component will rotate about the direction of the static field at the Larmor frequency ω_0. If the amplitude of this rotating component is denoted by $M_{xy}(\vec{r})$, Faraday's Law dictates that the changing magnetic flux associated with the magnetic moment $M_{xy}dV$ will induce a small voltage dS across the NMR receiver coil (Figure 2.3). In 1976, Hoult and Richards related the voltage induced by a rotating magnetic moment located at any point $\vec{r}$ directly to the strength of the magnetic field produced in the transverse plane at the same location $B_{xy}(\vec{r})$ when a unit current flows through the receiver coil at the Larmor frequency [1]. This so called Principle of Reciprocity shows that amplitude of the induced voltage per unit volume ($S_{puv} = dS/dV$) can be expressed in the following fashion:

$$S_{puv}(\vec{r}) \propto \omega_0 M_{xy}(\vec{r}) B_{xy}(\vec{r}) \tag{2.10}$$

The factor ω_0 comes from the time derivative of the magnetic flux in the law of induction.

2.3.1 Principle of reciprocity

In classical electromagnetism, reciprocity refers to a variety of related theorems involving the interchange of time-harmonic electric current densities (sources) and the resulting electromagnetic fields in Maxwell's equations for time-invariant linear media under certain constraints. The Principle of Reciprocity, developed in 70's by D.I. Hoult ([1], [34]) relates the magnetic field produced by the current in a current loop with the voltage induced in the same loop by the magnetic flux originating from a distant source. To understand the principle of reciprocity one needs to think of the electromotive force emf induced in a loop of an electrical conductor by a small rotating nuclear magnet $\vec{m}$. If we divide the receiving loop into a mesh of small elementary areas (Figure 2.4a), the magnetic scalar potential ϕ from the magnetic moment $\vec{m}$ at any point $\vec{r}$ in the loop is:

$$\phi = \frac{\vec{m} \cdot \vec{r}}{4\pi r^3} \tag{2.11}$$

As the magnetic field is gradient of the potential ($\vec{B} = -\mu_0 \nabla \phi$), the flux linkage Φ through the coil is then the sum of the fluxes passing through each elementary area, as shown in Figure 2.4a, or

$$\Phi = -\mu_0 \int_{loop} \nabla \cdot \left(\frac{\vec{m} \cdot \vec{r}}{4\pi r^3} \right) d\vec{S}, \tag{2.12}$$

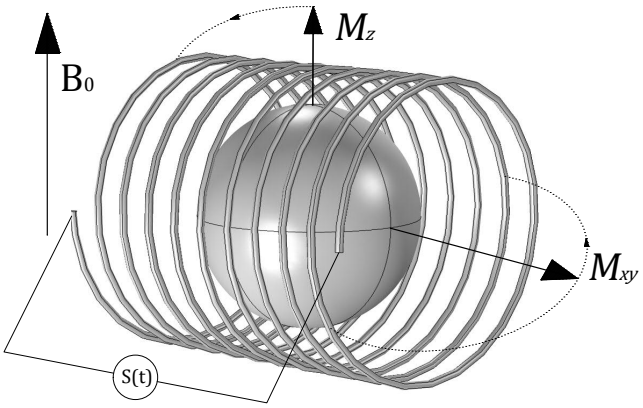

Figure 2.3: Precession of the magnetization vector $\vec{M}$ from the plane perpendicular to the $\vec{B}_0$ to the direction parallel with $\vec{B}_0$ induces signal $S(t)$ proportional to the transversal magnetization component M_{xy} in the coil placed around the spherical sample.

where $d\vec{S}$ is the vector normal to the surface of an elementary area dS.

At the same time we can use the same mesh to try to find a magnetic field produced by the current I in the loop, using the Biot-Savart law. If we consider each mesh element as a small current loop (Figure 2.4b), we can integrate over all elementary magnetic moments $Id\vec{S}$ to find mathematical construct for the magnetic field $\vec{B}_1$ at the distance $\vec{r}$ from the loop.

$$\vec{B}_1 = \mu_0 I \int_{loop} \nabla \cdot \left(\frac{\vec{r} \cdot d\vec{S}}{4\pi r^3} \right). \tag{2.13}$$

There is clearly some symmetry between the last two equations. Minus sign is missing in the second one because the $\vec{r}$ has been reversed. Further on, it is easy to show that magnetic flux can be written as:

$$\Phi = -\frac{\vec{B}_1}{I} \cdot \vec{m}. \tag{2.14}$$

From the Faraday's Law comes the fact that the induced emf per unit volume is proportional to the rate of change of flux linkage $\partial\Phi/\partial t$. If we consider all magnetic moments in the sample volume V_s, we obtain

$$S(t) = -\int_{V_s} \frac{\partial}{\partial t} \left(\hat{B}_1 \cdot \vec{M} \right) dV. \tag{2.15}$$

Here, $\hat{B}_1$ stands for the magnetic field produced by the current of 1 A, and $\vec{M}$ is the sample bulk magnetization which is expressed as a sum of magnetic dipoles per unit volume. To further simplify the calculus, we assume homogeneous magnetization and RF field across the sample, and the signal amplitude becomes:

$$S = k_0 \omega_0 (\hat{B}_1)_{xy} M_0 V_s. \tag{2.16}$$

Here is the $(\hat{B}_1)_{xy}$ component of $\hat{\vec{B}}_1$ perpendicular to the main field $\vec{B}_0$ and k_0 is, so called, an "inhomogeneity factor" which may, if necessary, be calculated for most shapes of the coil. Equation (2.16) is the expression for the expected NMR signal induced at the receiver coil. Here it is shown that, using the principle of reciprocity, one can find the solution using the Biot-Savart law which is much easier to numerically integrate than Faraday's law.

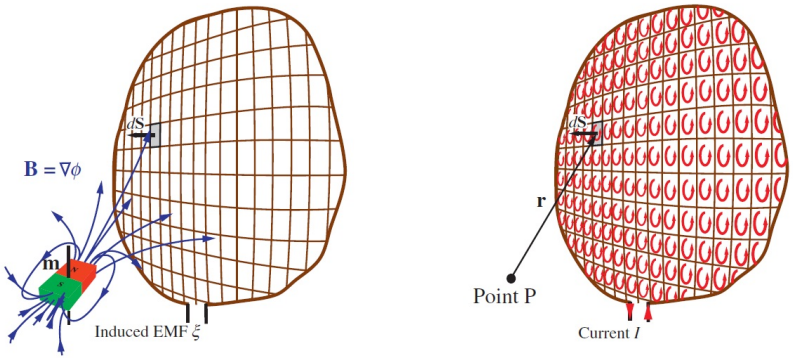

(a) (b)

Figure 2.4: Surface enclosed by the current loop and divided into infinitesimal regions dS. First figure shows magnetic potential originating from small distant magnet. Second figure depicts magnetic field induced by the current loop at the position of the same small magnet. Image taken from [34].

2.3.2 Typical NMR spectrometer block

Voltage induction in the NMR coil is the starting point of the whole measurement chain (Figure 2.5). The pick-up coil that is represented as a series circuit of resistance R_c and inductance L is a part of the resonant LC circuit which is tuned at the Larmor frequency with a quality factor Q. The Q is defined as a ratio of the maximum energy stored in one cycle and power dissipated in heat. Since the dielectric losses in the capacitor are small it is primarily influenced by the coil parameters:

$$Q = \frac{\omega L}{R_c} \tag{2.17}$$

The signal generated in this resonant circuit will result in a voltage $v(t) = QS(t)$ across its terminals. For copper wire solenoid coils, Q values are typically 50 to 100.

The LC resonator is connected to a circulator coupler. It is a multi-port device that only enables signal propagation between certain ports. This is a very important component of the NMR spectrometer because the same coil and the same LC resonator are used for both sample excitation and NMR signal detection. The coupler allows the pulse from the power amplifier to go to the LC resonator but not to the pre-amplifier in the detection channel. Also, the signal generated at the LC circuit only can travel towards the pre-amplifier. In RF electronics all the devices should be matched to the same reference impedance (most often 50 Ω) so there is a matching network between LC circuit and the coupler.

The synthesizer module is the source of the radio-frequency signals used in the spectrometer. With an embedded oscillator and a phase-locked loop (PLL), it generates signals from below 1 MHz to 2 GHz, even though for NMR frequencies of few tens to few hundreds of MHz are used. The RF signal generated by the synthesizer is fed to two devices: a power amplifier and a heterodyne receiver. The role of the power amplifier is to generate sufficiently large B_1 field within the detection coil, for which it is sometimes necessary to reach the voltage pulses of few kV in amplitude across the terminals of the coil. The length of the pulse, typically few milliseconds, is controlled by the digital pulse controller.

The pre-amplifier has a role of rising the usually weak NMR signal (few microvolts) from the LC circuit to the voltage level suited for the further processing. It is extremely important to ensure a low noise profile pre-amplifier so that the signal doesn't get drowned in the noise. Filters and mixers are used for scaling the NMR

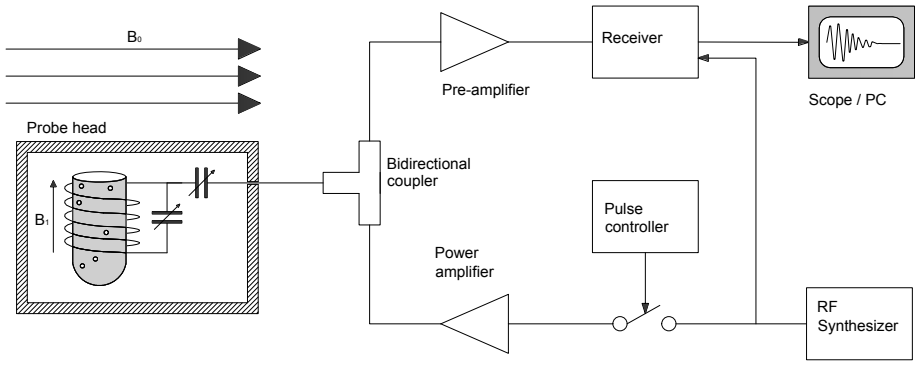

Figure 2.5: Typical NMR spectrometer building blocks

frequency down to a level of few kilohertz so that analog-to-digital conversion may take place. In modern systems direct A/D conversion is suited for frequencies up to 100 MHz so that mixing and filtering is all digital. Sometimes heterodyne receiver may be used instead and analog signal mixed to DC range is displayed directly on the scope. The signal is finally processed on the computer where the useful data of the NMR experiment are extracted and studied.

The static magnetic field is generated by a large electromagnet (sometimes superconductive) in which a *probe head* is placed. The probe head is a part of the spectrometer which contains LC circuit and NMR sample enclosed in a metal casing. It is the most sensitive part of the spectrometer since the weak NMR signal is generated in there and is prone to various noise interferences.

2.4 SNR and coil design considerations

2.4.1 Noise in the detection system

Thermal noise is the common name for the random charge fluctuations within the conductive material, whose spectral power density is $k_B T$. Because of its uniform spectral distribution is is also referred to as *white noise* and sometimes a *Gaussian noise* because of a normal amplitude probability distribution. In a coil that is part of the LC circuit of bandwidth Δf the voltage generated by the noise of the power P_n is $\sqrt{2P_n R_c}$. Along with the noise generated by the sample within the coil the noise voltage is given as

$$V_{noise} = \sqrt{4k_B(R_s T_s + R_c T_c)\Delta f}, \tag{2.18}$$

where R_s and R_c terms represent the ohmic resistance of the sample and coil, respectively, while the T_c is coil temperature and Δf is the bandwidth of the receiver. When linear dimensions of the sample are below few milimeters, the noise due to the sample resistance is usually small compared to the noise due to the coil's resistance [35].

Along with the noise generated by the resistance of the coil, there is also a noise generated in all other elements of the NMR spectrometer. Noise of the semiconductor integrated circuits is usually both, white noise and $1/f$-noise, that is the noise that drops in amplitude as frequency increases. The overall noise of the amplifier, filter and mixer blocks is usually specified by the manufacturer in their noise figure tables.

Totally different but very important source of noise is mechanical tremble of the coil-sample arrangement. During the pulses the magnetic field B_1 exerts significant forces on the wires and the sample. This can cause the rattling of the coil and sample for hundreds of microseconds if not taken care of, especially with small coils and the correspondingly thin wires.

2.4.2 Signal-to-noise ratio

By combining equations (2.1), (2.16) and (2.18) we can deduce signal-to-noise ratio or SNR of the coil as:

$$SNR = \frac{k_0 \eta \hat{B}_1 V_S N \gamma \hbar^2 I(I+1)\omega_0^2}{3k_B T F \sqrt{4k_B T R_c \Delta f}}. \tag{2.19}$$

Factors from the eq. (2.19) can be divided into three groups: physical constants ($\hbar$ and k_B are reduced Planck's and Boltzmann's constants, respectively), sample parameters (V_S is the sample volume, N number of spins per unit volume, γ the gyromagnetic ratio, I the nucleus spin quantum number and η that is a filling factor determined as the ratio of the sample's volume and coil volume), spectrometer parameters (k_0 is a scaling factor accounting for the RF inhomogeneities of the coil, $\hat{B}_1$ is the RF magnetic field induced in the coil per unit current, ω_0 the nuclear Larmor precession frequency, T the temperature, F noise factor of the spectrometer, R_c resistive losses of the coil, Δf spectral bandwidth).

From the above equation it is clear that most of the parameters are constants of nature or dictated by the sample properties or the sample conditions. The basic strategy to optimize the NMR signal is to choose the lowest possible temperature combined with the highest magnetic field (and thus ω_0) available. It has been widely accepted that cooling the RF-coil in so-called cryo-probes, where the temperature goes down to few tens of Kelvin, is a straight-forward way to improve sensitivity due to the nature of Curie's law. For pure metals, the resistivity is inversely dependent on temperature, so according to eq. (2.19), reducing the temperature 10 times increases sensitivity by roughly 100 times [36]. Increasing magnetic field is also conventional approach in increasing sensitivity. Commercially available instruments can produce up to 21 T static field, providing an NMR signal frequency up to 900 MHz, even though most of the NMR experiments are being carried out in the fields of 2 to 7 T, what corresponds to the working frequency of 80 to 300 MHz (for protons $\gamma = 42.5\,\mathrm{MHz\,T^{-1}}$). The disadvantage of this approach is the cost of high field magnets, which usually involve liquid Helium cooling, and low value of B_1 field because one has to reduce inductance L to keep the resonator at ω_0.

Increasing the number of nuclei, or the product $V_S N$, may seem obtainable by increasing sample size, but at the same time with increasing volume, increases the inhomogeneity of the sensing coil. Larger coil means bigger inductance L, and there are two downsides of increasing the L: first, it is practically unachievable to find a low enough capacitance needed to tune the LC oscillator at ω_0, and second, it is hard to keep the value of B_1 for the large L. The only technical design parameter of the coil that can be manipulated are in fact $\hat{B}_1$ and R_c. This translates to the question of choosing the proper coil geometry for any given sample. Hence, for a given receiver bandwidth, temperature, sample volume and concentration, nuclear species and magnet strength, the SNR per unit volume (SNR_{puv}) of the RF coil can be described as:

$$SNR_{puv} \propto \frac{\hat{B}_1}{\sqrt{R_c}} \tag{2.20}$$

The numerator of the above equation represents coil sensitivity i.e. the coupling between the sample magnetization and the coil. For most coils, a good estimate of their sensitivity can be easily found by assuming uniform distribution of current

in the cross section of the coil wires and by performing an integration according to Biot-Savart's law. On the other hand, the resistance of the coil is often difficult to estimate because it depends on the details of the current distribution in the cross-section of the coil wire [37].

In modern NMR spectrometers the noise is mostly diminished by digital signal processing, most notably by averaging. By averaging multiple FID and spin-echo sequences one might achieve $\sqrt{n}$ times better signal-to-noise ratio, where n is the number of averaged sequences.

2.4.3 Inhomogeneities of static and RF field

When the static field B_0 is inhomogeneous over the test sample, it does not resonate at the single frequency ω_0. Instead, a band of frequencies $\Delta\omega$ will show up on a resonant curve, reducing the overall resolution of the spectrometer. That's the reason why many modern spectrometers have strong demands on electromagnet's quality and static field homogeneity. However, independent of the electromagnet quality, local magnetic field inhomogeneities arise from the composition and structure of the sample itself. Interactions between the atoms within the sample will cause significant shift from the ω_0, also called a *chemical shift* [29]. There are additional inhomogeneities produced by susceptibility mismatch of the sample and coil. The coil, usually made of copper or some other highly conductive metal is slightly paramagnetic compared to the sample which is most often diamagnetic, and the surrounding that is mostly diamagnetic. This mismatch introduces spatial variations of the static field.

The aspects of RF homogeneity and optimization of sensitivity for solenoid coils was analyzed in a great detail by K. Minard and R. Wind in [38] and [39]. They have contributed with the extensive guidelines in designing the coil with the specific number of windings and wire size for either lossy and loss-free samples. It was shown that the homogeneity of the RF magnetic field in the region of the NMR sample is prerequisite for good performance in many NMR experiments. F. Engelke in [40] made a computational analysis of this field and also examined behavior of the field when wavelength and coil size become comparable. The features and limitations were probably the best reviewed by A. Webb in [41] where he brings the concept of *microcoils* which was introduced to increase the volume sensitivity by miniaturizing NMR coils.

Spatial differences in RF field strength result in non-uniform flip angles and these, in turn, drive variations in magnetization. Minard and Wind have shown explicitly how variations in both RF field strength ($\Delta B_{xy}/B_{xy}$) and transverse magnetization ($\Delta M_{xy}/M_{xy}$) degrade the spatial uniformity of a homogeneous sample's NMR response [38]. Specifically, their analysis is devoted to the field non-uniformities of solenoid coil and its dependence on coil geometry factors as well as experimental parameters, such as repetition time and sample's longitudinal relaxation rate. The authors provide numerical method for minimizing coil's dimensions in respect to maximum tolerable deviation of the NMR response. Given the afore mentioned parameters, numerical solution allows to determine coil's minimum length-to-diameter ratio for different ratios between sample's length and coil's diameter.

2.4.4 Coil designs

Different coil designs have been tested in order to increase the coil sensitivity; most popular of them are saddle and solenoid geometry. In NMR spectrometry, the trend is toward the miniaturization of the sample as well as coil and these are, hence, referred to as the microcoils. While the main advantage of the solenoid microcoils lies in the inherently higher sensitivity and better filling factor η, in comparison to the saddle coils they have a greater magnetic susceptibility mismatch between

the coil, capillary and the sample that results in the broader resonance spectrum and, therefore, lower spectral resolution [41]. Peck and Minard have tried to find optimum geometry parameters of these coils in order to optimize the SNR ([2, 38] and [39]). Eroglu and Massin have looked for ways of increasing volume sensitivity of planar coils in dependence of their geometrical parameters ([37, 35] and [42]). In solid-state NMR the resonance lines are rather broad because interactions do not average out as in liquid solutions. For solid-state samples the requirement for the field homogeneity is therefore less stringent and the coil can in general be designed to fit tightly around the sample holder [36].

A novel approach was taken by many researches in 2000-s, most notably by S. Eroglu, R. Magin and C. Massin. So called *planar* or *surface* microcoils were considered to be a better match for the investigation of biological cells and other two-dimensional samples. Eroglu *et al.* in [37, 35] and [42] reviewed the design and performance of the spiral surface microcoils and their importance in micro fluid applications. Fabrication of the micro channels and the coils for micro fluid spectroscopy was presented by Massin *et al.* in [43]. The possibility of using surface microcoils in microscopy or microimaging was well elaborated by Massin et al. in [44, 45] and [46]. A significant contribution in the planar coil design was given by the Peck, ([47, 48]), B. Gimi ([49]), K. Ehrmann ([50]) and N. Baxan ([51, 52]).

The most popular method of producing 3D coils was simple hand wire-wounding around the capillary holding the sample or, in best case, some fine micro machining as in [2]. For planar microcoils, the well established techniques of lithography or vapor phase deposition on glass or silicone substrates are suited best. The work presented in this thesis introduces the thick film technology of LTCC as an alternative to the standard thin-film technology or hand wounded wire. The benefits of this approach lies in the combination of best features of wire wounding and thin-film technology: it has precision and repetitiveness of the thin-film technology in handling of the micro structures while keeping the robustness and high conductance of the thick wires.

Chapter 3

LTCC Materials and Fabrication Process

In this chapter, an introduction to Low Temperature Co-firing Ceramic (LTCC) technology is presented as this technology was considered to realize the coils with improved signal-to-noise ratio per unit volume as well as thermal and mechanical properties compared to ordinary coils used in NMR spectrometry. Physical background concerning the structure of ceramics and pastes applied on it is provided. Mechanical and electrical properties of these materials are theoretically analyzed and their measurements laid out. Standard fabrication processes and techniques are described. Advantages and disadvantages to some other commonly used technologies are discussed. This chapter will serve for argumentation why is the LTCC technology beneficiary for inductor development.

Since the beginnings of electrical engineering and component design, ceramics have been valuable material due to their high isolation characteristics (high resistivity and electrical strength, low ionic conductivity) [53]. The use of ceramics for multilayer substrates in electronic circuits dates back to the 1950s [7]. IBM was the first company that has commercialized the technology by incorporating it in circuit boards of their mainframe computers in the 1980s [5]. There was shown that ceramic substrates did have advantages concerning reliability of the packaging compared to other contemporary substrates like phenolic or epoxy resin or Bakelite. A disadvantage of that technology was relatively high sintering temperatures (1600 °C for alumina) what made co-firing with the conductive materials, for example, silver or copper impossible. Due to this high sintering temperatures, this technology is commonly referred to as *high temperature co-fired ceramics* (HTCC) technology.

Very soon ceramic industry developed a low temperature co-fired ceramics (LTCC) technology by using composites of Al_2O_3 and SiO_2 that allowed sintering temperatures below 900 °C. Therefore, metals with higher electrical conductivity, - copper, silver, gold - could be used for co-firing [6]. Nowadays, LTCC substrates are used for high-end radio and microwave frequency applications because of their superior electrical properties and the design of micro-electro-mechanical systems (MEMS) because of their advantageous thermo-mechanical properties. Since the LTCC technology can be used in building both the sensor and packaging part of the sensor, it was the technology of choice for this thesis. This chapter is devoted to the thorough description of required process steps and their respective optimization. Section 3.1 provides a short overview and is an introduction to a typical LTCC fabrication process. All the process parameters for every raw material used in this thesis are given in the table 3.1 at the end of the chapter.

3.1 Fabrication process

All LTCC processes for fabrication of sensor coils including their packaging have been developed in the Laboratory for Integrated Circuits and Technologies, at the Institute of Sensor and Actuator Systems (ISAS), Vienna University of technology. The standardized process starts with the raw LTCC tape preparation, including laser cutting and via filling, screen stencil preparation using photolithographic methods, screen printing of the conductive paste, lamination and, finally, co-firing. Raw LTCC tapes are provided by the manufacturer (most notably Heraeus, CeramTec and ESL) in form of reel - rolled sheets. Over the years many papers on characterization of LTCC materials have been published by the research groups at ISAS ([54, 55, 56, 57] and [23]) and their characteristics are listed in table 3.1.

3.1.1 Chemical composition of the LTCC tapes

LTCC sheet in unfired (sometimes also called *green*) state is a thin flexible compound of ceramic and glass powder with organic composites. In order to allow the co-firing of metals with high electrical conductivity, the sintering temperature of the ceramic substrate has to be reduced well below the melting point of the individual metal (e.g. Cu: 1084 °C, Ag: 962 °C, Au: 1064 °C). Glass is added to the ceramic powder in order to lower the sintering temperature requirements while maintaining advantageous properties of HTCC: high mechanical strength, high specific electrical resistivity and low dielectric loss [58]. The most commonly used glass for LTCC substrates is borosilicate glass with the main constituents silica (SiO_2) and boron oxide (B_2O_3). Silica shows high melting point, high viscosity, low thermal expansion and good chemical durability, whereas boron oxide reduces the viscosity of the glass. Other types of glass are often used to modify thermo-mechanical properties: to increase resistivity PbO or BaO are used, to reduce melting point K_2O or Na_2O and to improve chemical durability CaO, Na_2O or ZnO. As ceramic constituent Al_2O_3 powder is used.

Organic materials serve as the *binders* for maintaining the strength of the compound and increasing its formability; *plasticizers* that give the compound its plasticity and flexibility; *dispersing agents* that provide control of the pH of the compound; *antifoaming agents* to prevent the occurrence of foam in the slurry; surface treatment *coupling agents* to improve poor wettability of ceramic powder by lowering its surface tension; and non-aqueous organic *solvents* [6]. However, in the firing process before the sintering takes place, all organic composites have to be completely eliminated, leaving in the end a firm structure of sintered ceramic particles.

The conductive paste is of similar composition. Functional particles that define electrical properties of the paste can be precious metals like Ag, Au, Pd or Pt and base metals like Al, Cu, Cr or W. There are also resistive pastes available, which use different metal oxides as functional particles. Inorganic binders (based on glass) provide adhesion to the ceramic substrate and control the expansion coefficient of the paste. Organic binders specify the rheology of the paste, what is a crucial parameter for the screen printing quality. These binders evaporate during the firing as well.

3.1.2 Laser processing

LTCC sheet is a priori cut into pieces that are typically 7 cm times 5 cm large. At ISAS Laboratory a 120 W Nd:YAG RSM100D laser machine by Rofin-Sinar Technologies, Inc. is used to cut the outer contours, via holes and perforations (Figure 3.1a). Also, additional four reference holes are cut at the edges of the tape that will be of use in the printing and laminating processes. It is obvious that different LTCC tape will require different laser parameters, such as laser diode current, pulse fre-

quency and the head velocity. These parameters are empirically determined by the collaborators at ISAS and are presented at the table 3.2 at the end of this chapter.

3.1.3 Via filling and screen printing

Laser cutting and via filling are consecutive processes needed for every single LTCC tape. The latter one (Figure 3.1) is achieved by filling the via holes with a conductive silver-based paste. High viscosity of the paste and small size of the vias (typically 150 µm to 250 µm in diameter) prevent from paste leakage, which is further discouraged by drying the tapes in the oven at 75 °C. Via filling is done on the stencil printer De Haart SPSA-10 with vacuum applied on the bottom part of the porous aluminum table. The via pastes have a higher amount of solids than conductor track pastes to prevent voids that could arise during the sintering. The via paste has also to account for the shrinkage of the LTCC tape during sintering to avoid stresses due to the volume difference. The filling process depends mostly on squeegee, stencil and vacuum quality.

When the vias are filled and dried, conductor tracks can be printed (Figure 3.1b). For adequate track printing, 30 µm to 50 µm thick Murakami stencil was attached on steel screen with mesh with the resolution of 320 - 450 dpi. The stencil was made with standard photolithography technique. Screen printing was performed with silver-based paste under pressure of 2.7 bars. After printing, tapes were dried once again at the temperature of 75 °C.

The term *co-firing* is related to the simultaneous firing of both LTCC tape and conductive paste. It is obvious that, during the firing, the structure will experience certain shrinkage due to the loss of organic composites. Therefore firing properties of both tape and conductive paste must be compatible in order to obtain the same shrinkage rate what will prevent cracking of the lines. For the same reason, caution has to be taken in the design of conductive track layout.

3.1.4 Stacking and Lamination

When the printing process is finished, the LTCC tapes are stacked together and laminated. Proper positioning of the tapes is done with the help of four additional reference holes which are laser cut and fixed to four reference pins fastened on a metal mold (Figure 3.1). This kind of a mechanical fixation yields matching of about 30 µm. A single tape of a PET film is added between the LTCC stack and press mold to prevent adhesion. Once stacked and preheated to 80 °C the structure is exposed to a pressure of 80 - 160 bars depending on the structure's number of layers for 3.5 minutes. During this process, called lamination, a single substrate is created from the stacked layers of LTCC and conductive paste. At the ISAS clean room two lamination presses are on disposal - an isostatic and an uniaxial press Carver 3895CE, form Carver Inc., USA. Whereas the isostatic press applies pressure equally on all sides by immersing the sample in water, the uniaxial press only applies pressure along the out of the plane axis. The Carver press specifies the applied pressure in units of kilograms per cm^2. In practice the required press force in kilograms is specified by multiplying the desired value of pressure in units of bar with the surface of the substrate in square centimeters.

3.1.5 Sintering

Sintering is the process of compacting and forming a solid mass of material by heat and/or pressure without melting it to the point of liquefaction. Since the sintering of the LTCC structures is performed by exposition to heat, the process is also called *firing*. Because different materials, tapes and pastes, are sintered together simultanously the process is called *co-firing* and is the most sensitive process in

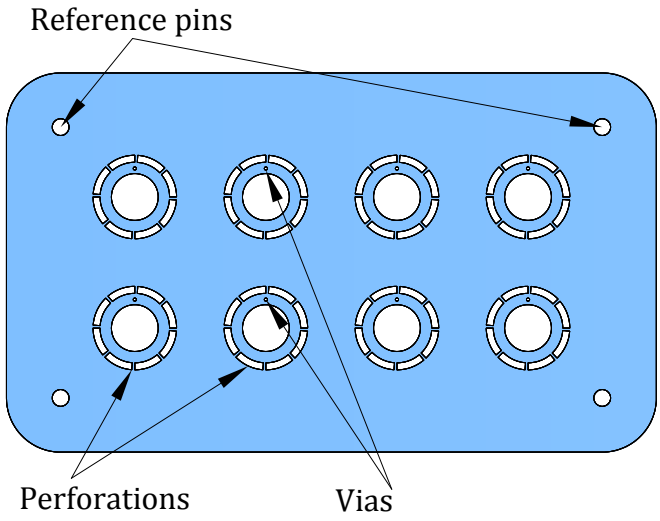

(a)

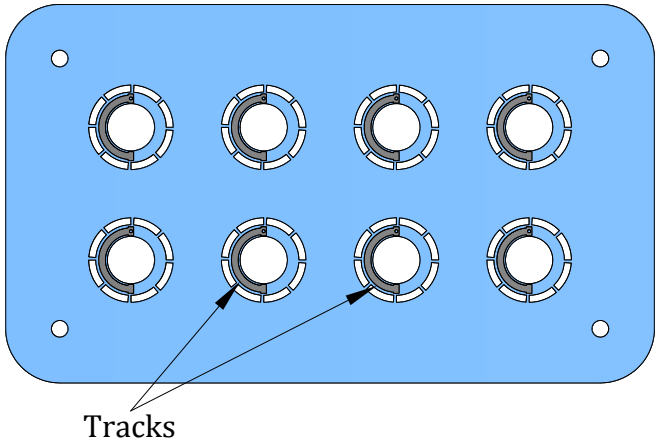

(b)

Figure 3.1: Typical layout of multiple structures on single LTCC substrate. (a) shows the laser processed tape with vias, holes and perforations. (b) shows the same tape with the screen printed conductor lines.

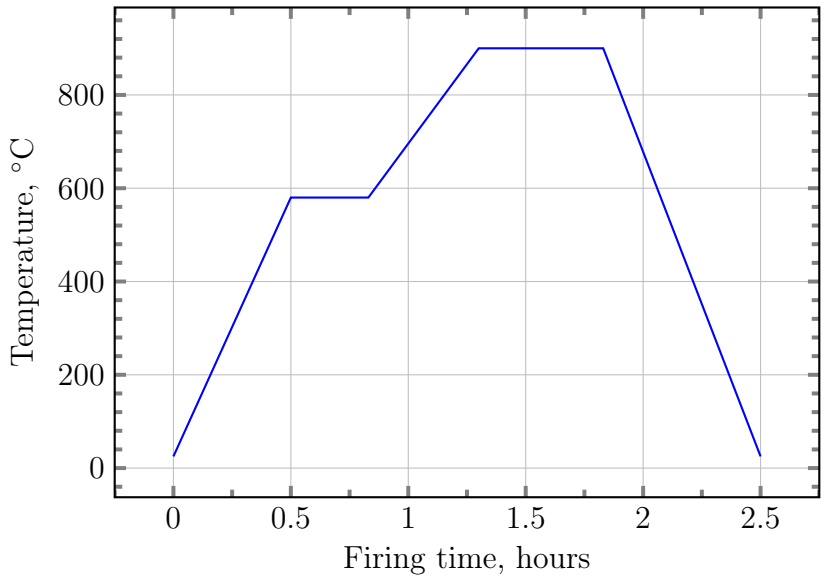

Figure 3.2: Typical box furnace temperature profile for CeramTape GC LTCC tape. Preheating phase develops in the first 30 minutes, after which burning phase takes place for 20 minutes at 580 °C. Following heating phase leads to 30 minutes long sintering phase at 900 °C , after which cooling is executed at 30 °C.

LTCC manufacturing. During the co-firing, ceramic and conductor particles are sintered together in a firm ceramic-like structure. Numerous complex reactions and transformations occur during the process, but most notable of all is the shrinkage of the structure due to crystallization of the glass particles and evaporation of organic constituents. Numerous research groups have worked on sintering behavior of LTCC and properties of sintered structures have been examined [56].

The three most important technical points in this process are: (1) controlling the firing shrinkage of the whole substrate, (2) controlling firing shrinkage behavior of different materials within to prevent defects, (3) achieving both, anti-oxidation of the conductor material and melting of the binder material (glass granules) [6]. At ISAS sintering control is done by adjusting temperature profile and atmosphere content in either box furnace Linn HT-1600 or belt furnace BTU-QA41. While in the box furnace the temperature profile is set by the PC program, the belt furnace has six temperature zones and adjustable belt speed. Optimal firing parameters for materials used here were empirically determined starting with the manufacturer's recommendations from datasheets and modifying them for optimum quality. The used parameters are listed at the table 3.3.

The firing process is usually divided into five phases: preheating, burning, heating, sintering and cooling (Figure 3.2). The preheat phase slowly brings the temperature of the sample from the room temperature to around 400 to 600 °C. Depending on the sample size, the temperature rate can vary from 0.1 to 30 K/min. In the burning phase, which can last from a few minutes to a few hours, all organic constituents are burned and evaporated. Further heating brings the sample to its final temperature, at which sintering processes take place. The final phase - cooling - brings the sample down to room temperature at a slow rate to prevent extreme thermal stress and cracking.

Table 3.1: Properties of standard LTCC tapes. (Values taken from [54], [55], [56], [57] and [23])

Material	CT707	CT708	CT802	CeramTape GC
Geometric properties				
Thickness in green state, μm	150	250	250	300
Shrinkage in xy-plane, %	20	17.2	17.5	19.5
Shrinkage in z-direction, %	30	30	30	25
Electrical properties				
Dielectric constant ϵ_r at 1 MHz,	6.3	6.4	8.6	7
Dielectric loss δ at 1 MHz,	0.003	0.003	0.0025	0.002
Dielectric strength, kV/mm	-	-	-	10
Thermal properties				
Expansion coefficient, ppm/K	.2	7.6	5.1	5.3
Thermal conductivity, $1\,\mathrm{W\,m^{-1}\,K}$	4.3	-	4.3	2.2
Mechanical properties				
Bulk density, g/cm^3	3.2	3	3.3	2.9
Young modulus, GPa	54	-	110	-
Flexural strength, MPa	120	130	160	170

Table 3.2: Laser processing parameters (Values from [23])

Material	CT707	CT708	CT802	CeramTape GC
Diode current, A	27.0	28.0	28.0	29.5
Pulse frequency, kHz	8	8	8	10
Beam speed, mm/s	20	25	25	15

Table 3.3: Belt furnace firing parameters (Values from [23])

(Heraeus tapes have the same firing parameters)

Temperature, °C	T1	T2	T3	T4	T5	T6	Speed
Heraeus tapes	350	580	880	880	876	873	2.9.0
CeramTape GC	350	580	859	900	900	851	4.5.0

3.2 Conductive paste characterization

Silver based paste used for creating lines and structures in LTCC are produced in similar way as the green sheet tapes. They consist of a slurry mixture of metallic garnets mixed with organic binders and combining agents exported in a very viscous state and kept in the refrigerator at temperature of only few degrees. Manufacturers deliver datasheets with some of the paste's characteristics but these vary significantly when different production processes are used. The most crucial characteristic of the paste for the coil design is its resistivity, and in the following sections this parameter is thoroughly outlined.

3.2.1 Four-point resistance measurement

In order to measure the resistivity of the paste, a structure was designed that resembles a track of the width w and length l (Figure 3.3). Test structures were fabricated with the standard procedure described in previous sections. A standard four-point method was used to measure the resistance of the sample: a known current was fed through the track and the voltage was measured between two equipotential lines. Resistance R was measured with the ohmmeter and the specific resistivity ρ was calculated using formula $\rho = R \cdot wd/l$.

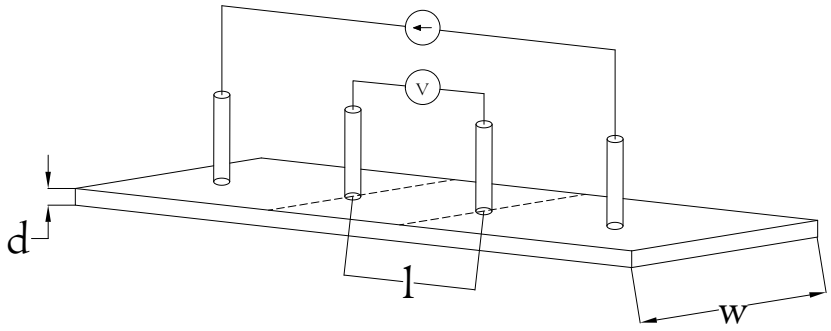

Figure 3.3: Setup for the paste resistivity measurements. Equipotential lines are shown in dashed style.

3.2.2 Van der Pauw method for resistance measurement

Aforementioned method may not be the best one if we are not sure in our knowledge about sample geometry. L. J. van der Pauw developed a technique for measuring resistance (and the sheet resistance), of thin and flat conductive and semi-conductive structures [59]. This method assumes few conditions:

1. The sample thickness d is sufficiently small with the respect to lateral dimensions
2. The contacts are point-like and placed at the circumference of the sample
3. The sample is isotropic and equally thick across the entire area
4. The surface of the sample does not have any isolated holes

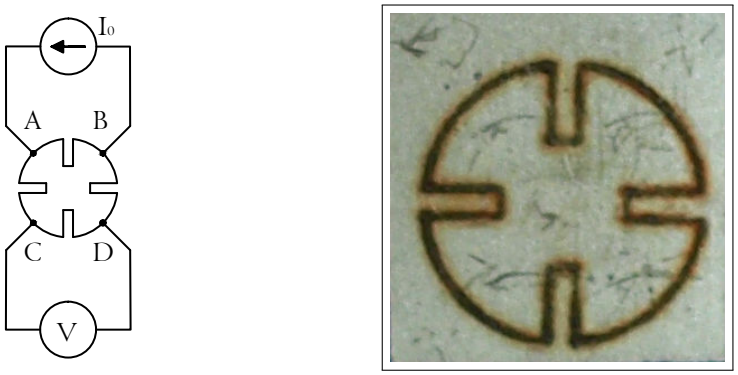

(a) (b)

Figure 3.4: (a) Cloverleaf sample layout for the van der Pauw measurement and (b) laser-cut cloverleaf structure on the conductive surface. By applying a constant current I_0 between contacts A and B and measuring a voltage between contacts C and D, one can calculate resistance $R_{AB,CD}$. In similar way, resistance $R_{BC,AD}$ is calculated if current flows between B and C and voltage is measured between A and D.

Measuring resistance using van der Pauw method requires four contacts on the edge of our sample, symmetrically distributed at the edges of the samples. In the literature the so called "cloverleaf" configuration is the most recommended one (Figure 3.4a).

The specific resistance of the conductor layer can be calculated using the following relation:

$$\rho = \frac{\pi d}{\ln 2}\left(\frac{R_{AB,CD}+R_{BC,AD}}{2}\right) f\left(\frac{R_{AB,CD}}{R_{BC,AD}}\right) \tag{3.1}$$

Herein, the $R_{AB,CD}$ denotes the resistance calculated as a voltage measured between contacts C and D divided while a current from a constant current source flows between contacts A and B and $R_{BC,AD}$ is similarly the resistance measured between contacts A and D while a known current flows between contacts B and C. The value of f can be calculated with the help of numerical methods using the expression (3.2):

$$\frac{R_{AB,CD}-R_{BC,AD}}{R_{AB,CD}+R_{BC,AD}} = f \cdot \operatorname{arccosh}\left(\frac{\exp(\ln 2/f)}{2}\right) \tag{3.2}$$

Assuming uniform thickness d of the sample, the sheet resistance can be directly calculated as $R_S = \rho/d$. The formula is valid only if, along with the aforementioned conditions, contacts A and D are on sample's axis of symmetry and contacts B and C are symmetric with respect to this axis.

3.2.3 Paste measurements and results

For both measurements, four-contact and van der Pauw, the setup included a precise current source TT QL355, a Keithly 2000 multimeter, a probe head with different contact positions and a firm stand for sample positioning (Figure 3.5). High precision current source was used to apply a current of 200 mA, with precision of 0.1 mA, and Keithley multimeter, with voltage resolution of 0.1 µV was used to measure voltage on the voltage terminals. Two probe heads were used, one with linearly spaced (1 mm) contacts for 4-point resistivity measurement and another one with quadratically arranged contacts for van der Pauw measurement.

Two different pastes were characterized: TC7306A and TC7306A. TC7304A is a Ag-paste purely for via filling, whereas TC7306A is a pure Ag conductor paste.

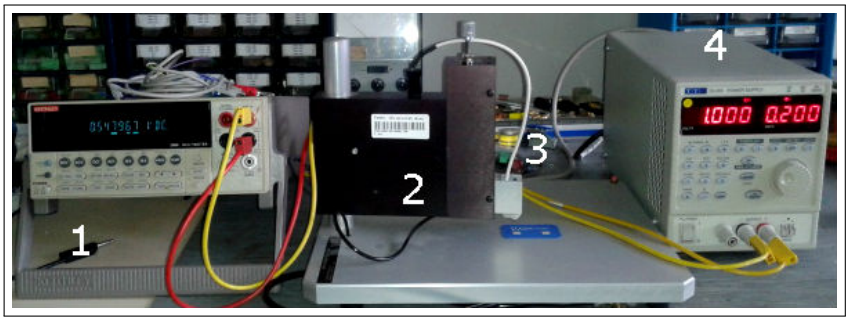

Figure 3.5: Laboratory setup for the resistivity measurement: 1) high-precision voltmeter, 2) stand, 3) probe head and 4) current source.

Both are compatible with the tapes CT800 and CT70x during the co-firing process. TC7306A is intended to be printed with the screen printer and it is somewhat less viscous that TC7304A. The reason for that lays in the technique of screen-printing: if the paste is too viscous, it will not spread adequately after the printing and the screen's mesh will remain patterned in the track. That is why the conductor paste contains more organic binders and liquefying agents which will increase its resistivity.

Test structures for the four-point and van der Pauw measurements were rectangular track and cloverleaf, respectively. While the tracks were printed by standard screen printing method, the cloverleaf structure was derived with some alternations. First a rectangle with surface larger than that of the cloverleaf was printed and co-fired. Afterwards, the cloverleaf structure was cut out of the rectangle with a laser (Figure 3.4b). The reason for this procedure is the demand for the high uniformity of the thickness in the sample when employing van der Pauw's method. Paste thickness variations due to the screen printing were avoided in this way.

Thickness and line quality of the produced samples were determined with the help of an optical profilometer by FRT GmbH. Width and thickness of the printed tracks were established as 0.95 mm and 5 µm. Resistivity values as found by 4-point measurements are given in the table 3.4, while sheet resistance values obtained by the van der Pauw method are shown in the table 3.5.

The influence of the track orientation to the direction of the screen printer was examined in the following way: A series of the equally sized rectangular tracks was printed on a single substrate, but in different orientations from 0° to 90°. The tracks were measured with four-point methods and results shown graph 3.6.

Table 3.4: Paste resistivity measurement results. For comparison, pure silver has resistivity of $1.59 \times 10^{-8}\,\Omega\,\mathrm{m}$ and copper $1.68 \times 10^{-8}\,\Omega\,\mathrm{m}$

Paste	R, mΩ	$\rho, 10^{-8}\ \Omega\,\mathrm{m}$
TC7304A	1.46	1.67
TC7306A	2.54	2.90

Table 3.5: Paste sheet resistance measurement results

Paste	$R_{AB,CD}$, mΩ	$R_{BC,AD}$, mΩ	f	R_S, mΩ
TC7304A	0.184	0.199	≈ 1	0.867
TC7306A	0.3315	0.3335	≈ 1	1.507

The via fill paste TC7304 shows lower resistivity than the conductor paste TC7306. This was expected because via fill paste contains less binders and non-metallic con-

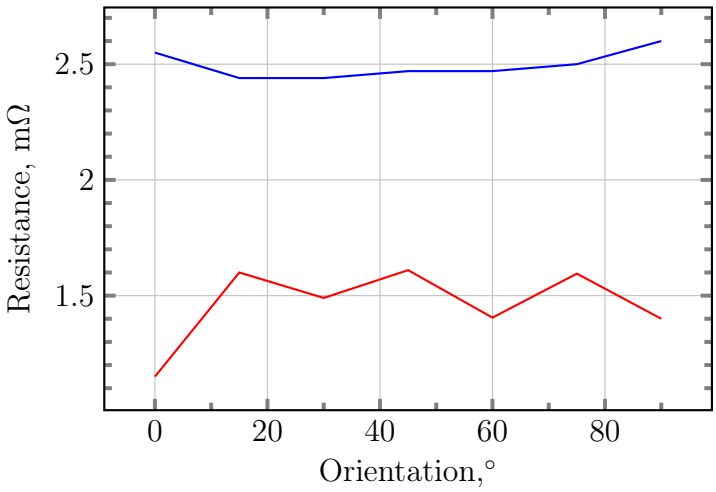

Figure 3.6: Resistance of the silver tracks in dependence of the orientation to the screen printer direction. TC7306 is presented with the blue line and TC7304 with the red one.

stituents which makes it more viscous and less prone to leakage out of the via hole. The viscous nature of TC7304 can be seen on the graph 3.6 where its resistance, in contrast to constant resistance of TC7306, changes in "zigzag" manner. As the orientation varies, the paste exhibits lower and higher resistance, repetitively. This can be attributed to the fine mesh structure of the screen, whose meshing elements are microscopic parallelograms with one dominant axis. When the paste is distributed along the dominant axis, its adherence is better and results in lower resistance, and vice versa.

3.3 Ceramic substrate characterization

Over the years in the Laboratory for Ceramic Technologies (ICeT) many dielectric tapes were characterized and their electrical, mechanical and thermal properties measured and published in many scientific journals and conference proceedings ([56],[55], [23], and [54]). In this section I will lay down measurement methods and results of permittivity (ε) measurements of dielectric LTCC tapes as presented in those works. Available tapes were the CT family from Heraeus GmbH, the CeramTape GC family from CeramTec, and the ESL 900x family from ESL.

A simple plate capacitors were fabricated with the aforementioned tapes as dielectric substrates of thickness d. Silver printed paste served as the round shaped capacitor plates of surface A whose capacitance was $C = \varepsilon A/d$. The capacitance measurements have been performed with high frequency LCR meter Wayne Kerr 6500P in a range 20 Hz– 20 MHz at 23 ± 1 °C room temperature and 30 ± 5 % relative humidity. The permittivity of the capacitor is represented as a complex number $\varepsilon = \varepsilon_0 (\varepsilon'_r - j\varepsilon''_r)$, ε_0 being vacuum permittivity 8.854 $\cdot 10^{-4}$ F m^{-1} and ε''_r and ε''_r imaginary and real part of the dielectric constants that are related as

$$\frac{\varepsilon''_r}{\varepsilon'_r} = \tan\delta = \frac{1}{Q}, \tag{3.3}$$

where $\tan\delta$ is so called *dielectric loss*, *loss tangent* or *dissipation factor* and Q material's *quality factor* [60, p.460]. Dielectric loss represents resistive losses within the material and is a measure of a material's dielectric quality. Ceramic materials are famous to have the lowest dielectric losses of all conventional materials ([53]). Obtained results are shown in the table 3.1, and are slightly larger than of pure

ceramics. Magnetic properties of dielectric LTCC materials are considered to be completely diamagnetic and therefore no special measurements were performed.

Chapter 4

LTCC Coils Design and Simulations

The following chapter presents physical models of LTCC coils intended for NMR spectrometry. Using analytical tools and integral calculus, parameters which help to provide a first hand insight in the performance of the coil are given. These models are intended to focus on the most descriptive parameters of the coil and an estimation of the signal-to-noise ratio per unit volume rather than to consider the geometry of the coils in all details. According to formula 2.20, where SNR_{puv} is the ratio of the magnetic field induced per unit current and the square root of the coil's ohmic resistance, the analysis seeks to lay down the estimation of B-field along the region of interest and the expression for the resistance. A somewhat more detailed view on the coil's characteristics is given in the second part of the chapter, where finite-element method simulations were employed to find electrical characteristics in both DC and AC conditions.

4.1 Quasi-solenoid 3D coil

Standard fabrication of LTCC materials only allows a treatment of each layer alone, considering every layer as a two-dimensional structure, so the fabrication of the classical solenoid form is unachievable. Its best resemblance, a type of coil called a "quasi-solenoid" can be produced with more or less similar properties as the solenoid. A quasi-solenoid presented in this thesis [13] is a type of the coil whose windings are placed half-by-half parallel to each other in mirrored and non-mirrored manner interchangeably, with a certain spacing in between (Figure 4.1). In this configuration, each winding is treated as a half-circle printed on one layer of the LTCC tape and stacked among the other, same looking layers in a way that two neighboring layers, i.e. half-circles, are facing opposite directions. The half-circles are interconnected by vias through the LTCC layers in a way that the vias in two neighboring layers come to the opposite ends of the half-circle. For every point of the quasi-solenoid, except vias, the tangent line makes a constant angle with the axis of symmetry, what partially meets the criterion of the helix curve. Because of the stepwise increment of the coil windings, homogeneity of magnetic filed is significantly deteriorated. While an ideal solenoid coil is considered to have only one magnetic field component, that along the axis of symmetry, quasi-solenoid will have strongly emphasized transversal components. In this section a mathematical analysis of this field using the Biot-Savart law and numerical methods is presented.

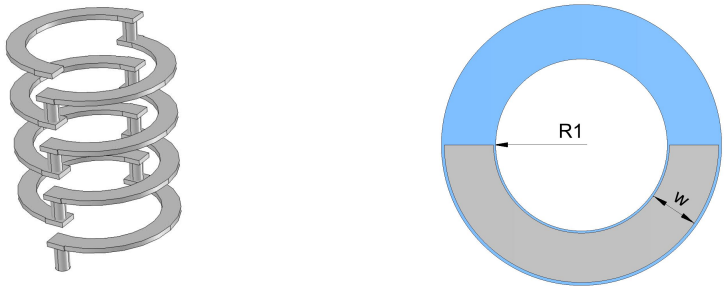

(a) (b)

Figure 4.1: An illustration of the quasi-solenoid without LTCC substrate (a) and its top view layout on a substrate (blue) (b).

4.1.1 Analytical model of quasi-solenoid coil

Magnetic field of the quasi-solenoid

The analytical model section in this chapter is intended to mathematically express the signal-to-noise ratio of the NMR experiment performed with the quasi-solenoid coil in LTCC in respect to the coil's geometry parameters. According to formula 2.20, which says that SNR_{puv} is proportional to the ratio $\hat{B}_1/\sqrt{R_c}$, the analysis starts with the magnetic field distribution made by one semi-circular track (Figure 4.2). To do this, we apply the Biot-Savart law of magnetic induction, which gives the magnetic field $\vec{B}$, generated by the electrical current I flowing through line element dl. The track has an inner radius R_1, width w and outer radius $R_2 = R_1 + w$ and the surface current density $dI = I/(R_2 - R_1)dr_0$, which is assumed to be uniform along the cross section of the track. The field produced along the z-axis, which is chosen to be coil symmetry axis, by current element dl is:

$$\vec{B}_1(0,0,z) = \frac{\mu_0 I}{4\pi w}\int_0^{\pi}\int_{R_1}^{R_2}\frac{zr_0\vec{a}_r + r_0^2\vec{a}_z}{(r_0^2+z^2)^{\frac{3}{2}}}dr_0 d\theta \tag{4.1}$$

By integrating the r-component in polar coordinates over the region $[0,\pi]$, it can be easily shown that the resulting vector has a component in one direction in Cartesian x-y plane, if $z \neq 0$. This happens due to the symmetry of the semi-circular track; for a complete circular track the r-component would completely vanish. By choosing the y-component as the non-zero one, we get the field expressions:

$$\begin{aligned} B_{1y} &= \frac{\mu_0 I z}{2\pi w}\left[\frac{1}{\sqrt{R_1^2+z^2}} - \frac{1}{\sqrt{R_2^2+z^2}}\right] \\ B_{1z} &= \frac{\mu_0 I}{4w}\left[\ln\left(\frac{R_2+\sqrt{R_2^2+z^2}}{R_1+\sqrt{R_1^2+z^2}}\right) + \frac{R_1}{\sqrt{R_1^2+z^2}} - \frac{R_2}{\sqrt{R_2^2+z^2}}\right] \end{aligned} \tag{4.2}$$

The above written expression (4.2) completely corresponds to the solution of similar problem presented in [61, p.24]. Taking in consideration that the quasi-solenoid consists of N layers of semi-circular tracks, we can write field equations (4.2) as a superposition of the fields produced by each track. Having in mind that the tracks are at the distance d from one another and assuming that the first track (most

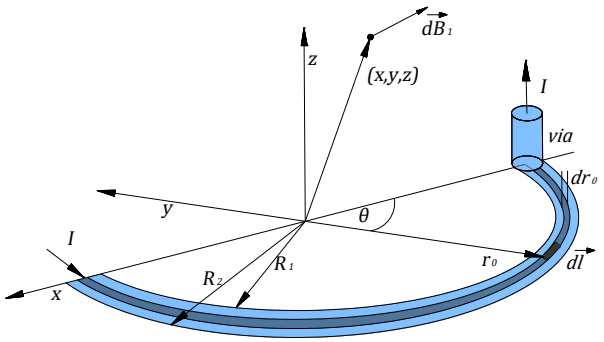

Figure 4.2: Differential field $d\vec{B}_1$ produced by the current I through the line element $\vec{dl}$ of the semi circular track with the inner radius R_1 and outer radius R_2.

bottom one) lies at $z = 0$ components of the $\hat{B}_1 = B_1/I$ become:

$$\begin{aligned}
\hat{B}_{1y} &= \frac{\mu_0 z}{2\pi w} \sum_{n=0}^{N-1} (-1)^n \left[\frac{1}{\sqrt{R_1^2 + (z-nd)^2}} - \frac{1}{\sqrt{R_2^2 + (z-nd)^2}} \right] \\
\hat{B}_{1z} &= \frac{\mu_0}{4w} \sum_{n=0}^{N-1} \left[\ln \left(\frac{R_2 + \sqrt{R_2^2 + (z-nd)^2}}{R_1 + \sqrt{R_1^2 + (z-nd)^2}} \right) \right. \\
&\qquad \left. + \frac{1}{\sqrt{R_1^2 + (z-nd)^2}} - \frac{1}{\sqrt{R_2^2 + (z-nd)^2}} \right]
\end{aligned} \tag{4.3}$$

The factor $(-1)^n$ comes from the fact that every second semi-circular track lays in the mirrored direction from the previous one implying that y-component will act in the opposite direction on the y-axis.

Magnetic field contributed by vias

On a very similar basis we can calculate the magnetic field contributed by vias. Firstly, the magnetic field of a single via shall be deduced. Imagining via as a simple wire element of length d, through which the current I is flowing, placed at the coordinates $(R_1, 0, 0)$, we can calculate the magnetic field at any point on the symmetry axis $(0, 0, z)$. According to the Biot-Savart law of a single current line, the field produced by vias only has a transversal y-component:

$$B_{y,via} = \frac{\mu_0 I}{4\pi} \left(\frac{d-z}{\sqrt{R_1^2 + (z-d)^2}} + \frac{z}{\sqrt{R_1^2 + z^2}} \right). \tag{4.4}$$

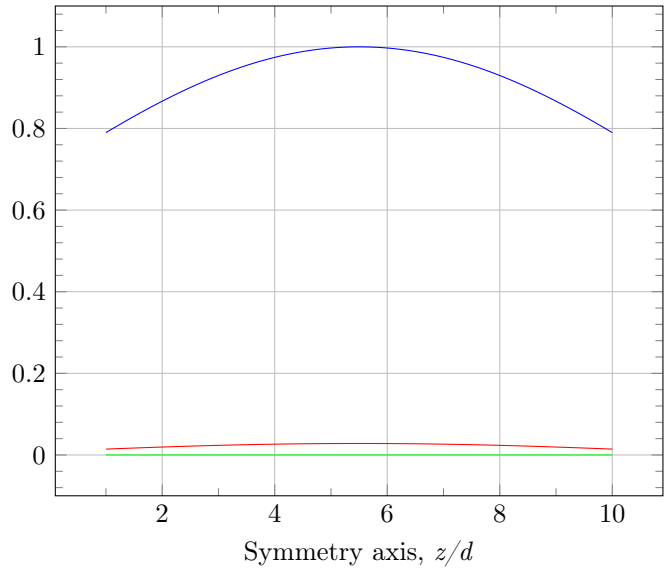

Figure 4.3: Relative ratio of the B-field components, as calculated in equations (4.3) and (4.5): z-component (blue line), y-component (red line) and y component contributed from vias (green line). Number of half-windings is 10.

Similarly as in formula (4.3), we can express the the magnetic field along the z-axis of N vias spaced by distance d as:

$$\hat{B}_{y,via} = \frac{\mu_0}{4\pi} \sum_{n=0}^{N-1} (-1)^n \left(\frac{d(n+1) - z}{\sqrt{R_1^2 + [z - (n+1)d]^2}} + \frac{(z - nd)}{\sqrt{R_1^2 + (z - nd)^2}} \right). \tag{4.5}$$

As can be seen on figure 4.3, y-components of B are significantly lower than z-component. As a matter of fact, for 10 half-windings, their ratio is 1:0.03 and decreases with higher number of half-windings, which is due to the alteration factor $(-1)^n$. It is also visible that the maximum field strength appears in the middle of the coil, which is easily understood from symmetry reasons. Figure 4.4 depicts how $|B|$ varies with number of layers N with constant distance d, and shows that for increasing number of layers, $|B|$ reaches its maximum value beyond which it doesn't increase any more. While it may seen counter-intuitive on the first thought, it is well in accordance with the known theory of classic solenoid coils. For a large number of windings, the quasi solenoid resembles a classical solenoid whose field along the axis is $B_{solenoid} = \mu_0 NI/L_c$. Knowing that coil length L_c increases with the number of layers as $L_c = Nd$ where d is spacing between the layers, the field will be constant and independent on N:

$$B = \mu_0 \frac{NI}{L_c} = \mu_0 \frac{NI}{Nd} = \mu_0 \frac{I}{d}. \tag{4.6}$$

Resistance of the coil and signal-to-noise ratio

To calculate the resistance of the coil, we use the standard formula for the resistance of track of width w and length l. Knowing that sheet-resistance of the track is R_S, the total resistance will be:

$$R_{tot} = R_S \frac{l}{w} \tag{4.7}$$

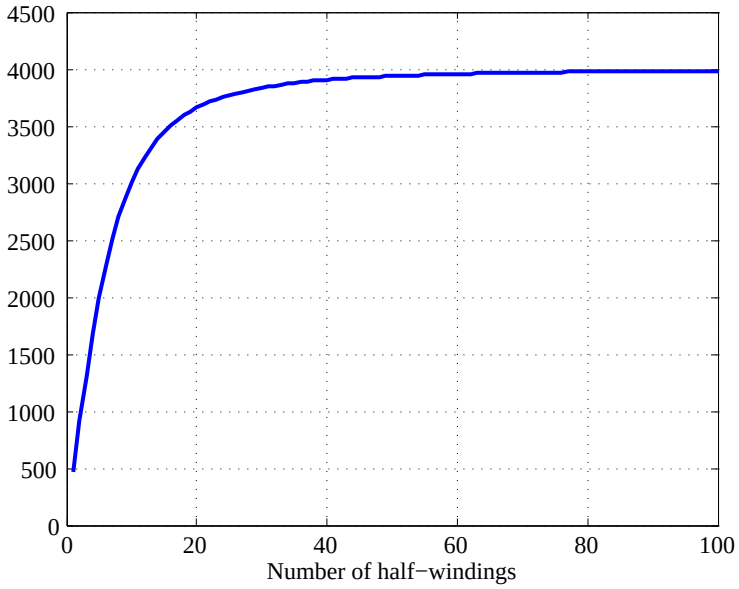

Figure 4.4: Dependence of $|B|$ in the middle of the coil on number of windings N.

Having in mind the shape of the track (Figure 4.1) we can conclude that total length of the coil is $l = N(R_1 + R_2)\pi$, what makes resistance of the solenoid tracks

$$R = NR_S \frac{(R_1 + R_2)\pi}{w} \tag{4.8}$$

While we could neglect the influence of the interconnection vias in the field analysis, the same can not be done in resistance calculation. Knowing that the length of the vias is exactly spacing between two tracks d, and that the radius of the via is r_v, the total resistance of the quasi-solenoid is:

$$R = NR_S \frac{(R_1 + R_2)\pi}{w} + N\rho \frac{d}{r_v^2 \pi} \tag{4.9}$$

where ρ is specific resistivity of the via filling paste.

The signal-to-noise ratio per unit volume (SNR_{puv}) is, as explained in chapter 2, proportional to the ratio of the magnetic field produced at the center of the coil per unit current and the square root of the coil resistance R. That said, SNR_{puv} is given by ratio of the formulae (4.3) and (4.9) times a factor given by the sample geometry and the conditions of the NMR experiment. With the assumption we can observe how SNR_{puv} depends on geometrical parameters of the coil and find the optimum ones. This dependence is presented in Figure 4.5.

What is immediately visible in the Figure 4.5 is that SNR_{puv} drops drastically with the increasing radius of the solenoid as well as with the increasing spacing between the layers. There is no meaningful way to optimize SNR_{puv} of the solenoid in respect to these two parameters except making the diameter and the spacing as small as the sample allows. On the other hand, SNR_{puv} clearly has a local maximum for given values of N and w. These maxima can be understood as a consequence of an increasing resistance with the higher N. While it is true that the magnetic field also rises with the number of layers, at certain point the curve loses linearity and becomes independent on N. For the increasing w, the effective area of the coil becomes larger

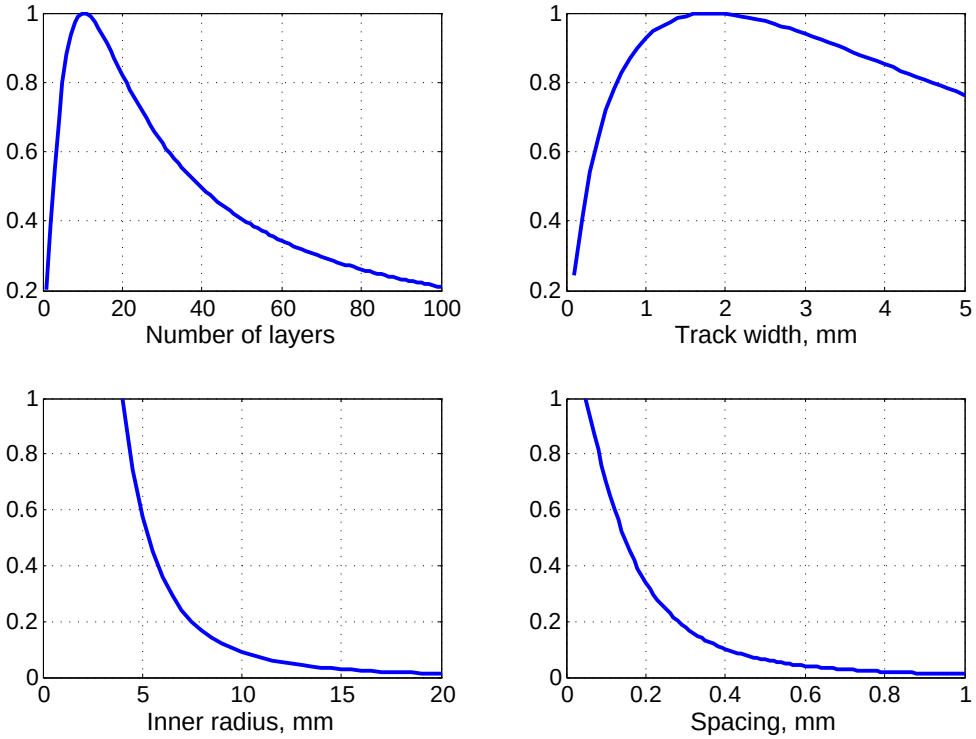

Figure 4.5: Dependence of the SNR_{puv} (normalized) upon a) number of layers N, b) track width w, c) inner radius R_1 and d) spacing between the layers d.

and the field in the middle of the coil does not follow the same distribution as for a thin wire solenoid. All this means that coil certainly can be optimized in respect to the number of half-windings and the track width. Knowing these values for each coil size enables one to find a maximum NMR signal intensity for the same sample volume.

4.2 Planar coils

A planar or surface coils are a kind of coils where the silver printed tracks form a two dimensional structure on a single LTCC substrate. The conductive lines form a spiral of circular or rectangular shape. Planar coils have found broad usage in NMR microscopy systems since their field homogeneity is suitable for biological cell analysis [46]. The structure studied in this chapter is an Archimedean type spiral (Figure 4.6a).

4.2.1 Analytical model of the planar spiral coil

Eroglu *et al.* in [37, 35] and [42] reviewed the design and performance of the spiral surface microcoils and their importance in NMR spectrometry. Significant contributions in mathematical model of the spiral coils is presented by Massin *et al.* in [43, 44, 45] and [46].The following analysis has been taken and accordingly modified from the one in [37]. A mathematical equation describing the Archimedean spiral in polar coordinates is given as $r = a\theta$ where a is a spiral constant, r is the radial coordinate of a point on the spiral and θ is the angular coordinate in radians of the

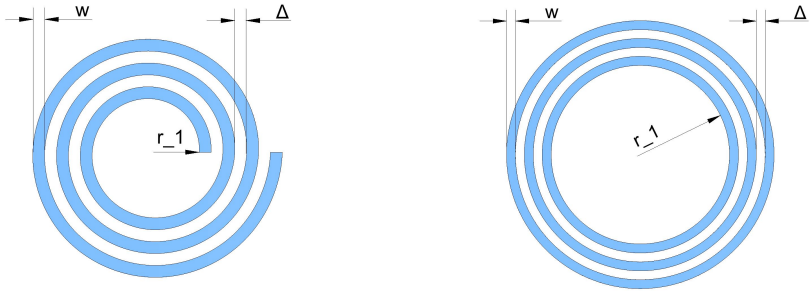

(a) (b)

Figure 4.6: a) Archimedean spiral coil layout and b) its nested circular track representation

same point. The spacing Δ between the turns is related to the spiral constant by the equation $\Delta = 2\pi a$. It was assumed that the NMR signal comes from the points along the central axis normal to the plane of the coil. The magnetic field everywhere along the axis of the spiral coil (z-axis) can be easily found by treating coil wires as infinitely thin filaments and by using the Biot-Savart law:

$$\vec{B}_1 = \frac{\mu_0 I}{4\pi} \int_{\theta_1}^{\theta_2} \left(\frac{a/z^2 \theta}{\left[(a/z)^2 \theta^2 + 1 \right]^{\frac{3}{2}}} \hat{a}_r + \frac{(a/z)^2 \theta^2}{\left[(a/z)^2 \theta^2 + 1 \right]^{\frac{3}{2}}} \hat{a}_z \right) d\theta \tag{4.10}$$

where θ_1 and θ_2 are angles associated with initial and final points on the spiral, respectively. The number of turns, N, in terms of angles is given by $2\pi N = \theta_2 - \theta_1$. The initial radius of the spiral is related to the initial point angle by $r_1 = 2\pi\theta_1$.

The total z-component per unit current along the z-axis is calculated to be:

$$\hat{B}_1 = \frac{\mu_0}{2\Delta} \left(\frac{\theta_1}{\sqrt{\theta_1^2 + \lambda^2}} - \frac{\theta_2}{\sqrt{\theta_2^2 + \lambda^2}} + \ln \frac{\theta_2 + \sqrt{\theta_2^2 + \lambda^2}}{\theta_1 + \sqrt{\theta_1^2 + \lambda^2}} \right). \tag{4.11}$$

where parameter $\lambda = 2\pi z/\Delta$ represents the z-coordinate of the observation point scaled by the spiral constant.

Resistive losses and SNR of the planar spiral coil

The resistance and, more generally, resistive losses of the coil can be calculated as Eroglu *et al.* have shown in [35]. In their analysis the total coil resistance consists of two parts. First part, the AC resistance R_c, takes the confinement of the current within the skin depth into account. The second contribution R_{eddy} stems from magnetic inter-turn interactions including eddy-currents, and thereby current inhomogeneities in what is called a *proximity effect*. This effect becomes dominant as the number of turns increases. Total losses are estimated as the sum of the two: $R_c + R_{eddy}$.

This paper considers spiral coils having conductor traces of rectangular cross section whose width w is several times larger than their thickness, t. Both w and t are assumed to be much greater than the electrical skin depth δ. In such cases the AC resistance of the coil can be approximated by the product of the coil's length and resistivity divided by the skin effect reduced conductor cross section. Because the total length of an Archimedean spiral can be computed using the standard formula for arc length the coil's AC resistance is given as:

$$R_c = \rho\frac{l}{A} = \frac{\rho}{wt - [(w-2\delta)(t-2\delta)]}\int_{\theta_1}^{\theta_2} a\sqrt{1+\theta^2}d\theta$$
$$\cong \frac{\rho\Delta}{8\pi w\delta}\left[\theta_2\sqrt{\theta_2^2+1} - \theta_1\sqrt{\theta_1^2+1} + \ln\frac{\theta_2+\sqrt{\theta_2^2+1}}{\theta_1+\sqrt{\theta_1^2+1}}\right] \tag{4.12}$$

The estimate of the proximity losses is based on the principle that eddy current losses induced in conductors can be bounded from above and estimated using the expression

$$L_{int} \leq \frac{\omega^2\sigma t}{2}\int_S \left|\vec{A}\right|^2 dS \tag{4.13}$$

where ω is frequency, σ is the conductivity and t is the thickness of the conductor, S is planar region occupied by the conductor and $\vec{A}$ is the magnetic vector potential due to the injected current when it is uniformly distributed in the cross section of the conductor traces. Two additional assumptions will be made in order to compute an estimate of the proximity losses using equation 4.13. One is that the spiral will be replaced by a sequence of concentric circular traces in order to have a closed form expression for the vector potential in terms of Legendre polynomials. The other is that only the first few terms in the series expansion of the square of the vector potential will be retained. Only the vector potential created by the i-th turn over the area of the j-th turn for all possible different i and j is taken in account, because the influence of each turn on itself has already been incorporated in relation (4.12). It accounts for losses due to interactions of the turns and is given by the following formula

$$L_{int}(N, w, \Delta) = 2\sum_{i=1}^{N-1}\sum_{j=i+1}^{N} L_{ij}(r_i, r_j) \tag{4.14}$$

where

$$L_{ij}(r_i, r_j) \approx 2\pi\omega^2\sigma t\int_{r_j-w/2}^{r_j+w/2}\left|\vec{A}_i\right|^2 r dr \tag{4.15}$$

and $\vec{A}_i$ is the magnetic vector potential generated by the i-th loop.

The magnetic vector potential due to a circular trace of width w and radius r_i carrying a linear current density J, can be found for any point with the coordinates r and θ inside the conductor circle:

$$A_i(r,\theta) = -\frac{\mu_0 J}{4} r\ln\left(\frac{r_{i+}}{r_{i-}}\right)P_1^1(\cos\theta)$$
$$-\frac{\mu_0 J}{4}\sum_{n=1}^{\infty}\frac{(-1)^n(2n-1)!!}{2^{n+1}n(n+1)!}r^{2n+1}\left(\frac{1}{r_{i+}^{2n}} - \frac{1}{r_{i+}^{2n}}\right)P_{2n+1}^1(\cos\theta) \tag{4.16}$$

where $P_n(\cos\theta)$ are n-th Legendre polynomials. Squaring the vector potential in equation (4.16), keeping all the terms up to the order r^8 of the resulting infinite series expansion and integrating the result according to equation (4.15), the following

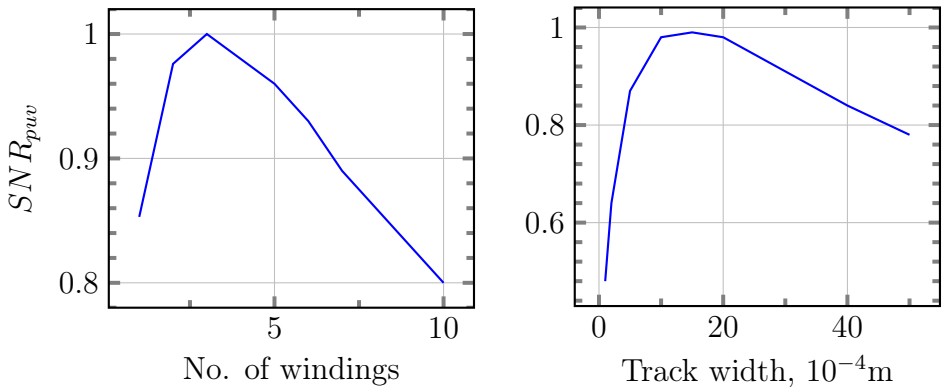

(a) Constant parameters: $r_1 = 2.5\,\text{mm}$, $w_1 = \Delta = 100\,\mu\text{m}$

(b) Constant parameters: $r_1 = 2.5\,\text{mm}$, $\Delta = 100\,\mu\text{m}$, No. of turns = 3

Figure 4.7: Normalized SNR per unit volume for the surface spiral coil vs. number of turns and track width.

expression for L_{ij} is obtained:

$$L_{int}(N,w,\Delta,r_0) \approx \frac{\mu_0 \pi J^2 \omega^2 \sigma t}{2} \sum_{i=1}^{N-1} \sum_{j=i+1}^{N} \tag{4.17}$$
$$\left\{ 0.25 \left[\ln\left(\frac{r_{i+}}{r_{i-}}\right) \right]^2 \left(r_{j+}^4 - r_{j-}^4\right) + 0.0625 \ln\left(\frac{r_{i+}}{r_{i-}}\right) \left(\frac{1}{r_{i-}^2} - \frac{1}{r_{i+}^2}\right) \left(r_{j+}^6 - r_{j-}^6\right) \right.$$
$$\left. + \left[4.4 \cdot 10^{-3} \left(\frac{1}{r_{i-}^2} - \frac{1}{r_{i+}^2}\right)^2 + 0.0146 \ln\left(\frac{r_{i+}}{r_{i-}}\right) \left(\frac{1}{r_{i-}^4} - \frac{1}{r_{i+}^4}\right) \right] \left(r_{j+}^8 - r_{j-}^8\right) \right\}$$

where r_{i+} and r_{i-} stand for $r_i + w/2$ and $r_i - w/2$, respectively. The total resistance of the coil is then found using the expression

$$R_{tot} = R_c + R_{eddy} = R_c + \frac{L_{int}(N,w,\Delta,r_0)}{(Jw)^2} \tag{4.18}$$

The signal-to-noise ratio per unit volume is estimated according to formula (2.20): $SNR_{puv} \propto \hat{B}_1/\sqrt{R_{tot}}$. The graph on the figure 4.7 depicts the dependence of SNR_{puv} on the number of layers and track width. What is immediately visible is the existence of the maximum SNR_{puv} for a certain values of these two parameters. The goal of these analysis is to find these values for each spiral configuration.

4.3 3D spiral coils

Three dimensional spiral coils present a synthesis between quasi-solenoid and planar spiral coils. It is designed so that on each layer of the LTCC tape an Archimedean spiral is printed. Printed tapes were stacked together so that the spiral on one layer faces the spiral on neighboring layer oppositely. Ends of the spirals were connected with vias which in every layer ended up on opposite sides of the ring (Figure 5.5).

4.3.1 Analytical model of 3D spiral coil

The field at the symmetry axis at the center of the coil is modified from equation (4.11) so that each layer superimposes the magnetic field. The parameter $\lambda =$

$2\pi z/\Delta$ again represents the z-coordinate of the observation point scaled by the spiral constant and d' the equally scaled distance between two layers d.

$$\hat{B}_1 = \frac{\mu_0}{2\Delta}\sum_{n=0}^{N}\left(\frac{\theta_1}{\sqrt{\theta_1^2+(\lambda-nd')^2}} - \frac{\theta_2}{\sqrt{\theta_2^2+(\lambda-nd')^2}} + \ln\frac{\theta_2+\sqrt{\theta_2^2+(\lambda-nd')^2}}{\theta_1+\sqrt{\theta_1^2+(\lambda-nd')^2}}\right) \tag{4.19}$$

The resistance of such a coil has been estimated as the sum of coil resistance from eq. (4.12) for all layers, or $N \cdot R_c$, plus the resistance contribution by the vias from eq. (4.9). The expression for the AC resistance of the 3D spiral coil is:

$$R_c = N \cdot \frac{\rho\Delta}{8\pi w\delta}\left[\theta_2\sqrt{\theta_2^2+1} - \theta_1\sqrt{\theta_1^2+1} + \ln\frac{\theta_2+\sqrt{\theta_2^2+1}}{\theta_1+\sqrt{\theta_1^2+1}}\right] + N\rho\frac{d}{r_v^2\pi} \tag{4.20}$$

where ρ is specific resistivity of the via filling paste and the radius of the via is r_v. The signal-to-noise ratio per unit volume of the coil is again calculated with the help of MATLAB using the formula 2.20. The following graphs 4.8 lay the dependence of SNR_{puv} on coil geometry parameters.

Again, there are certain number of layers and windings per layer for which the coil exhibits maximum SNR per unit volume for given sample and experiment conditions. Calculating these values for each coil size enables maximum signal intensity for the same sample volume. Examining the dependence on other parameters such as the track inter-turn spacing, layer or track thickness was considered non-influential on coil SNR and not presented here as it has been shown in previous section that these parameters do not yield local maxima on the graphs.

4.4 Twin horseshoe resonator

Previously analyzed coils present an inductor in classical sense as a component whose impedance in ideal case rises linearly with the frequency and has a phase shift of 90°. But in some applications of NMR, such as magnetic resonance imaging (MRI) systems, different kind of component - the twin horseshoe resonator has found its usage. It has been developed from the transmission line resonator (TLR) where a gap had been cut on its outer conductor. This gap presents a mechanical discontinuity that disturbs normal current flow and consequently the magnetic flux pertaining to the center core of the transmission line is no longer canceled by the current flowing in the outer conductor ([62]).

A twin horseshoe resonator consists of two parallel-plate conductive rings with diagonally opposite gaps separated by a dielectric medium. The natural resonant frequency of such structure is a function of the transmission line propagation constant (β), its characteristic impedance (Z_0), as well as the series inductance (L) of the two loops. The frequency of the resonator can be tuned by varying gap size, or average length of the conductors (X_l), and satisfies equation 4.21.

$$\frac{\omega_0 L}{4Z_0}\tan\left(\frac{\beta X_l}{4}\right) = 1 \tag{4.21}$$

Despite of its apparently simple form, the field distribution of the horseshoe resonator bears a complicated relation with respect to the circuit elements and generated fields. For a given coil size, its natural resonant frequency has been numerically computed with Python programming package. *Comsol* simulation was used to examine RF characteristics of the resonator.

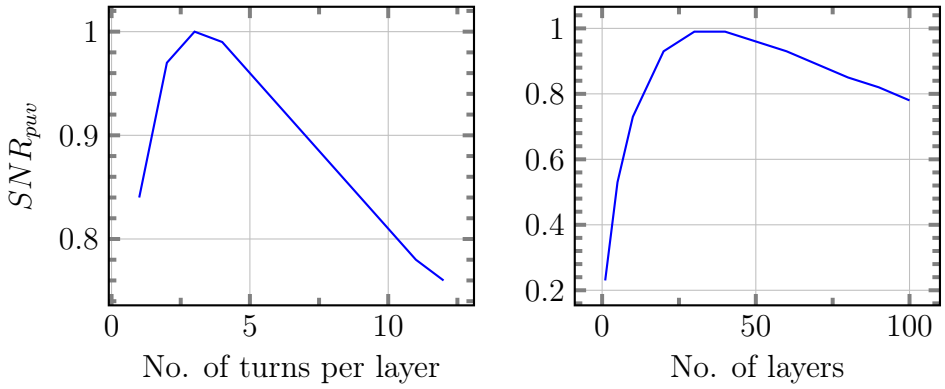

(a) Constant parameters: $r_1 = 2.5\,\text{mm}$, No. of layers = 5, w, Δ=0.5 mm

(b) Constant parameters: $r_1 = 2.5\,\text{mm}$, No. of turns per layer = 2, w, Δ=0.5 mm

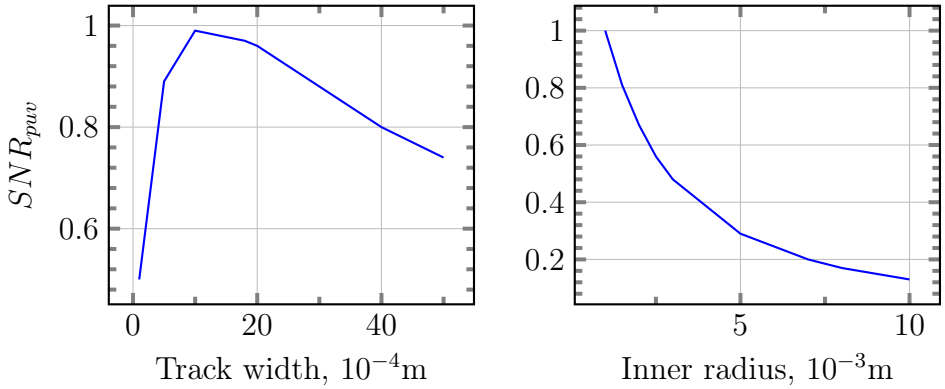

(c) Constant parameters: $r_1 = 2.5\,\text{mm}$, No. of turns per layer = 4, No. of layers = 20

(d) Constant parameters: w, Δ=0.5 mm, No. of turns per layer = 4, No. of layers = 20

Figure 4.8: Normalized SNR per unit volume for varying geometry parameters

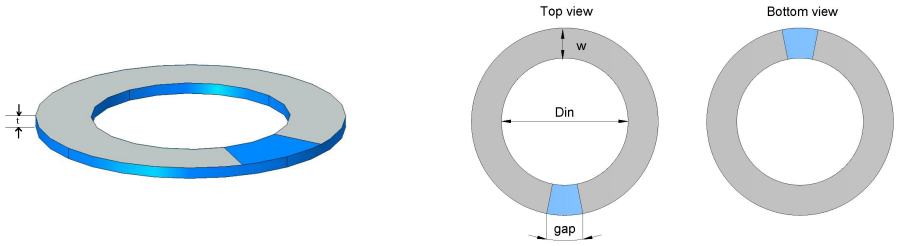

(a) (b)

Figure 4.9: (a) Perspective view and (b) geometrical sketch of the twin horse-shoe resonator

4.5 FEM simulations of the LTCC coils

In order to confirm the analytical description of the coils and get deeper insight into their dynamical characteristics, *finite element method* (FEM) based simulations were performed with the help of the software package *Comsol* [63]. This method relies on defined geometry conditions, equations governing the physics behind the problem and a finite number of elements into which whole geometry is divided. Since there is no way to adequately simulate continuous space where the equations take place, special care has to be taken in defining *boundary conditions*, i.e. the physical values at the limits of the defined geometry. FEM simulation will find a steady-state as well as frequency dependent solution of the Maxwell equations within the region containing coil under test. Boundary conditions will define electric and magnetic field at the edges of that region and one specific boundary will be determined as an excitation (voltage or current one), which finally leads to the creation of the fields in the Maxwell equations.

Once the physics and the geometry of the model is set, the simulation requires the discretization of the model space into finite elements in the process called *mesh*. *Comsol* is based on tetrahedral shaped elements and it offers a possibility to define their size in few different classes, from very coarse to extremely fine. Of course, the finer the mesh is, the more accurate the simulation will be, but it will cost a lot of computational time. That's why the mesh is chosen to accommodate the maximum element size few times within of the minimum geometry entity. Finally, *Comsol* offers different solver configurations, like MUMPS or PARDISO. These are different solvers of large sparse symmetric and unsymmetric linear systems of equations on shared-memory and distributed-memory multiprocessors ([64, 65]). For the purpose of this simulations the difference of the two is not crucial and it was proceeded with the default solver (MUMPS).

Comsol also offers different study types such as stationary, time-domain, frequency domain or eigen-frequency. Dynamic properties of the coil are crucially important for its implementation in NMR experiment. In example, if self-resonance of the coil is below the working frequency of the NMR spectrometer, the coil can not be used in the experiment. Mathematical way of estimating coil AC losses and self-resonant characteristics, as shown in previous sections, turned out to be rather complex and unpractical analysis. That's why the frequency dependent study of the coil comes in place. One extremely useful feature of *Comsol* solvers is the *Parameter Sweep*. It allows the user to pick one of the parameters of the model and make it change its value in few steps within a specified range. As a result, solutions will be presented for each step and compared.

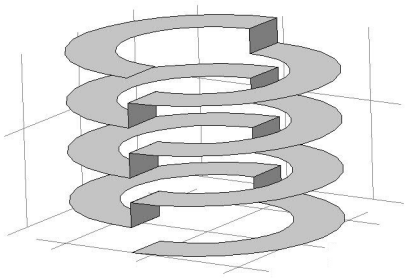

Figure 4.10: Eight-track quasi-solenoid *Comsol* model.

4.5.1 FEM simulation of the quasi-solenoid

Comsol model begins by drawing a 2D or 3D sketch of the coil and its environment, what can be easily done by any CAD (computer-aided design) technique. Geometrical parameters are usually stored in a separate parameter list and can be changed when the sketch has to be re-drawn. Geometrical parameters of the quasi-solenoid coil are

R_1	Inner radius of the coil.
w	Width of the tracks.
d	Spacing between the layers.
N	Number of the half-windings.
t_{track}	Conductive track thickness.
r_o	Via radius.

Since the track thickness t_{paste} is relatively small (cca. 10 µm) compared to the rest of the geometry, track can be drawn as a two-dimensional object, as depicted in Figure 4.10.

The discretization of the vias connecting two adjacent layers depends on the overall geometry. In case where the simulated coil is huge (up to few centimeters), concerning its number of layers and overall size, vias, which are maximally a few hundreds of micrometers long can present a significant problem in dividing the geometry into the small finite elements. The software was unable to resolve the equations due to the huge number of meshing nodes. That's why the vias are presented as tiny rectangles connecting two tracks in relatively big models, like in figure (4.10). The cost of faster and successful computation is lack of accuracy, for the vias are presented in the different way then they are in reality. But, fortunately, due to their minute size, their influence can be neglected. To achieve a solution accurate as possible, we can change the resistivity of the via material in order to have the same resistance as the actual via has. Equations (4.22) explain the principle of determining the resistivity of the substitutionary via ρ' as a function of the actual via radius r_o, conductor layer thickness t_{track}, the track width w and a real resistivity ρ.

$$\begin{aligned} R_v &= R'_v \\ \rho\frac{d}{r_o^2\pi} &= \rho'\frac{d}{wt_{track}} \\ \rho' &= \frac{wt_{track}}{r_o^2\pi}\rho \end{aligned} \tag{4.22}$$

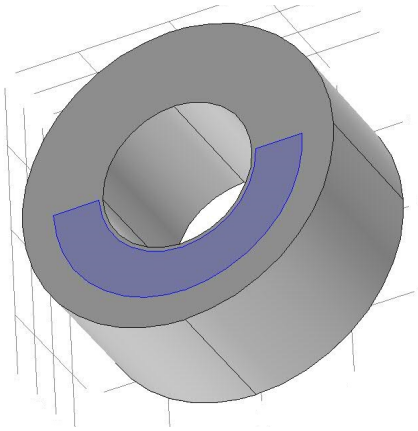

Figure 4.11: Model of the ceramic substrate in which the coil tracks are embedded.

The drawing is complete when two remaining parts are sketched. These are the ceramic substrate and the surrounding air region. The ceramic substrate is drawn as a hollow cylinder which fits the tracks, and the air region is a solid sphere surrounding the coil. The radius of the air sphere is five times outer radius of the coil. This makes model outer boundary far enough from the coil to consider the field values insignificantly low there.

In *Comsol* each of the drawn entities is considered as a domain or a boundary. Both, domains and the boundaries, are assigned to the different materials and for electromagnetic simulations each of these materials need to have defined properties: electric conductivity, relative magnetic permeability and relative electric permittvity. These values are given as obtained in chapter 3. For simplicity relative permittivity and permeability of air are set to 1 and its conductivity to zero. Boundaries assigned to the coil tracks will have resistivity as specified in chapter 3, while boundaries assigned to the via will have resistivity as determined in the formulae 4.22.

DC simulation analysis

The next step in preparation of the model is the definition of the physics which will govern the solution of Maxwell equations. The most suitable packages that *Comsol* offers are the *Electric Current Shell, (ECS)* and the *Magnetic Fields, (MF)* [63]. Within the *ECS* package we define the excitation of the model. This means that one boundary, called the *terminal* is considered to be connected to the voltage or the current source. It is necessary to have another boundary which will be connected to the opposite pole of the source, called *ground*. In the model of quasi-solenoid, the terminal is assigned to the free end of the bottom most track, and ground to the free end of the topmost via (Figure 4.12). The terminal is chosen to be the current type and the assigned current is 1 A. In this way magnetic field will be calculated per unit current.

The package *ECS* will use this assignments with material's electric properties to calculate the current density through the coil and voltage potential distributed over it. The package *MF* will, according to the Biot-Savart law, calculate the magnetic field generated by the current inside of the coil region. To achieve this, we must assign the property called *surface current* to the geometrical entity of the coil. The surface current property requires $x, y,$ and$z$ components of surface current density to be manually entered. These are, of course values calculated in *ECS* `ecs.Jsx`, `ecs.Jsy` and `ecs.Jsz`. Within the *MF* package a few other things are defined: magnetic and electric insulation of the entire geometry as well as initial conditions.

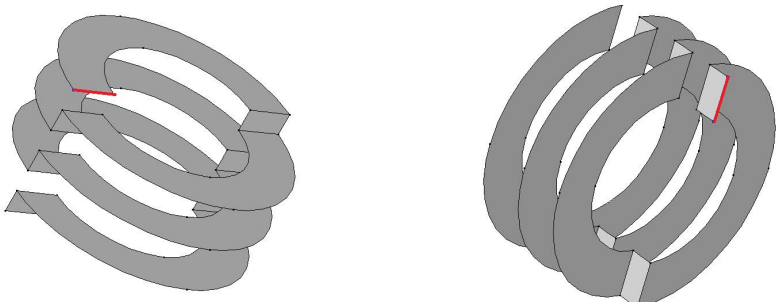

(a) (b)

Figure 4.12: (a) A terminal and (b) ground (red lines) assigned to the 6-track model of the solenoid

The latter shall not be taken into account since the simulation is steady-state only and does not need to calculate transient phenomena.

The results are presented in a graphical mode, like in figure 4.13. The current density and voltage potential distributions can be studied as well as the magnetic field over the entire region. The magnetic field across any desired plane or line within geometry can be extracted in two-dimensional and one-dimensional plots. A post-processing toolkit enables some global variable calculation, such as integrating or averaging. This way one can obtain values for the total magnetic energy or voltage at the terminal, and use them to calculate the inductance and the resistance of the coil. The total energy of the magnetic field is extracted as a volume integral of the magnetic energy density $W_m = \mu |H|^2 /2$. In the *MF* package of *Comsol*, this value is stored as a variable `mf.intWm`. Using the formula for energy stored in the inductor ($E = LI^2/2$), we can find the inductance L of the coil as `L = 2*mf.intWm/ecs.I0_1^2`, where `ecs.I0_1` is terminal current, designated in the *ECS* package. The DC resistance R is found in a similar manner `R = ecs.V0_1/ecs.I0_1`. The quality facor Q is defined as the ratio of the two times the frequency.

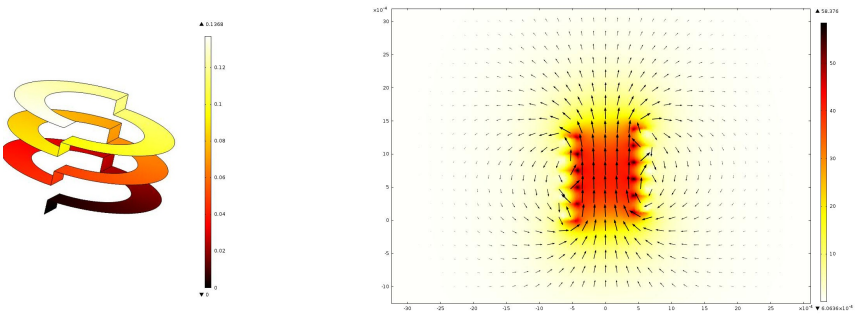

(a) (b)

Figure 4.13: Simulation output for (a) the voltage potential distribution of a 3-layer coil and (b) the B-field distribution of the 12-layer coil. Magnetic field lines, depicted with the arrows strikingly resemble field lines of the solenoidal coil.

The magnetic field along the axis of the symmetry has its maximum in the middle of the coil and is picked at this point to test dependence of the field on the variations of different geometry parameters. The following figure 4.14 and 4.15, present normalized values of L, Q and of the SNR, versus variations of geometrical parameters.

The graphs in figure 4.15 show good matching between the mathematical model

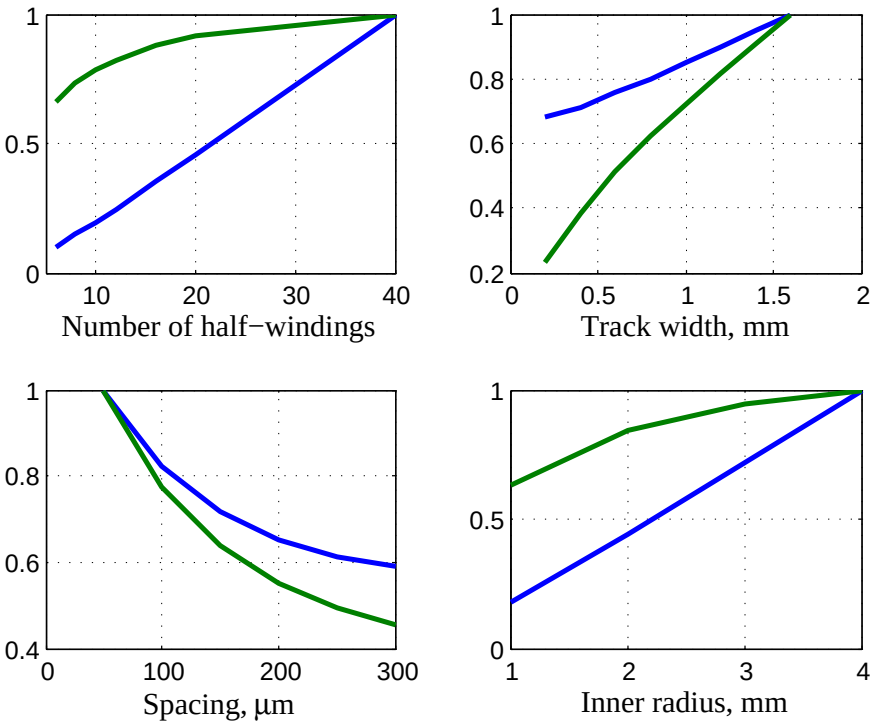

Figure 4.14: Normalized values of L (blue line) and Q (green line) of the quasi-solenoid against different parameters, as obtained by the simulation. Normalization factors are 80, 11, 10 and 133 nH, respectively. Because of DC simulation, Q is only calculated as the ratio of L and R.

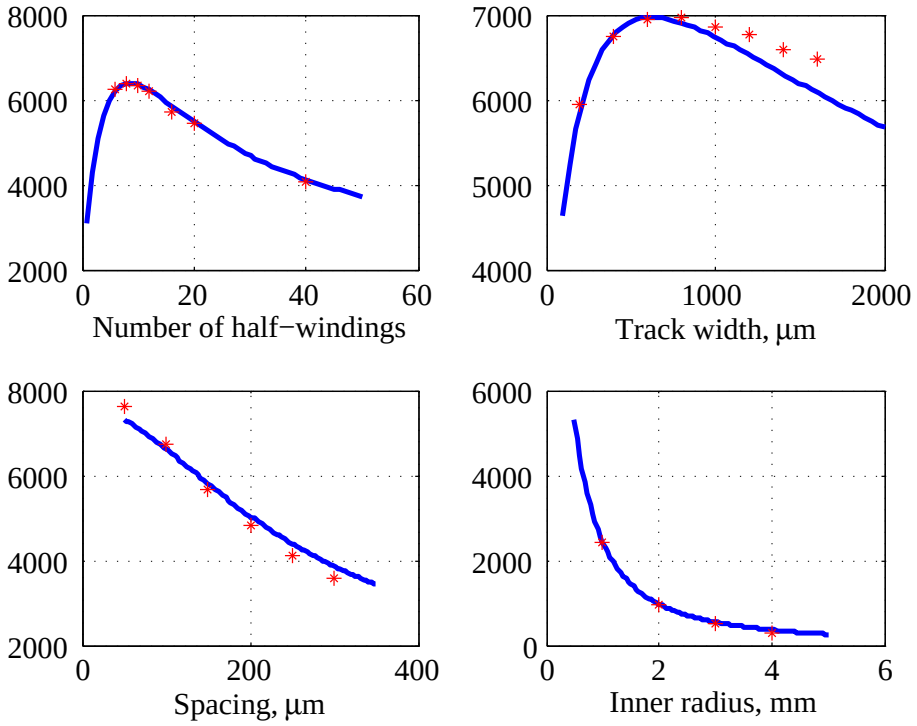

Figure 4.15: $SNR_{p.u.v.}$ of the quasi-solenoid for different geometry parameters. The blue line represents the results of the analytical model from the section 4.1.1, and red asterisks represent discrete outputs from the *Comsol* simulation.

and the numerical simulation. These graphs can be used for manufacturing the coil with the optimal properties for the given geometry. While L and Q have monotonic trend of rising with N, w and R_1 and falling with spacing d, the SNR seems to have a local maximum for the certain values of N and w. This is the main output of the simulation results that can be used for optimizing quasi-solenoidal coil performance.

Homogeneity study

The advantage of the DC simulation is the possibility of visualization of the magnetic field distribution which in turn gives an insight into the field's homogeneity. As said in Chapter 2, the homogeneity of the magnetic field within the coil is crucial to the signal obtained from the NMR experiment. For the quasi-solenoidal coil, the field homogeneity can be described in the following way: Let the ΔB be the difference of the field B_{center} at the center of the sample and the field at the distance d within the coil. For the sample of dimension $d_{sample} < d$ a field homogeneity factor k_0 from 2.19 can be calculated as:

$$k_0, \% = \left(1 - \frac{\Delta B \cdot d_{sample}}{d \cdot B_{center}}\right) \cdot 100 \tag{4.23}$$

In quasi-solenoidal coil, field variations along two principal directions are of interest - radial and along the z-axis. The d is taken to be radius length R for a radial axis inhomogeneity and half of the coil's height L for the z-axis inhomogeneity. The field distribution along the z- and radial axis is depicted in figures 4.16 and 4.17, and calculated homogeneity factors are in table 4.1. The decisive parameter of the coil homogeneity turned out the be the ratio of coil's radius R and coil's height L. Clearly a bigger ratio R/L yields a better homogeneity at the cost of the weaker magnetic field induced at the coil's center. Generally, homogeneity tends to be higher along the z- direction than radial, as the contribution from individual wires increases further from center in radial direction. In table 4.1 are presented calculated homogeneity factors for quasi solenoid and real solenoid. The difference of the homogeneity in two kinds of coils is almost negligible indicating a good resemblance of LTCC coil to the real solenoid.

Table 4.1: Homogeneity factors k_0 in % for quasi-solenoid and solenoid coil of length 1.375 mm and 6 windings along the z- and radial axes for a sample of size 0.5 mm.

Radius, mm	1	2	3	4
quasi-solenoid				
radial axis	89	91	92	93
z axis	81	90	96	97
solenoid				
radial axis	90	93	94	94
z axis	80	91	96	99

Frequency domain analysis

Frequency domain analysis was executed in radio-frequency specialized package called *Electromagnetic waves, (EMW)*. The *EMW* package enables two types of studies, *eigenfrequency study*, which determines natural frequencies of the model and *frequency domain study* which actually gives a solution in the frequency domain. Eigenfrequency studies require some reasonably estimated frequency for a starting value and then search for a stable solution in its neighborhood. More details about field dynamics are obtained in frequency domain study. While in eigenfrequency study it is not necessary to specify certain excitation ports, in the frequency domain study we

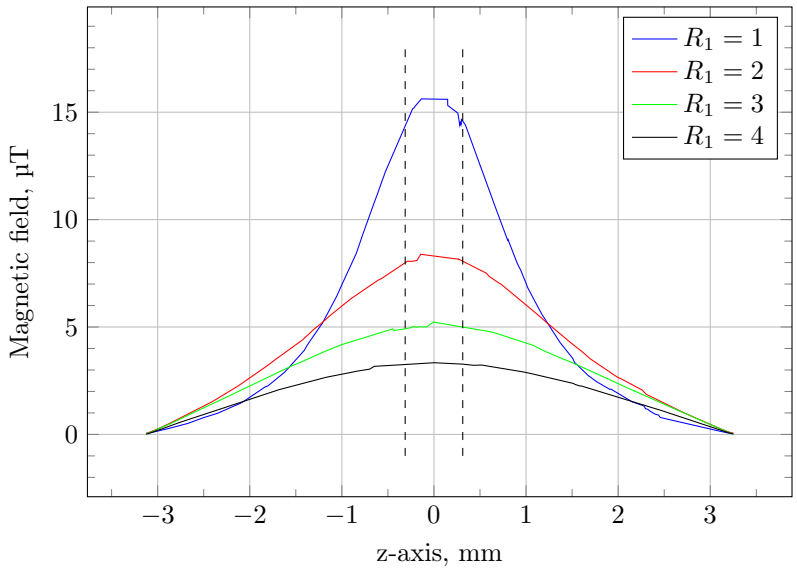

Figure 4.16: Absolute value of the magnetic field along the coil's axis of symmetry in dependence of the coil's inner radius R_1 in mm. The graph displays the decreasing field homogeneity with the smaller radius. Dashed lines represent the edges of the coil. Simulated coil had a length of 1 mm and 6 windings.

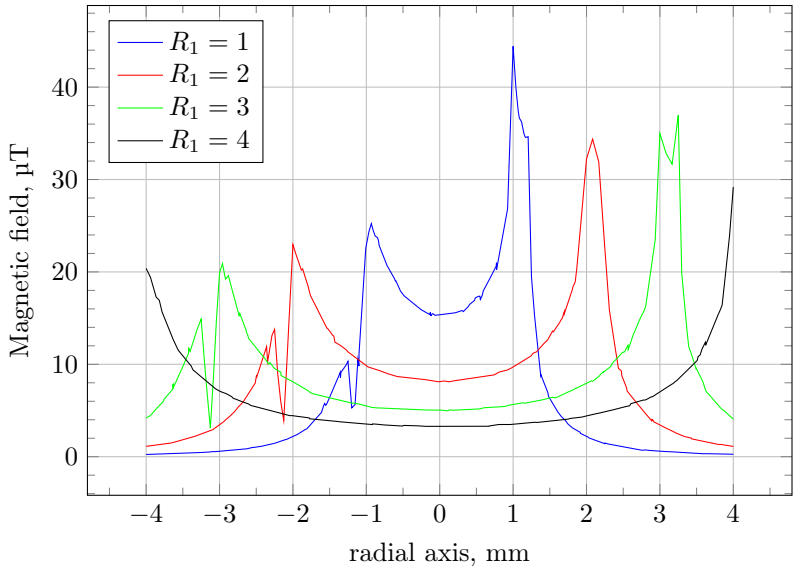

Figure 4.17: Absolute value of the magnetic field along the coil's radial axis in dependence of the coil's inner radius R_1 in mm. The graph displays the decreasing field homogeneity with the smaller radius. Radial coordinate 0 presents the center of the coil, while the coil edges are recognized as the peaks left and right from the coil. Asymmetry of the peaks left and right from the zero point as well as the gap on the left hand side come from lack of smoothness of the mesh elements. Simulated coil had a length of 1 mm and 6 windings.

need to define a surface that serves as an excitation port. This area is called *lumped port* and is a surface between two ends of the coil (Figure 4.18). It is also necessary to specify boundary condition of the model that represents infinite space that surrounds the coil. In *Comsol*, one of the options is the so called *perfectly matched layer* boundary that ensures no signal reflection at the edges of the model (Figure 4.18). The impedance of the coil is stored in the global variable called `emw.Zport_1`, and the inductance of the coil can be estimated as `imag(emw.Zport_1)/emw.omega`. The quality factor can be obtained as a ratio of imaginary and real part of impedance with `abs(imag(emw.Zport_1)/real(emw.Zport_1))`. The basic CAD sketch has been taken from the DC simulation from the previous section, along with the material-domain assignment.

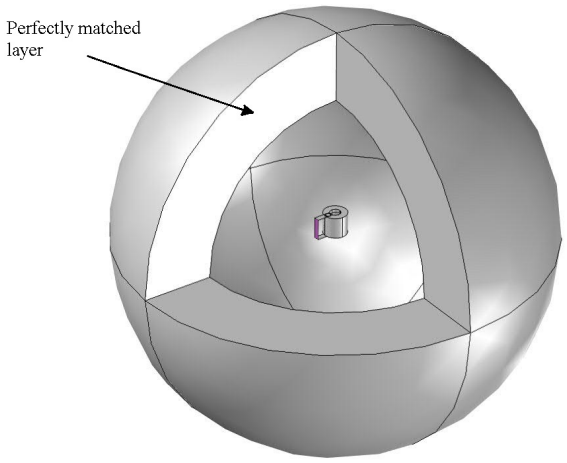

Figure 4.18: Spherical model for the frequency domain study. One eight of the sphere is cut for depiction reasons. Lumped port (purple) and perfectly matched layer are shown in perspective.

The inductance simulated this way over a wide range of frequencies for two microcoils is depicted on figures 4.19 and 4.20. There we see constant values at the lower frequency side and a resonant curve at the higher frequency end. Obtained values for two coils are presented in table 4.2. Q-factor could not be realistically modeled because the *EMW* package requires all conductive surfaces to be assigned as a perfect electric conductor. Lack of real resistance value in this simulation makes the Q-factor calculation inadequate.

Table 4.2: Simulated characteristics of the quasi-solenoidal microcoils. The coils presented in the tables have 12 layers, track width (350 µm) and the spacing between the tracks (125 µm).

Inner diameter, mm	L, nH	f_{res}, GHz
0.85	16	3.7
1.5	46	1.9

4.5.2 Eddy currents losses

One extremely useful feature of the simulation in frequency domain is the possibility of calculating the inductive losses within the coil. As shown in section 4.2.1, mathematical way of calculating eddy current losses is excessively complex and hard to

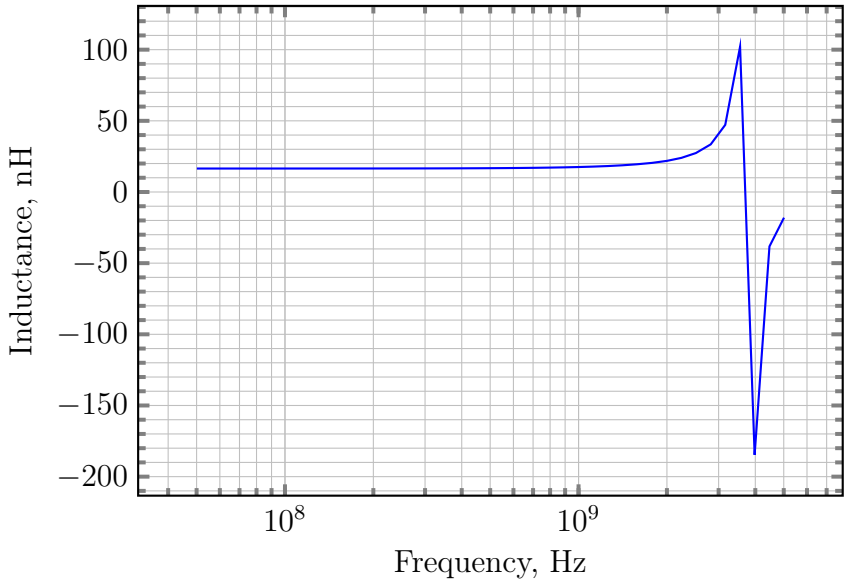

Figure 4.19: Inductance of a quasi-solenoidal coil estimated as $imag(Z_1)/\omega$ from the frequency domain study. The simulated coil had 12 layers, an inner diameter of 0.8 mm and track width 350 µm.

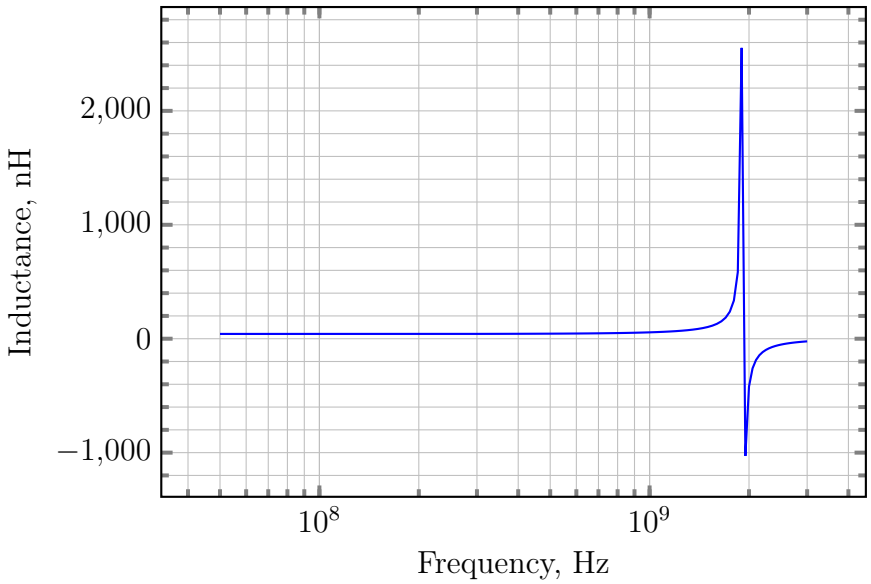

Figure 4.20: Inductance of a quasi-solenoidal coil estimated as $imag(Z_1)/\omega$ from the frequency domain study. The simulated coil had 12 layers, an inner diameter of 1.5 mm and track width 350 µm.

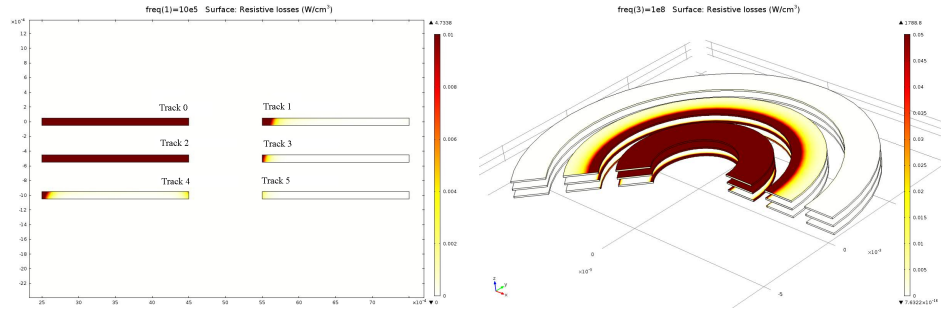

(a) (b)

Figure 4.21: Graphical representation of the eddy current losses within the solenoid coil in two (a) and three (b) dimensional image. In this simulation, only one circular track has been excited (Track 0) in the left sub-figure) and influence of its magnetic field on neighboring tracks studied.

Table 4.3: Calculated inductive losses in mW/m within the circular tracks around one excited track. This table is given in relation with the figure 4.21. The track (Track 0) on the top left has been taken for excitation with 1 A. Last column presents the sum of losses from surrounding tracks.

	Track No.						
Frequency, MHz	0	1	2	3	4	5	Total
1	61.1	0.4	26.7	0.07	0.21	0.01	27.39
10	160	1.1	89.4	0.2	0.45	0.03	91.18
100	520	3.8	295.1	0.6	1.4	0.11	301.1

estimate. FEM simulation allows to find these losses in relatively easy way. Knowing the losses from AC simulation and B_1 field can be used to estimate the SNR

For the purpose of loss calculation, a bit simplified simulation has been performed. Instead of via-connected tracks, quasi solenoid was drawn as a stack of concentric circular tracks. In simulation, only one of these tracks has been excited and influence of its inductive coupling to other tracks examined. Figure 4.21 shows two- and three-dimensional depiction of the results.

From the figure 4.21 is clear that most of the losses appear in the first neighboring track. Using integration tool of *Comsol*, total losses produced in each track can be calculated. The results for this example are given in table 4.3 in dependence on frequency. It is clear that the most of the loses (up to 98 %) is concentrated in the first top and bottom neighbor. Significantly less losses is produced in the first co-planar neighbor and negligible in all other tracks. This information can be used in estimation of losses in fabricated coils: each track in the solenoid induces losses in one track above and below itself in amount of 55 % of its own AC losses (which are in case of thick film at frequency of few tens of MHz equal to its DC losses). In co-planar track it induces only 0.6 % of its losses. For a quasi solenoid coil of N layers, with one track per layer, the total loss will be $(N + 2 \cdot 0.55(N - 1))$ times of the single track loss. Depending on the solenoid geometry, the percentage will vary and *Comsol* simulation gives a way to determine it.

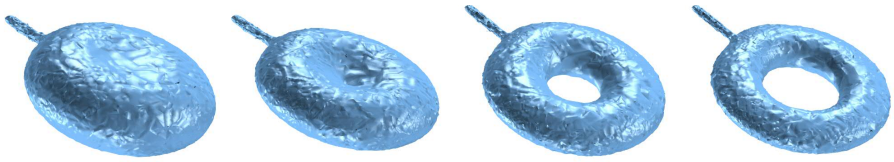

(a) (b) (c) (d)

Figure 4.22: Isosurfaces of magnetic field $|B|$ surrounding planar coil for (a) 1000 (b) 1400 (c) 1700 and (d) 2000 µT. Region of interest is where the isosurface is the most flat, i.e. plane above the spiral where the field has value of 1000 µT

4.5.3 FEM simulation of the planar coil

Massin *et al.* have delivered thorough simulations of planar microcoils of the Archimedean spiral type in [43, 44, 45] and [46]. The conclusion was that, in accord with the mathematical analysis, the signal-to-noise ratio per unit volume changes with the number of windings and has a local maximum. A homogeneity study showed that the magnetic field is the most homogeneous at the distance above the spiral plane which is equal to the spiral initial radius.

Similar to the simulation of the quasi-solenoidal coil from the previous section, the simulation of the planar coil has been developed in *Comsol* and consisted of 4 steps: 3D drawing, material assignment, physics specification (excitation port and Maxwell equations), meshing and finally numerical solver. In this case 3D sketch has not been directly drawn in *Comsol* , but imported from standard CAD software (*AutoCAD*). Again, the solution is laid out in DC conditions as well as in frequency domain. Different parameters of the spiral coil have been varied to find optimum performance of the coil for the NMR measurement purposes.

DC simulation and homogeneity study

The imported spiral layout has been assigned terminal and ground ports at its ends. The field distribution is visualized on figures 4.22 and 4.23, where it is clearly visible how homogeneity decreases close to the coil tracks. The highest homogeneity region really is in a plane at a distance equal to the spiral initial radius above the spiral. That's where the B-value has been picked for a SNR_{puv} calculation.

As can be seen on the figure 4.25, SNR_{puv} drops down with increasing radius and spacing between the turns. The reason is that *filling factor* of the coil, that is the ratio of the track surface to the area of entire coil, significantly drops. On the other hand, by varying the track width it is possible to find a maximum SNR_{puv}. This advantage will be taken in to consideration for the coil design.

Frequency domain simulation

As in the section about quasi-solenoid coils, the frequency dependent simulation starts with specifying excitation surface called lumped port and boundary condition called perfectly matched layer that ensures no signal reflection from the edges of the model. The output results in the frequency dependent variable `emw.Zport_1` that presents impedance of the coil and the inductance is estimated as `imag(emw.Zport_1)/emw.omega`. Resonant frequency is found where imaginary part of `emw.Zport_1` equals zero. Frequency domain dependent simulation delivers the dynamic characteristics of the coil in table 4.4and helps to find the coil geometry which ensures the resonant frequency above the working NMR frequency.

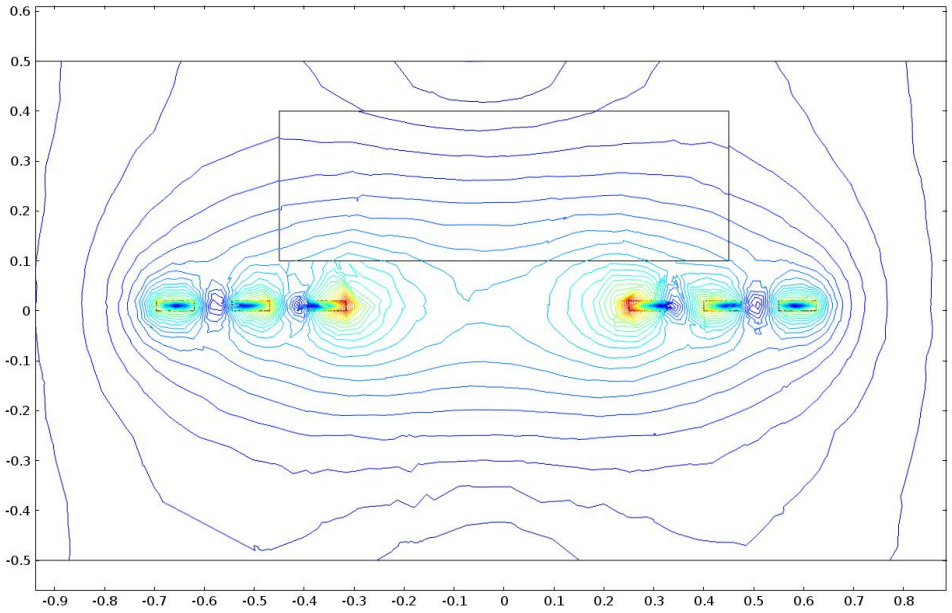

Figure 4.23: Contours on the figure depict isolines of magnetic field $|B|$ of 3-windings coil with inner diameter of 5 mm and track width of 200 µm. It is clearly visible how the field exhibits maximum planar homogeneity at the distance above the coil that is equal to the radius.

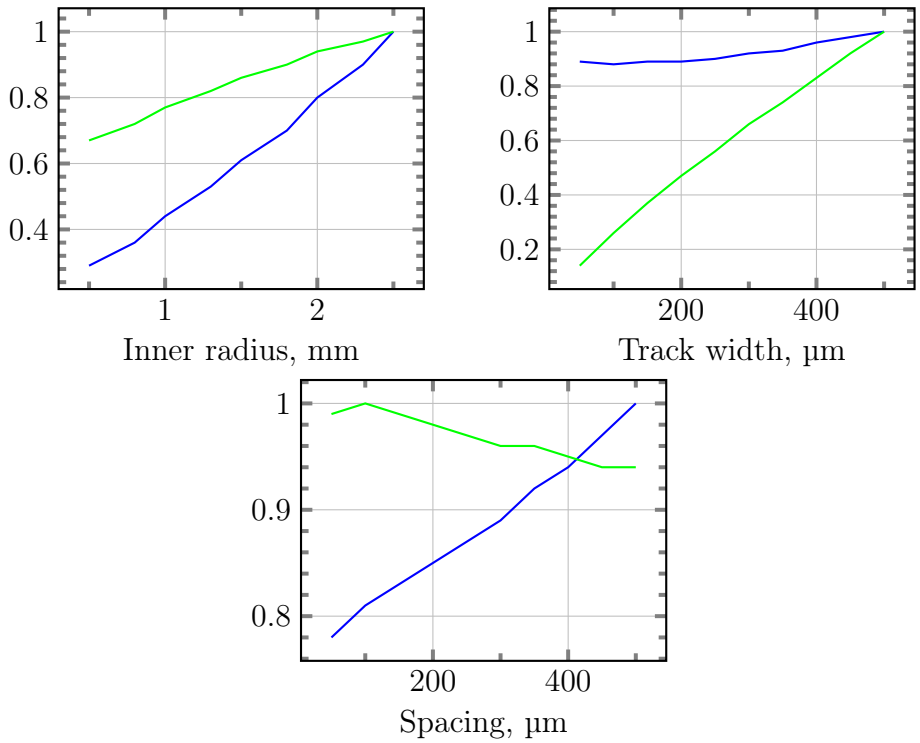

Figure 4.24: Normalized values of L (blue line) and Q (green line) of the planar spiral against different parameters, as obtained by the simulation. Inductance was normalized by the factor of 87 nH in the top left graph and 37 nH in other two graphs. The constant values were inner radius 0.8 mm, track width and spacing 0.1 mm and 3 windings.

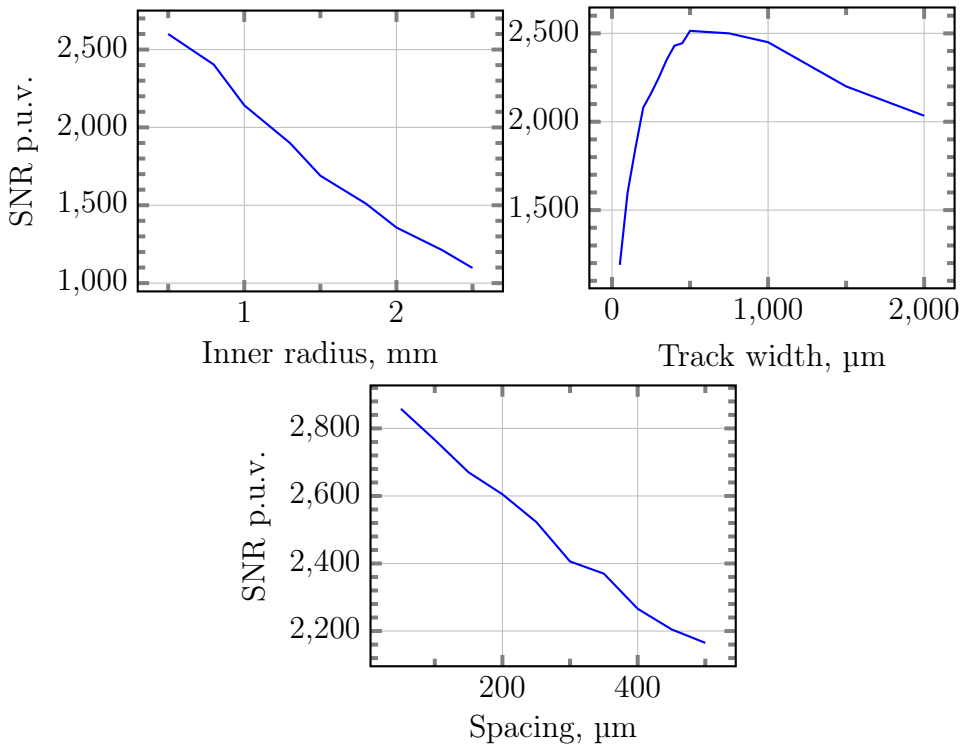

Figure 4.25: Estimated SNR p.u.v. of the planar spiral coil for different geometry parameters. The constant values were inner radius 0.8 mm, track width and spacing 0.1 mm and 3 windings.

4.5.4 FEM simulation of the twin horseshoe resonator

The twin horseshoe resonators have been simulated in a similar way as the other coils. The 3D model contains an alumina ring with two silver horseshoe shaped arcs, as shown in the figure 4.9. The air region and perfectly matched layers are presented as the spheres significantly larger than the alumina ring. Gap area is chosen as lumped port for excitation of the silver track on one side of the ring. Finally, the inductance calculated as `imag(emw.Zport_1)/emw.omega` is presented in figure 4.26. There it is shown how variations in resonator's thickness t change resonant frequency. The inductance and self resonance are compared to the values from mathematical analysis in the table 4.5. It can be shown that the values of L and f_{res} correspond well to the analytical model explained in 4.21. The most decisive parameter for resonant frequency is capacitance of the resonator since it drastically changes with the track width and thickness, both of which are most influential for the capacitive contribution. Neither of parameters seems to impact the inductance of the resonator in radical measure. The inductance changes considerably only for tracks thinner than 1.5 mm.

Resonant frequency of the twin horseshoe resonator can be tuned either by changing some geometry parameters (in this case thickness is the most influential) or by adding an external capacitor. Instead of component available on the market, the external capacitor can be created by simple metal plate placed in the vicinity of the resonator. By varying the distance of the plate from the horseshoe ring, the resonant frequency can be finely tuned. An example of the resonance shift by the plate movement is showed in the figure 4.27.

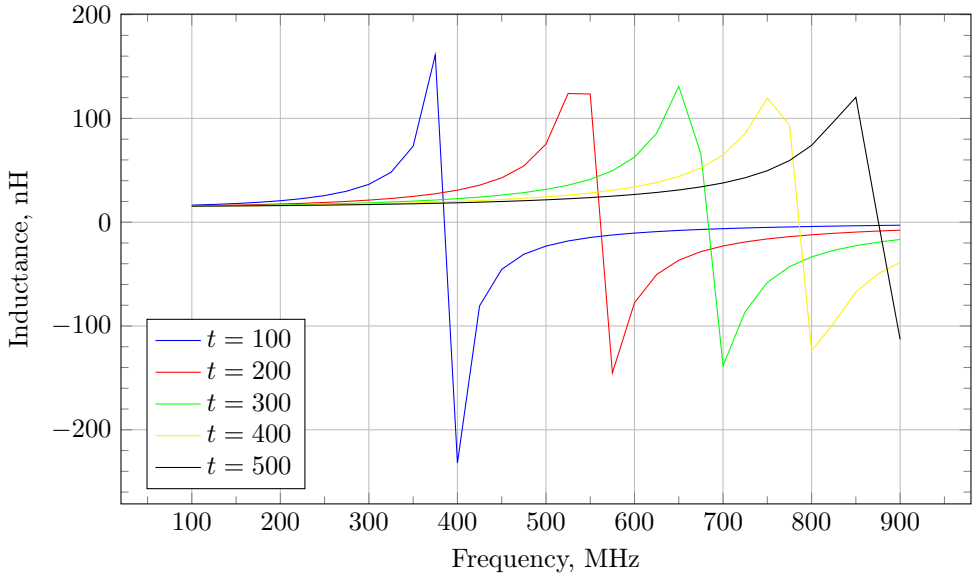

Figure 4.26: Inductance of the twin horseshoe resonator in dependence on its thickness t, µm. Other parameters are: inner diameter 9 mm, gap width 4.5 mm and track width 2.5 mm.

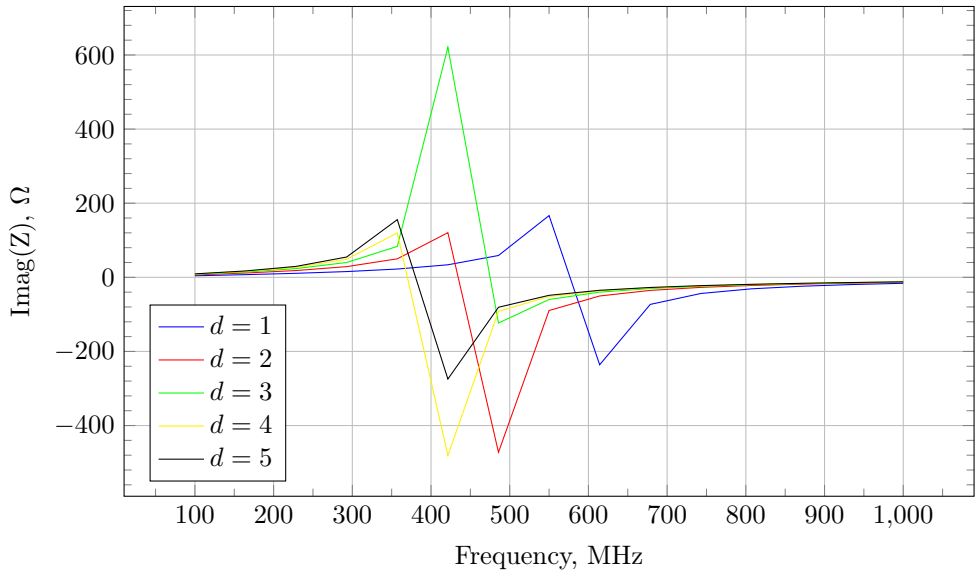

Figure 4.27: Imaginary part of the twin horseshoe resonator impedance in dependence on distance d from the metallic plate in mm. Other parameters are: inner diameter 9 mm, gap width 4.5 mm, thickness 0.5 mm and track width 2.5 mm.

Table 4.4: Electrical characteristics of the simulated planar coils. The coils presented in the tables have the common parameters specified above each table.

Inner diameter (5 mm), track width (300 µm) and spacing between the turns (250 µm)

No. of turns	L, nH	Q-factor	f_{res}, MHz
4	157.5	45	518
6	355	59	319

Number of turns (3), track width (100 µm), spacing between the turns (100 µm)

Inner diameter, µm	L, nH	Q-factor	f_{res}, MHz
800	8.83	17	2290
1600	28.4	21	1180

Table 4.5: Inductance and self-resonance of the twin horseshoe resonator in dependence on gap length and track width. Inner radius of the coil is 4.5 mm and initial track width, thickness and gap length are 2.5 mm,300 µm and 4.5 mm, respectively.

	Simulation		Theory
Gap length, mm	L, nH	f_{res}, MHz	f_{res}, MHz
1	15.5	812	823
2	15.5	835	836
3	15.5	840	849
4	15.5	860	863
5	15.5	875	877
Track width,mm			
0.5	22	-	992
1	19	-	962
1.5	17	-	934
2	16	-	908
2.5	15	875	884
3	15	780	861
Thickness, µm			
100	16	390	
200	15.8	560	
300	15.6	695	
400	15.5	790	
500	15.4	890	

Chapter 5

Coil Fabrication and Characterization

5.1 Coil fabrication

Multiple sets of coils have been fabricated in LTCC technology in order to examine their suitability in NMR spectrometry. Led by the analysis presented in previous chapters different geometrical shapes have been produced that can be categorized in two main groups, three dimensional (solenoid) and two dimensional (planar) coils. Three dimensional coils have in general quasi-solenoidal shape and differ in number of layers as well as in number of turns per layer (Archimedean spiral coil type). Two dimensional coils have a spiral shape with varying number of turns. Another category of two dimensional structures for NMR measurements are twin horseshoe resonators.

To test the dependence of coils' properties on different geometry parameters, the sets have been produced with varying geometries like track width, number of layer, inner radius, etc. The fabricated samples are listed in Table 5.1. An additional set of microcoils has been produced after the calculation of the optimal structure shapes for nano-liter volume NMR samples.

5.1.1 General fabrication details

This section provides details of the coil fabrication process that was performed in the Laboratory for Integrated Circuits and Technologies and it includes all fabrication steps described in the chapter 3. LTCC tapes CT707, CT708, CT802 and CeraTape GC were used for different coil type fabrications. These materials were chosen on the basis of their low dielectric loss and lower permittivity what reduces parasitic capacitance.

If not noted otherwise, the following are the general parameters of the coil fabrication process. One sample structure was predestined to accommodate multiple coils of the same geometry. Tapes were laser cut with perforations to enable further mechanical processing of each tape. Laser cut vias, 200 µm in diameter were filled with a conductive silver-based paste Heraeus TC7304. High viscosity of the paste and small size of the vias prevent from paste leakage, which is further hindered by drying the tapes in the oven at 75 °C. The next step in fabrication was line printing, where conductive tracks were screen printed on every tape. The screen stencil was made with the standard photolithography technique. Screen printing was performed with Heraeus TC7306 silver-based paste under pressure of 2.7 bars. After printing, tapes were dried once again at the temperature of 75 °C.

Table 5.1: Geometry data of the produced samples. Parameters with * are relevant for microcoils only.

Three dimensional coils	
Number of layers	10, 12*, 20, 40, 60
Number of turns per layer	0.5, 1, 2, 4, 6
Inner radius, mm	0.8*, 1.5*, 5, 10
Track width, mm	0.3*, 0.5, 1, 2
Interturn spacing, mm	0.5
Spacing between layers, μm	50, 125, 500
Two dimensional coils	
Number of turns per layer	3, 4, 6
Inner radius, mm	0.4*, 1.6*, 5
Track width, mm	0.1*, 0.5
Interturn spacing, mm	0.1*, 0.5
Twin horseshoe resonators	
Inner radius, mm	5
Gap width, mm	1, 2, 5
Spacing between layers, μm	50, 100, 250, 375, 500

The tape samples (each of which forming one layer of the final coil specimen) were stacked above each other with the help of an aluminum mold. A single tape of a PET film is added between the LTCC stack and press mold to prevent the adhesion of raw tape to the aluminum. Once stacked and preheated to 80 °C, the structure was exposed to an uniaxial pressure of 80 to 160 bars depending on the structure's number of layers for 3.5 to 5 minutes. During this process, called lamination, a single substrate is created from stacked tape layers.

Co-firing of the laminated structure is the most sensitive process in the LTCC production cycle and it was done, depending on the sample, either in a chamber or in a belt furnace. During the co-firing, ceramic and conductor particles are sintered together by exposition to temperatures of up to 900°. The most important technical points in this process are controlling the firing shrinkage of the whole substrate, controlling firing behavior of different materials within the sample to prevent defects, and achieving both, antioxidation of the conductor material (silver) and melting of the binder material (glass granules). Because of the variety in sizes of samples one must adjust the firing parameters for each sample to satisfy these requirements. The optimal co-firing temperature profile to achieve these requirements depends on the sample, but co-firing temperature is always under 900 °C. Samples of CT708 and CT707 tapes consisting of less than 20 layers were fired with the same profile as given in the table 3.3. Prior to firing the samples are sandwiched between two CeramTape A tapes that serve as a mechanical constraint for the deformations during the firing process.

5.1.2 3D coils fabrication details

One sample structure, consisting of 10 to 60 LTCC tapes was predestined to accommodate 2 coils of the same geometrical properties. The structures were made of CT708 and CT802 tapes from Heraeus GmbH. Laser cutting, via filling and line printing were made according to the general procedure. All printed tapes were stacked together so that semicircle track on each layer is mirrored. Overlapping ends where then via-connected with the track on the layer below and above, respectively. Lamination, however, had to be adapted to the different sizes of the samples.

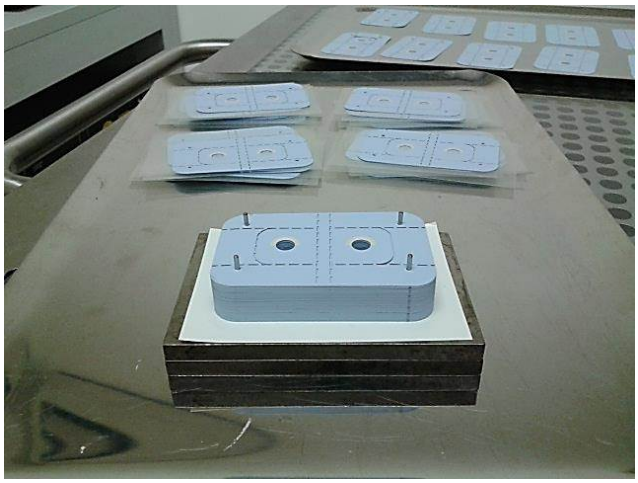

Figure 5.1: Stack of LTCC tapes prior to lamination. Unstacked layers are in the background.

A bigger number of layers required a significantly lower pressure (70 bar), otherwise significant deformation in x-y direction occurs (Figure 5.1). For samples of 40 and 60 layers it was shown that optimum lamination is executed in few iterations. Firstly, sets of 10 LTCC tapes should be heated to 70 °C then laminated for 3.5 minutes under 115 bar pressure. Afterwards, 4 or 6 of these sets were to be laminated together for 5 to 6 minutes under 70 bar.

Due to the larger size, the standard temperature profile (Figure 3.2) is not applicable. If the temperature increases too rapidly, as is the case in the standard profile, its distribution within the sample will be non-uniform. This peculiarity inevitably causes uneven firing and leads to deformations. The coils were finally fired in the box furnace with the profile shown in Figure 5.2. At temperature rate of 1.1 °C/min was confirmed to be adequate to reach a uniform temperature distribution the within whole sample.

5.1.3 3D Microcoils fabrication details

One sample structure, consisting of twelve LTCC tapes was predestined to accommodate 32 microcoils in two different dimensions: 16 microcoils of diameter 800 µm and 16 microcoils of diameter 1500 µm (Figure 5.3).

A lead free tape CT708 from Heraeus GmbH, Germany was used. Rings which form the body of the coils were laser cut with perforations to enable detachment of the coil from the substrate. The envisaged width of the substrate ring was 350 µm. Every ring had a 100 µm diameter hole which serves as a via after filling it with a silver-based paste. For adequate printing, 50 µm thick Murakami stencil was attached on the steel screen with the mesh of 450 dpi. Lamination and firing were made in accordance to standard procedure. These samples turned out to be very lamination sensitive. Due to the high height-to-width ratio of the coil, the lamination process caused significant deformations, as depicted in figure 5.4. The substrate was bended and paste squeezed between the layers.

The improvement would include mechanical support during the lamination which will not affect the component during the firing and will be easy to remove afterwards. The best attempt was to pour liquid PMMA inside the cylinder of the microcoil and the perforations around the ring. Liquid PMMA provides hydrostatic pressure that minimizes deformation forces on the walls of the coil and keeps the structure intact during the lamination process. PMMA is a good choice because it does not

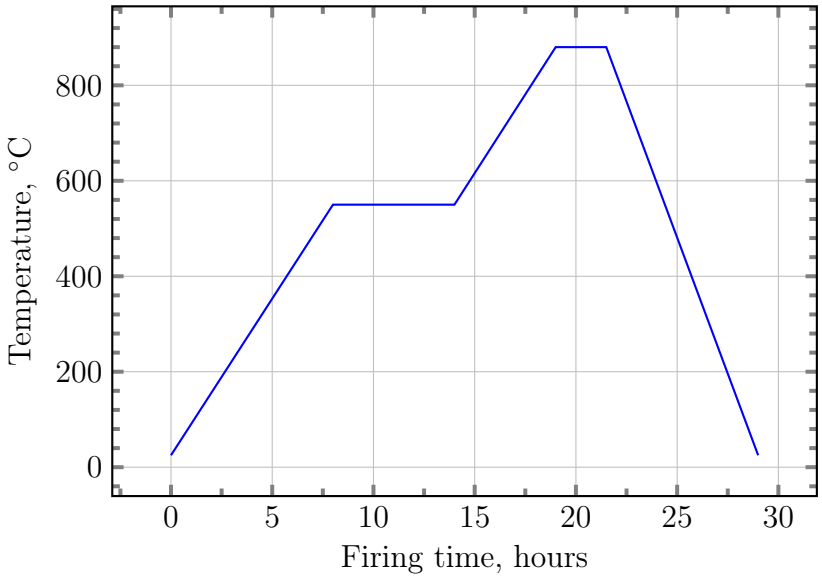

Figure 5.2: Temperature profile for the 40 - 60 layers big samples. The peak temperature is 880 °C, and the heating rate is 1.1 °C/min

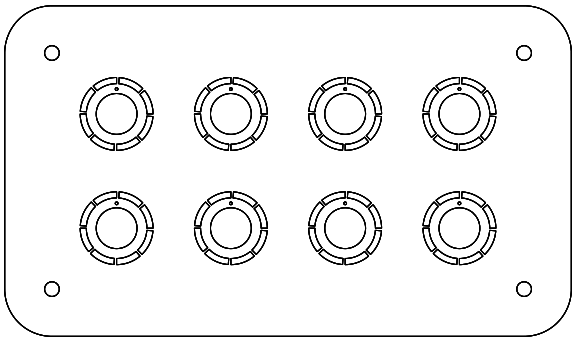

Figure 5.3: Layout of the substrate for 8 microcoils. The image is enlarged for presentation reason.

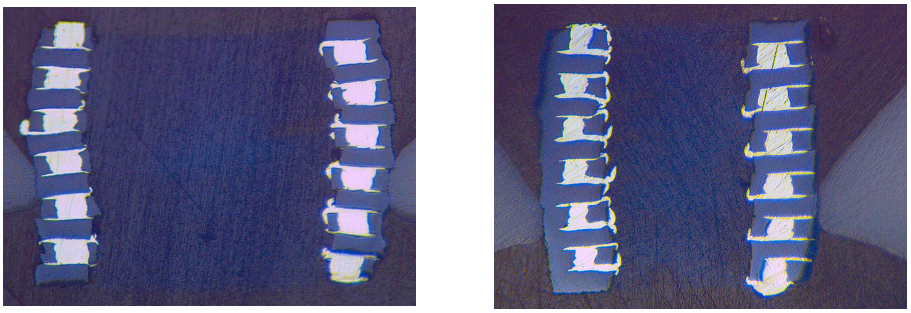

(a) (b)

Figure 5.4: Deformation and paste leakage in the (a) 1.5 mm diameter and (b) 0.8 mm diameter coils.

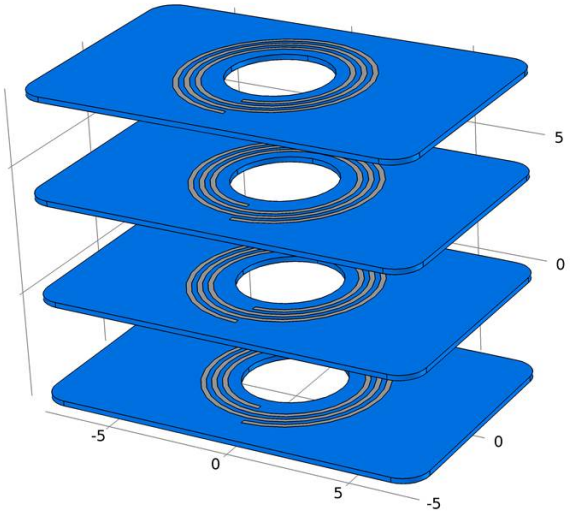

Figure 5.5: Stack of the spiral track layers of LTCC in 3D coil.

react nor damage the LTCC tape and is burned out completely in the firing stage. Additionally, the lamination has been done under significantly reduced pressure, that is, 80 bar. Cross sectional images are displayed in figures 5.11 - 5.13 in the section "Post-firing analysis". However, leaked paste still remained on the inner side of the cylinder wall. It was removed after firing with the help of diamond tipped drill. The diamond tip could easily peel off the leaked paste of the ceramics. This step is very delicate and requires exquisite drill handling skill in order to avoid any permanent damage of the coil.

5.1.4 Spiral coils fabrication details

Spiral coils come in a 3D and a 2D modification. In the former kind, printed tapes were stacked together so that the spiral on one layer faces the spiral on the neighboring layer oppositely. Ends of the spirals were connected with vias which in every layer ended up on opposite sides of the ring (Figure 5.5). Planar microcoils have a spiral layout and ground-signal-ground SMA connection pads on the topmost layer. On the second layer, return path is printed to provide a signal path from center of spiral to ground pads. Two layers are connected with 100 µm diameter vias placed in the inner end of the spiral and in the ground pads (5.6). Proper positioning of the tapes is done with the help of four additional reference holes which were fixed to four reference pins fastened on a metal mount. Once stacked and preheated to 80 ° °C the structure was exposed to a uniaxial pressure of 120 bar for 3.5 minutes. Firing was performed in the belt furnace with the standard profile Heraeus tape profile (3.3).

The creen printing stencil should be made with special care for this kind of coils. Murakami film, used for stencil fabrication comes in two thicknesses, 30 and 50 µm. If the spacing between the spiral tracks is about 100 to 150 µm, then the film's structural stability is insufficient for further processing due to low width-to-height ratio. For that reason, 30 µm film was always used and stencil deteriorations were prevented.

Another type of spiral coil that was produced is a four coil system for circular polarized field generation. This system consists of four layers: a top layer where the spiral coils are printed, a second layer where the track connecting one pair of coils is printed and a third layer where a track that connects the other coil pair is printed, perpendicularly to the track on second layer (Figure 5.7). The additional

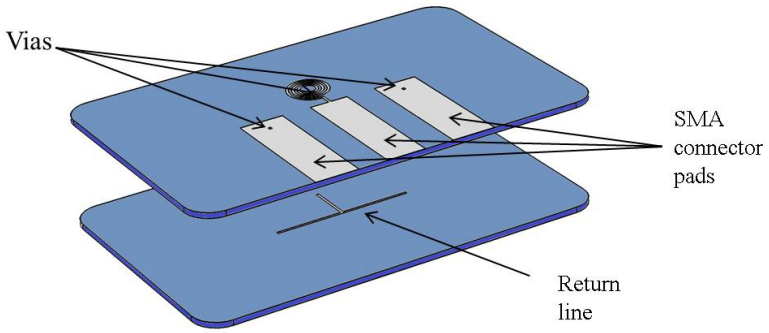

Figure 5.6: Planar spiral microcoil on a two layered LTCC substrate.

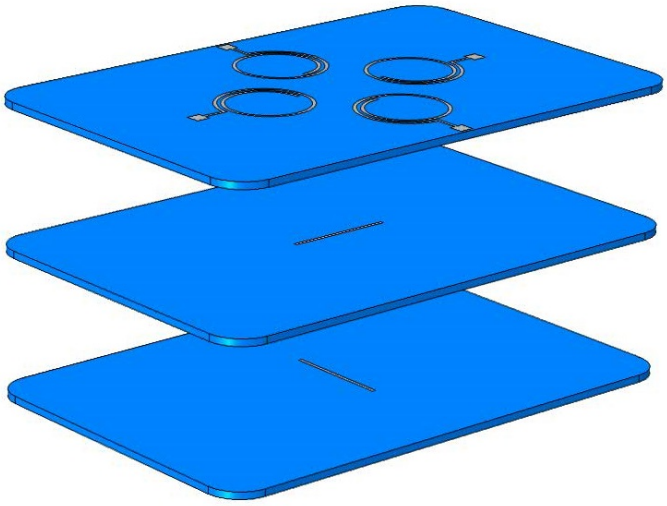

Figure 5.7: Spiral coil set for circular field generation on a three layered LTCC substrate.

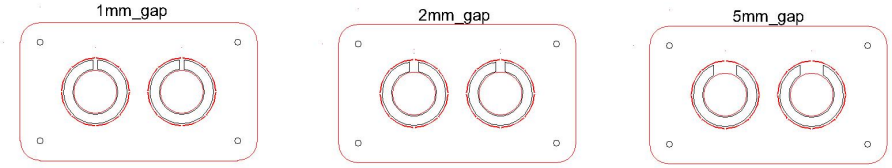

Figure 5.8: Twin-horseshoe resonator top layout.

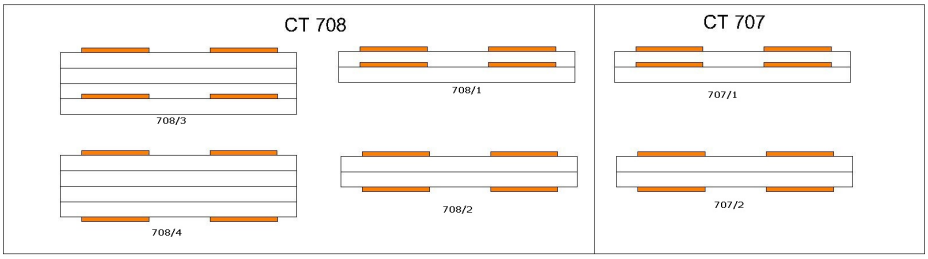

Figure 5.9: Twin-horseshoe resonator stack profile. Various distances between tracks were achieved by varying the number of layers and tape thickness

fourth layer at the bottom serves for mechanical support only. The coil pairs and corresponding tracks were connected with TC7304 vias.

5.1.5 Twin horseshoe resonators fabrication details

Three kinds of resonators were designed with a diameter of 10 mm, and line thickness of 2 mm. They differ in the gap width: 1, 2 and 5 mm as indicated in figure 5.8. For this purpose, again, the tapes CT707 and CT708 were used. For printing conductor tracks, silver paste TC7306 and a 325 dpi screen with a 50 µm thin Murakami stencil were used.

Samples with different distance between two tracks (from 50 to 500 µm) were fabricated by varying number of layers and tape thickness, as demonstrated in figure 5.9. To reach 50 and 100 µm distance, CT707 was used. Samples were laminated under 107 bar for 3 minutes and fired with the standard belt furnace Heraeus profile (Table 3.3).

5.1.6 Post-firing analysis

After sintering, samples were optically inspected. The overall thickness of the 3D coils varies from 1.5 mm for the 10 layers coil to 9 mm for the 60 layers coil. The thickness increases linearly with the number of layers, as shown in Table 5.2, which indicates that the shrinkage in z-axis is independent on the number of layers. Likewise, the shrinkage in x- and y-axes was constant across all sample sizes. The measured values differ slightly from those specified in the datasheet (Table 3.1), probably due to the different fabrication process. Usually, gentle breaking along the perforations suffices to disjoint the coil from the substrate, but in case of the thick 60-layers coil (Figure 5.15), it was necessary to use a diamond saw to cut off the sintered ceramic.

Table 5.2: Shrinkage results of the produced samples in dependence on stack size.

No. of layers	Thickness, mm	Shrinkage in z-axis	Shrinkage in x-y plane
10	1.4	30 %	17 %
20	2.8	30 %	17 %
40	5.7	28 %	17 %
60	8.7	27 %	17 %

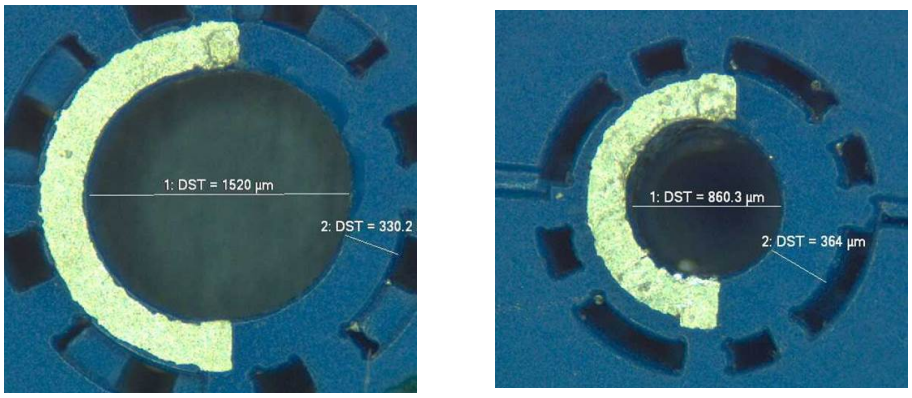

(a) (b)

Figure 5.10: Top view on the sintered (a) 1.5 mm diameter and (b) 0.8 mm diameter coils. Microscopically measured track widths are displayed on the photo.

One of the coils was immersed in an epoxy mixture and cut for a cross-section study. The main objective of this action is to investigate the via quality. After milling and fine grinding, vias were microscopically inspected and are shown in Figures 5.11 and 5.12. Complete silver reflection is a sign of the good via filling process, but the cone-like via cross-section is a consequence of a parabolically sharpened laser beam.

The quality of the silver tracks that were printed on microcoil samples (Figure 5.14) is arguable. Circular tracks of only 100 µm width or less may not be the most suitable for screen printing technique. The screen raster of 425 dpi gives only $425/254 \approx 1.6$ dots per 100 µm, which could be responsible for the poor line resolution. For this technology wider, straight and rectangular lines are more suited.

Nonetheless, the overall production quality was satisfactory after final procedure parameters were set. No deformations or sample cracking were observed. Although individual intervention for each sample group was necessary, the general fabrication guidelines apply well.

5.2 Electrical characterization of the coils

5.2.1 Wired coil characterization model

All of the produced coils were characterized with the help of the vector network analyzer (VNA) HP8753 by Hewlett-Paclard, Ltd. A single port measurement was performed in order to obtain the reflection coefficient (S_{11} parameter). An open-short-match calibration of the analyzer is obligatory prior to the measurements. Measured S-parameters were converted to the impedance (Z) parameters, according to the relation:

$$Z = 50 \cdot \frac{1 + S_{11}}{1 - S_{11}} \tag{5.1}$$

At the frequencies of few MHz such coils can be modeled as a series circuit of an inductor and a resistor whose impedance is $Z = R_s + j\omega L_s$. The inductance is in

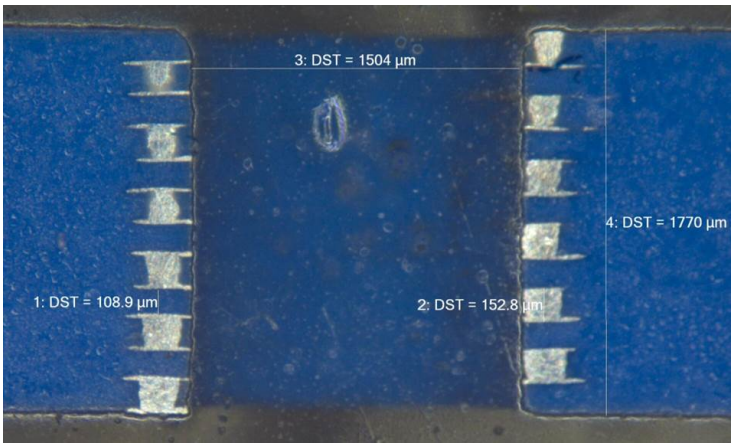

Figure 5.11: Cross sectional view on a sintered microcoil. Microscopically measured distances are displayed on the photo.

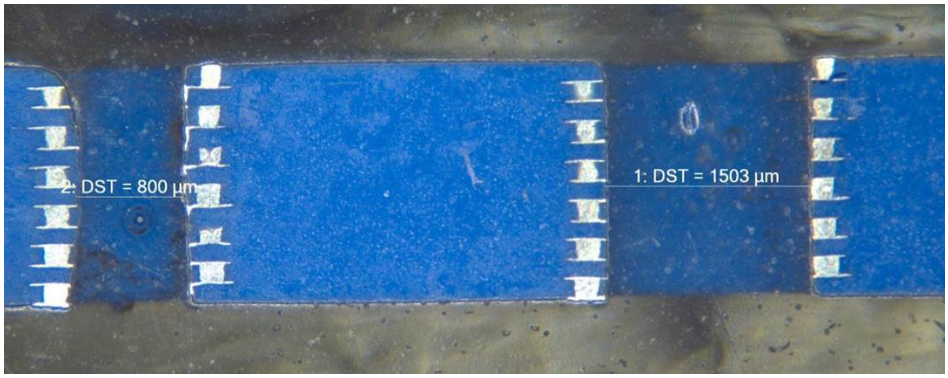

Figure 5.12: Cross sectional view of two sintered microcoils within the same substrate. Microscopically measured dimensions are displayed on the photo.

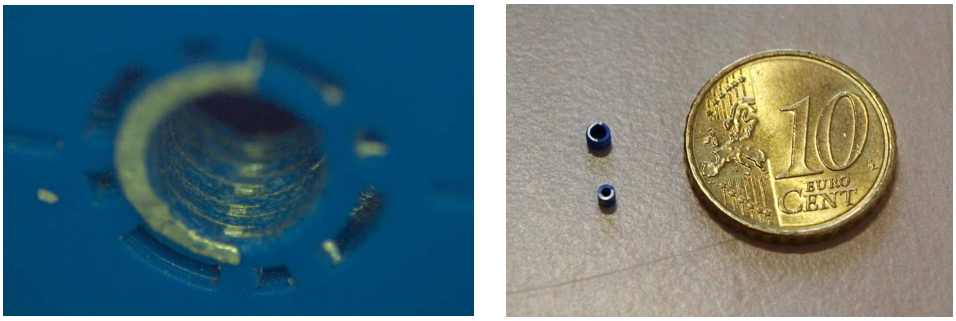

(a) (b)

Figure 5.13: (a)Perspective view of a microcoil after drill cleaning of the leaked paste. (b) Microcoils placed next to a coin for the size comparison.

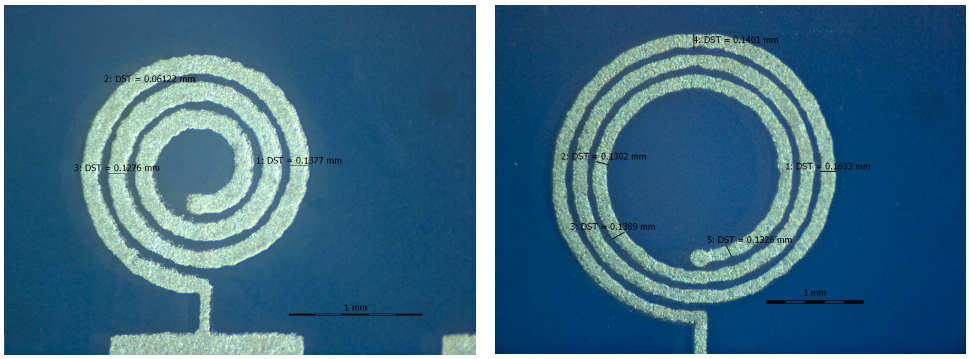

(a) (b)

Figure 5.14: Top view of the sintered (a) 0.5 mm inner diameter and (b) 1.6 mm inner diameter planar spiral coils. Microscopically measured track widths are displayed on the photo.

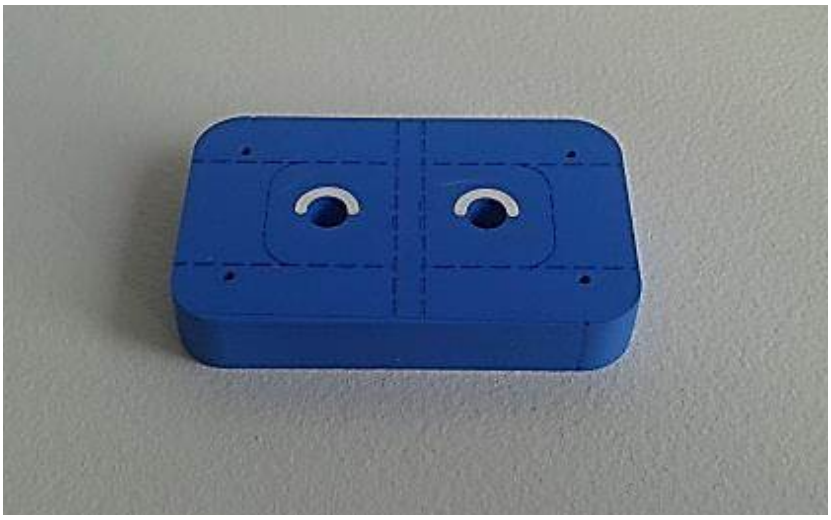

Figure 5.15: A set of two 3D coils of the same type on the same substrate after firing.

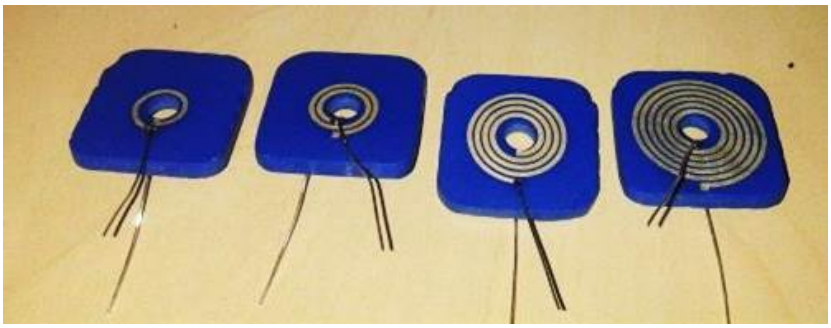

Figure 5.16: A set of spiral 3D coils with the varying number of windings.

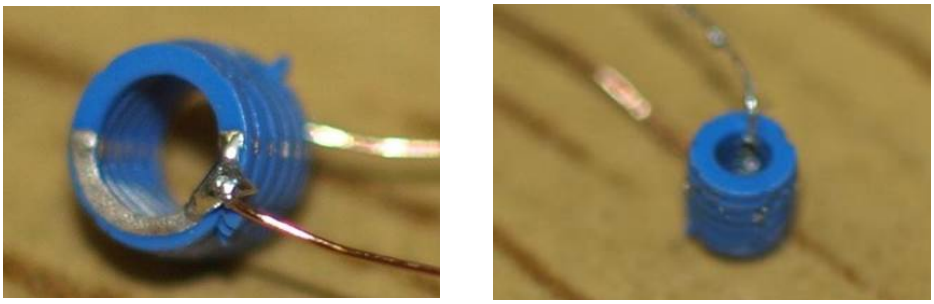

(a) (b)

Figure 5.17: (a) Bigger and (b) smaller microcoil with a soldered 200 µm copper wire for electrical characterization.

this approximation the ratio of imaginary part of the impedance and the frequency in rad/s (Figure 5.18). In this approximation inductance should be constant, but as the frequency gets closer to the coil's self-resonance, the capacitive contribution to the imaginary part becomes more apparent and this simplified model becomes invalid. That's the reason for the curvature at the right hand end in the given figure. The quality factor, Q, is given by the absolute ratio of imaginary and real part of the impedance in figure 5.19. Ideally Q should rise with the frequency according to Formula 2.17, but as the frequency gets closer to self-resonance the model breaks down and hence quality factor starts to drop. The self resonant frequency is estimated as the frequency where imaginary part of Z and, correspondingly, L is zero.

5.2.2 3D coil characterization results

After fabrication, coils were connected with 100 to 200 µm silver plated copper wire and attached to a small (1 cm^2) printed circuit board with SMA connectors for impedance characterization (Figure 5.17). 50-Ω BNC-SMA coax cable joined the vector network analyzer to the printed circuit board. An example of inductance and Q-factor measurement is shown in the figures 5.18 and 5.19. Inductance values evaluated at the low frequencies as well as the highest occurring Q, and their simulation counterparts are listed in the Table 5.3. The dependence of the coil inductance on number of layers and number of turns per layer is depicted in figure 5.20. Comparison of geometry dependence of measured inductance values to the simulated ones is presented in table 5.3 and figure 5.21. Close agreement of two values verifies the simulation procedure from section 4.5.3. For some of the coil, mostly those with more windings per layer the simulation model would break due to the complex geometry.

Theoretically, the inductance of the solenoid coil is proportional to the squared number of windings, cross section area and inversely proportional to the coil's length. The graphs in figure 5.20 show the measurement results for the 3D coils to be in the agreement with this expectation. In the section 4.1.1 it was shown that increasing the length of the solenoid with the same number of windings per length makes inductance rise linearly. In the figure 5.20 the inductance does rise linearly with the number of layers and exponentially with the number of windings per layer. In contrast, the Q factor significantly changes only for different number of windings per layer. The reason for that is explained in chapter 4.5.3: eddy current losses are most notable in windings above and below an excited winding. For spiral coils with multiple windings per layer this contribution gets more dominant and the Q-factor decreases more notably if number of windings per layer is increased than only number of layers.

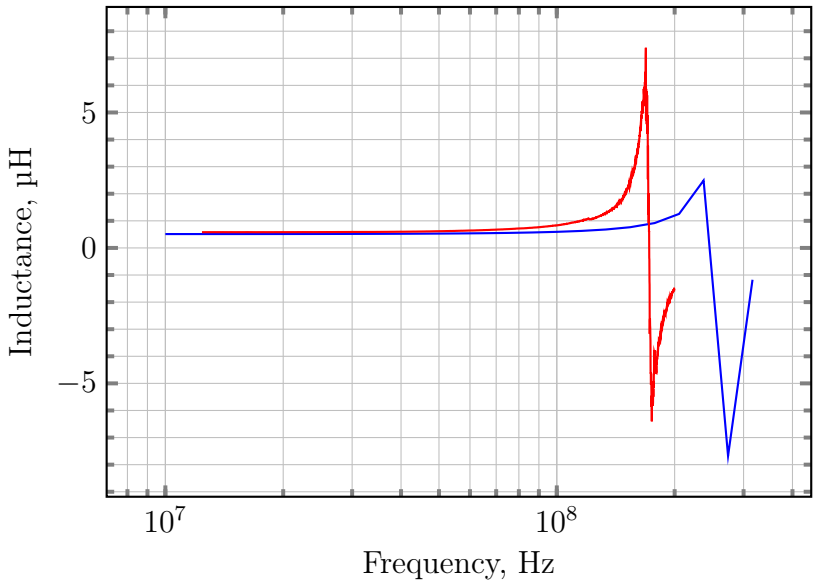

(a)

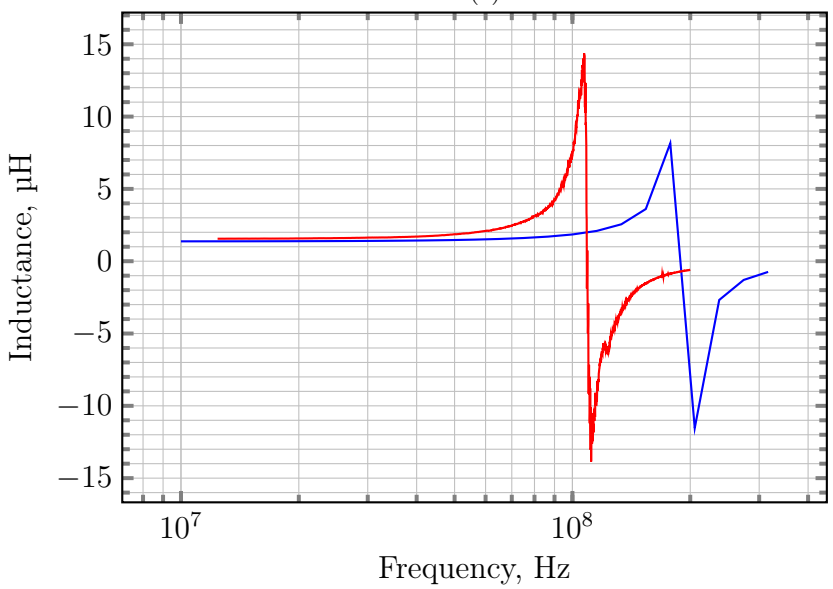

(b)

Figure 5.18: Inductance of quasi-solenoidal coils from measurement (red line) and simulation (blue line). The coils had 20 (a) and 40 (b) layers, an inner diameter of 5 mm and track width 350 µm. The graphs show good agreement between simulation and measurement at the low frequencies but certain discrepancies close to the resonant frequency.

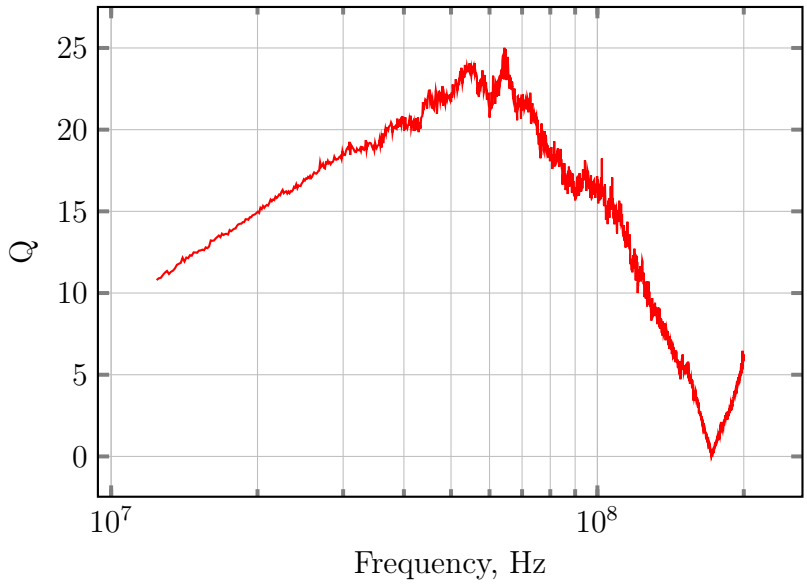

Figure 5.19: An example of quality factor (Q) measurement of the quasi-solenoidal coil. The coil had 10 layers, an inner diameter of 5 mm and track width 350 µm. It is clear that Q-factor has maximum value at certain frequency below the resonance. This is attributed to increasing resistive losses that became more apparent as the frequency gets close to self-resonant.

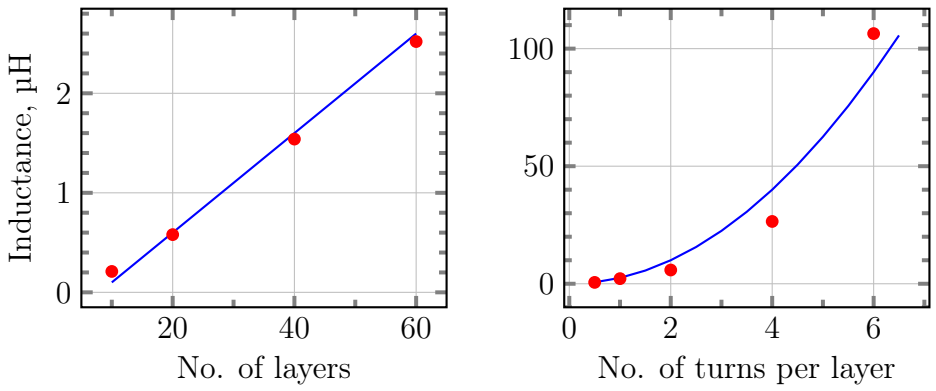

(a) (b)

Figure 5.20: Inductance vs (a) number of layers and (b) number of turns per layer with the theoretical predictions (blue line). The inductance rises linearly with the number of layers and exponentially with the number of windings per layer.

Table 5.3: Electrical characteristics of the produced coils in comparison to the simulated ones. The coils presented in the tables have the common parameters specified above each table.

	Measurements			Simulations		
0.5 turns per layer, inner diameter (5 mm), track width (300 µm) and spacing between the tracks (125 µm)						
No. of layers	L, µH	Q	f_{res}, MHz	L, µH	Q	f_{res}, MHz
10	0.21	38	260	0.18	40	350
20	0.58	33	172	0.51	31	240
40	1.54	31	109	1.47	51	180
60	2.52	31	86	2.41	55	166
20 layers, 0.5 turns per layer, inner diameter (5 mm) and spacing between the tracks (125 µm)						
Track width, mm	L, µH	Q	f_{res}, MHz	L, µH	Q	f_{res}, MHz
0.1	0.5	33	213	0.54	26	280
0.3	0.58	33	172	0.51	31	240
3	0.49	37	115	0.61	118	153
20 layers, 0.5 turns per layer, track width (300 µm) and spacing between the tracks (125 µm)						
Inner diameter, mm	L, µH	Q	f_{res}, MHz	L, µH	Q	f_{res}, MHz
5	0.58	33	172	0.51	31	240
10	1.3	39	89	1.42	51	130
20 layers, 0.5 turns per layer, inner diameter (5 mm) and track width (300 µm)						
Spacing between the tracks, µm	L, µH	Q	f_{res}, MHz	L, µH	Q	f_{res}, MHz
50	0.3	21	193	0.77	29	205
125	0.58	33	172	0.51	31	240
20 layers, inner diameter (5 mm), track width (300 µm) and spacing between the tracks (125 µm)						
No. of turns per layer	L, µH	Q	f_{res}, MHz	L, µH	Q	f_{res}, MHz
0.5	0.58	33	172	0.51	31	240
1	2.18	21	92.4	-	-	-
2	5.85	16	32.4	-	-	-
4	26.5	3	15.3	-	-	-
6	100.4	5	5.45	-	-	-
spacing between the tracks: 500 µm						
4	0.2	38	360	-	-	-
6	0.46	43	231	-	-	-

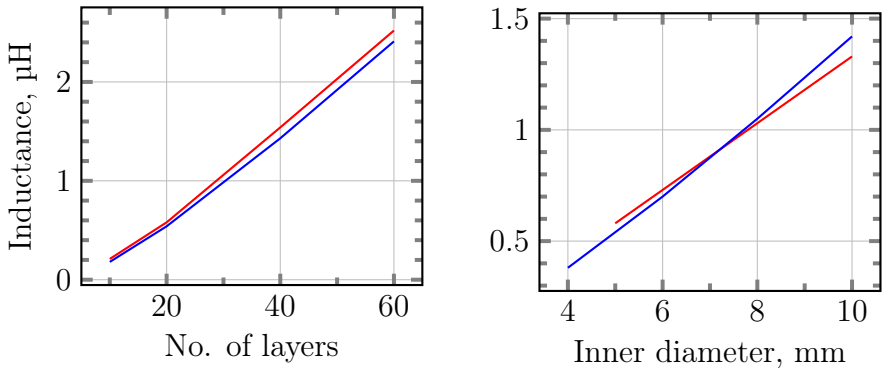

Figure 5.21: Measurement (red line) and simulation (blue line) values of inductance for different quasi-solenoid geometry parameters. Values are taken from Table 5.3.

5.2.3 Planar coil characterization

The same approach for characterization of the 3D coils was carried out for planar ones. The results are presented in the table 5.4. The advantage of the micro-sized planar coils is that they were already soldered to an SMA connector so there was no need to attach them by copper wires.

Table 5.4: Electrical characteristics of the produced coils in comparison to simulation results. The coils presented in the tables have the common parameters specified above each table.

	Measurements			Simulation		
Inner diameter (5 mm), track width (300 µm) and spacing between the turns (250 µm)						
No. of turns	L, nH	Q	f_{res}, MHz	L, nH	Q	f_{res}, MHz
4	200	38	360	157	45	518
6	460	43	231	355	59	319
Number of turns (3), track width (100 µm), spacing between the turns (100 µm)						
Inner diameter, µm	L, nH	Q	f_{res}, MHz	L, nH	Q	f_{res}, MHz
800	13.4	67	2178	8.83	17	2290
1600	30	51	1260	28.44	21	1180

5.2.4 Wireless model for coil characterization

Although some of the 3D microcoils were directly connected to the PCB for impedance measurement, most of them were characterized wirelesslly. This has been done with the help of the single wire loop, 7 mm in diameter made of 1 mm thick copper wire soldered to the single male SMA connector. This loop has been attached to the vector analyzer and brought to the vicinity of the microcoil. The inductive coupling between two inductors was used to read out the microcoil's characteristics. The principle of the wireless read-out has been laid down and described in more details in [66]. Inductive coupling can be modeled with the circuit demonstrated in figure

5.22, where R_1 and L_1 are lump elements of the loop and R_2, L_2 and C lump elements of the coil under test. As long as the frequency of operation is well below self-resonance of the wire loop (so that series model is valid), the impedance as seen from the port of the VNA will be:

$$Z_1 = R_1 + j\omega L_1 \left(1 + \frac{k^2 \left(\frac{\omega}{\omega_0}\right)^2}{1 + j\frac{\omega}{Q\omega_0} - \left(\frac{\omega}{\omega_0}\right)^2} \right) \tag{5.2}$$

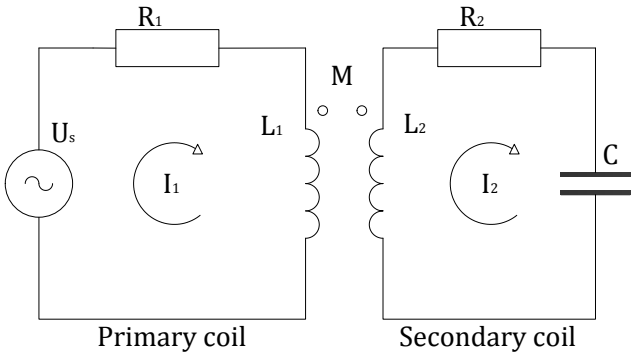

Figure 5.22: Electrical model of the inductive coupling between two coils. R_1 and L_1 are lump elements of the loop and R_2, L_2 and C lump elements of the coil under test. M is the mutual inductance between two coils.

where $\omega_0 = 2\pi f_{res}$ is the self-resonant frequency of the coil in rad/s and Q is its quality factor and k is the coupling factor that depends on position and distance of the two coils. If the values of R_1 and L_1 are known, they can be subtracted from the impedance in equation 5.2 and the scaled impedance of the coil under test can be obtained (Figure 5.23). Again, the resonant frequency is found as the frequency where imaginary part is equal to zero. The quality factor is found as the ratio of the resonant frequency and the bandwidth at the half of the impedance maximum value, as explained in chapter 2.

The results of the wireless measurements are presented in figure 5.24. The graph compares the performance of microcoils in a $Q - f_{res}$ plane. It is observable how the fabricated samples accumulate in two groups; larger microcoils with an average of f_{res} at 2.24 GHz and Q of 81.4, and smaller microcoils with an average of f_{res} at 3.76 GHz and Q of 80. The average values for each group are plotted with green circles. Standard deviations for each characteristic were calculated as a square root of the mean squared distance from the average value. Based on that, tolerances are estimated to be 5-7% for bigger coils and 1-3% for the smaller ones.

Finally, table 5.5 summarizes results for two types of microcoils and compares them to the simulation outputs. The resonant frequency f_{res} and quality factor Q are presented by their average values, which were obtained as described above. The inductance L is estimated from the direct measurements method described in the previous section.

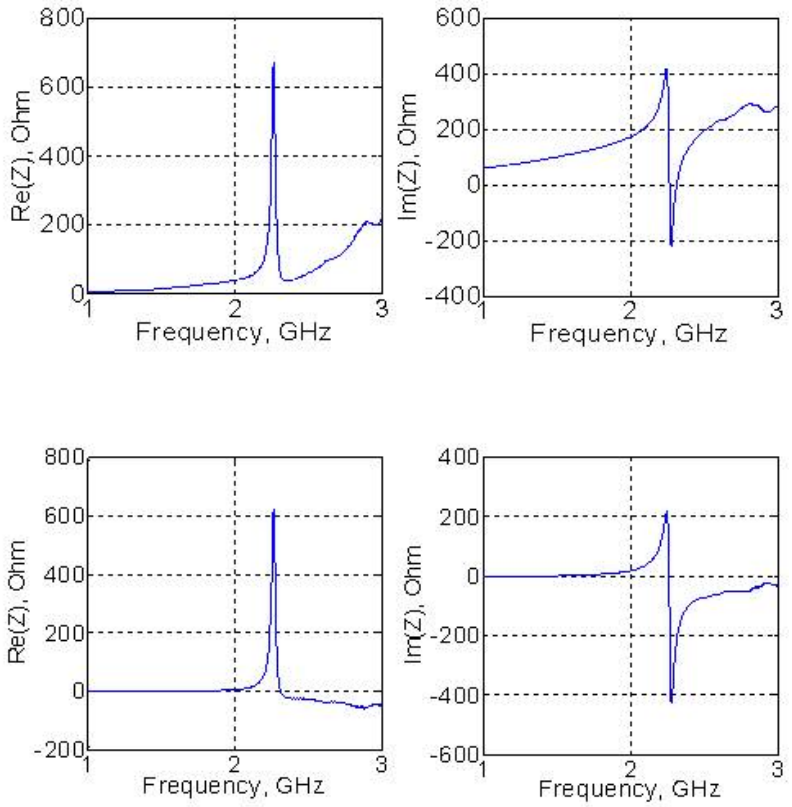

Figure 5.23: Real and imaginary part of the impedance Z (top left and right) and after subtraction of $R_1 + j\omega L_1$ (bottom left and right).

5.2.5 Twin horseshoe resonator characterization

The same model of wireless read-out explained in the previous section has been used for characterization of the twin horseshoe resonators. Only Q-factor and self-resonant frequency were of interest in this step. The results of the measurement are given in the table 5.6. In the last column the simulation results from the table 4.5 are given for comparison. Small discrepancies between the simulation and measurement are visible, but general trend of increasing self-resonant frequency with the resonator thickness is proven.

Table 5.5: Electrical characteristics of the produced microcoils in comparison to the simulated ones. The coils presented in the tables have 12 layers, 0.5 turns per layer, track width (350 µm) and the spacing between the tracks (125 µm).

	Measurements			Simulation		
Inner diameter, mm	L, nH	Q	f_{res}, GHz	L, nH	Q	f_{res}, GHz
0.85	26.08	79.8	3.76	20.06	66	3.7
1.5	56.43	89.4	2.241	46	55	1.9

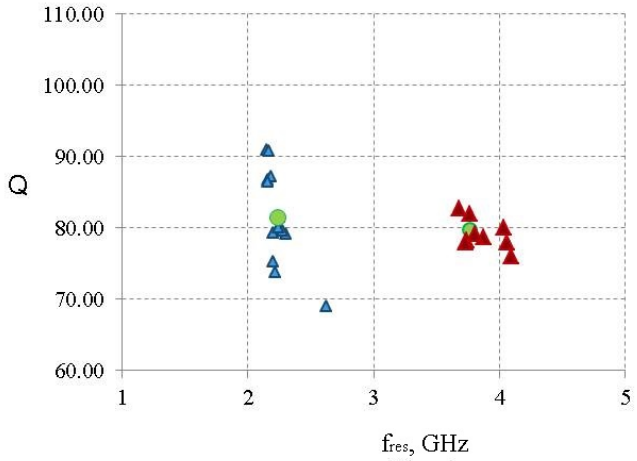

Figure 5.24: Measured values of Q-factor and self-resonant frequency of the micrcoil represented in $Q - f_{res}$ plane. Smaller microcoils are depicted as blue triangles, and larger as red diamonds. Fabricated samples accumulate in two groups whose average values are plotted with green circles.

Table 5.6: Electrical characteristics of the produced horseshoe resonators in comparison to the simulated ones. The resonators presented in the table have the same inner radius (4.5 mm), track width (2.5 mm) and gap width (5 mm).

	Measurement		Simulation
Spacing between the tracks, µm	Q	f_{res}, MHz	f_{res}, MHz
50	210	343.9	-
100	172	476.5	390
125	167	466	560
250	152	672.3	695
375	207	811.6	790
500	196	947.1	890

Chapter 6

NMR measurements and results

6.1 NMR Measurement set-up

NMR measurements have been performed in a NMR Laboratory at the Karl-Franzens University of Graz. For most measurements the nuclear quadrupolar resonance (NQR) of Cu in CuO at 26 MHz was utilized. In a few coils with too small inductance for this frequency the zero (external) field nuclear magnetic resonance (NMR) of metallic, ferromagnetic fcc-Co at 213 MHz was measured. The spectrometer consists of frequency synthesizer, power amplifier, attenuator switch, LC resonant circuit and receiver. The operation of the system is explained in section 2.3. The LC resonator used for detection is depicted on the figure 6.1. C_t and L_t are tunable components for tuning the resonant frequency of the circuit to the NMR (NQR) frequency and matching the resonator to the 50 Ω transmission line. L_{sample} is a LTCC coil that holds the sample being measured in the NMR experiment. While the tuning capacitor is a rigid device with screw handle that enables capacitance range from 1.5 pF to 450 pF, the matching coil is nothing more than a few loops of 200 µm copper wire. Impedance matching is done manually, by changing the size and shape of the loops. The whole circuit is tuned and matched with the help of Le Croy WaveSurfer oscilloscope and a signal at the NMR or NQR frequency from the Rhode & Schwarz synthesizer. The matching is managed by changing the C_t and L_t so that the signal reflected from the circulator connected to the output of the synthesizer, probe-head and the oscilloscope is minimized. For each L_{sample} coil, tuning and matching process goes anew. The whole circuit, including the pick-up wire is housed in the aluminum box during the operation.

Radio frequency pulses are cut out of the continuous wave from the synthesizer set to a specific amplitude by a variable attenuator and amplified by approximately 45 dB by a power amplifier. Before passing to the probe-head, the pulsed signal is attenuated by a variable attenuator which enables the attenuation in discrete 1 dB step from 0 to 20 dB. Impact of this parameter is studied further in the NMR/NQR measurements because it is the decisive parameter in determining the maximum signal of NMR/NQR as will be discussed in the following section.

The amplification in the receiver system occurs in two stages. The Doty Scientific LN-2L pre-amplifier nominally has 31±2 dB gain and a typical noise figure of 1.0 dB. Its input is connected to the LC-resonator via a 'magic T' which reduces signal by up to 3 dB. The Bruker quadrature receiver system has a nominal 30 dB gain in a first stage, and an additional 20 dB in the phase sensitive detection stage. After the quadrature mixing stage there is a low pass filter set to 100 kHz for present experiments. Between the pre-amplifier and the receiver sits a variable attenuator that prevents the overdrive of the receiver. A digital oscilloscope (LeCroy WaveSurfer) receives the two output channels of the quadrature mixer during a detection time

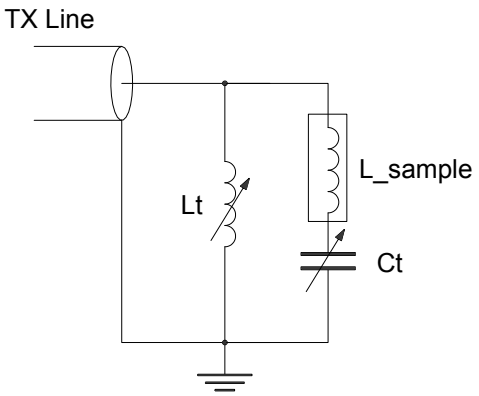

Figure 6.1: LC resonator for the NMR signal detection. C_t and L_t are tunable components that enable adequate tuning and matching of the circuit to the 50 Ω transmission line.

window. It is set and triggered by the computer controlling the spectrometer.

6.2 Measurement results

The software for instrument control, signal acquisition and processing was developed by Dr. Pieper from the Karl-Franzens University of Graz.

The measurement of a given coil consists of a series of measurements of the NQR (or NMR) signal from the tuned and matched resonance circuit with varying pulse amplitudes. Up to 17 different pulse amplitudes are were measured to determine the 90° condition for each coil as the attenuation with maximum echo signal (see Chapter 2). One measurement completion consists of multiple sequences, each acquired of 20 averages. Each sequence begins with the pulse excitation followed by the certain rest time followed by another pulse two times longer than the first one. Response of such excitation is FID signal after the first (90°-) pulse and spin echo after the second (180°-) pulse.

Figure 6.2 shows a NQR signal in CuO in the time domain (top) and Fast Fourier Transform (FFT) of a user specified time window (chosen to include the full echo and zero padded to improve resolution) in the frequency domain (bottom). The signal is integrated in user specified time and frequency windows and integrals are used for the signal power estimation and the FFT. This procedure is repeated for each sequence with different pulse attenuations. The results of the measurement are stored in a separate ASCII file (.log) containing information on number of sequence (0-19), signal maximum value, FFT absolute value at the excitation frequency, and finally, root-mean-square noise value.

Figure 6.3 shows the maximum signal value vs. attenuation pulse. From this one can deduce B_1 field produced within the coil in time and frequency domain. For a pulse sequence $\tau_1 - \tau_{rest} - \tau_2$, the echo signal amplitude is:

$$S = C \sin(\gamma B_1 \tau_1) \sin^2(\gamma B_1 \tau_2/2) \tag{6.1}$$

where C is a factor of proportionality. The pulse length for CuO samples was 3 µs and for Co samples 0.3 µs. To achieve the 90° flip in the Cuo samples, where gyromagnetic ratio γ is 11.3 MHz/T with a 3 µs long pulse it is necessary to produce

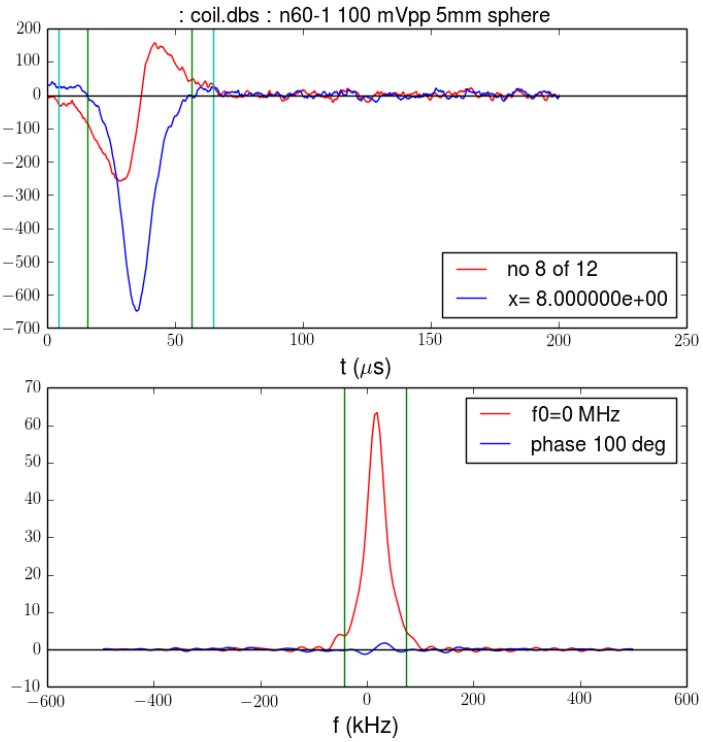

Figure 6.2: An example of NMR experiment output. The data is presented in time as well as in frequency domain (real parts in red, imaginary parts in blue). Green windows are boundaries of the time and frequency integration, and the blue window sets the FFT integration limits.

the B_1 field of amplitude $\pi/2\gamma\tau = 45\,\mathrm{mT}$. A comparison of measurement values to the prediction from 6.1 is depicted in figure 6.3 for both CuO and Co samples.

6.2.1 Room temperature measurements

In this section the measurement data per each fabricated and tested coil is discussed. Not all of the fabricated coils could be used in NQR system, since few of them, for instance 20-layered, 6 turns per layer spiral, had a self resonant frequency below the working NQR frequency. Some coils, for instance planar coils, had a self-resonant frequency too close to 26 MHz so no small enough capacitor was available to tune the LC resonator to this frequency. And some other coils, e.g. planar microcoils had a self resonance at such high frequency that no capacitor big enough was available for appropriate tuning.

For the SNR calculation maximum signal in the time domain is taken from the pulse sequence identified as 90°-pulse and the noise power was taken as the average power of the last 100 values detected after the time window of the echo signal. The SNR is calculated as maximum signal divided by average noise while the SNR_{puv} is calculated as SNR divided by the sample volume. For most of the coils the NMR sample was of the same size (5 mm diameter sphere), but for the coil with the inner diameter of 10 mm the copper oxide sample was of the also 10 mm sphere. The SNR_{puv} is presented in units of cm^{-3}. The scale varies from coil to coil depending on the attenuation on the receiver side. There was no need to convert the values to the voltage across the terminals of the coil or the induced current since the relative

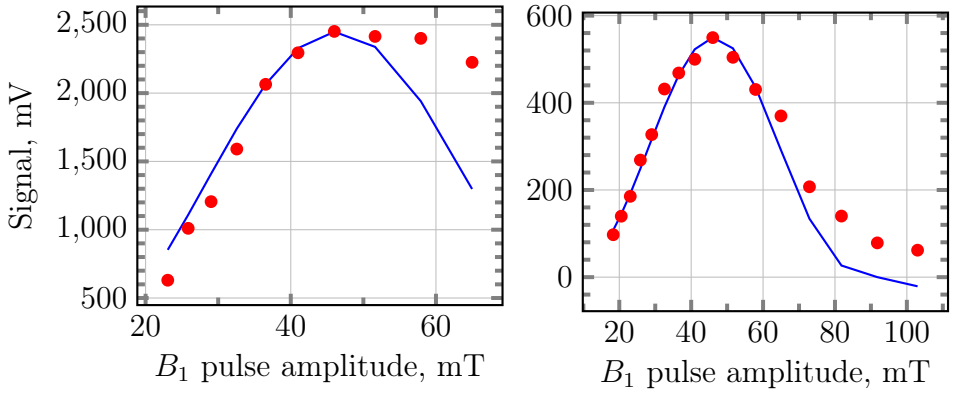

Figure 6.3: NMR signal dependence on B_1 pulse amplitude for two different coils. Measured data (red dots) interpolates well with the prediction from equation 6.1 (blue line). The peak value is the pulse amplitude that causes 90° pulse and in these two cases equals 46 mT.

SNR is the value we're interested in.

Comparison of LTCC coils for different geometries

Comparison of the SNR_{puv} for different coils is depicted in figure 6.4 along with relation of the experimental values to those from theoretical analysis from chapter 4. Table 6.1 presents details of executed experiments. The theory predicts that for certain coil geometries SNR_{puv} exhibits a maximum in respect to the number of layers and track width. Exactly this is visible on top and bottom graphs in figure 6.4. For some other parameters, e.g. coil inner radius SNR_{puv} declines monotonically.

Comparison of LTCC microcoils and copper wire coils

Also interesting are the measurement results of the microcoil design described in chapter 4. The comparison of this coil to an ordinary hand wound copper coil proves the advantages of the LTCC technology. The microcoil has been used for 1 mm^3 cobalt sample that exhibits nuclear magnetic resonance at 213 MHz in the internal magnetic field of ferromagnetic metallic Co. The signal of the microcoil is averaged 100 times, in contrast to usual 20 averages. The SNR_{puv} of the microcoil is compared to the one of the copper coil in table 6.3. It is known that averaging of N_{avg} samples improves the SNR by factor $\sqrt{N_{avg}}$. Hence, for comparison of these two coils, the SNR_{puv} is divided by $\sqrt{N_{avg}}$. It is clear that LTCC coils performs with about 50 times better SNR_{puv}.

6.2.2 Cryogenic probe measurements

As explained in chapter 2, one way to increase the sensitivity of an NMR experiment is to perform it at temperatures as low as possible. One available way was to use liquid nitrogen vessel where temperature of 77 K was reached, the boiling temperature of N_2 at ambient air pressure. The special kind of NMR probe used for this experiment is a *cryogenic probe head* with the LC-resonator containing a low temperature tunable capacitor and the sample and matching coils placed at the end of a (1.5 m) long non-magnetic metal tube. A low temperature 50 Ω coax line and the mechanism for tuning the capacitor are fed through the tube to the top which stays at room temperature. Not only will the electronics of probe-head get distorted by drastic change in temperature, but also will the NQR frequency of the

Table 6.1: NMR measurement data for 3D coils with different geometry parameters for the same sample of CuO. Presented data is shown for the equal NMR experiment settings: pulse amplitude set to 90° pulse, pulse sequence 0.3 µs - 12 µs - 0.3 µs, 20 averages.

	Max. signal, mV	Avg. Noise, mV	SNR_{puv}
0.5 windings per layer, inner diameter (5 mm), track width (350 µm), spacing between the layers (125 µm). No. of layers			
10	2451	115	40.46
20	3164	123	49.15
40	3316	92	68.48
60	2746	80	65.32
0.5 windings per layer, 20 layers, inner diameter (5 mm), spacing between the layers (125 µm). Track width µm			
350	3164	123	49.15
3000	3710	128	55.43
0.5 windings per layer, 20 layers, track width (350 µm), spacing between the layers (125 µm). Inner diameter mm			
5	3164	123	49.15
10	4264	93	10.96
20 layers, track width (350 µm), spacing between the layers (500 µm). No. of turns per layer mm			
4	2181	56	36.62
6	1350	51	21.67

Table 6.2: NMR measurement data for planar coils with different geometry parameters for the same 5 mm sphere sample of Co. Presented data is shown for the equal NMR experiment settings: pulse amplitude set to 90° pulse, pulse sequence 0.3 µs - 12 µs - 0.3 µs, 20 averages.

No. of turns	Max. signal, mV	Avg. Noise, mV	SNR_{puv}
Inner diameter (5 mm), track width (350 µm).			
4	298	5.8	65.50
6	2001	86	44.09

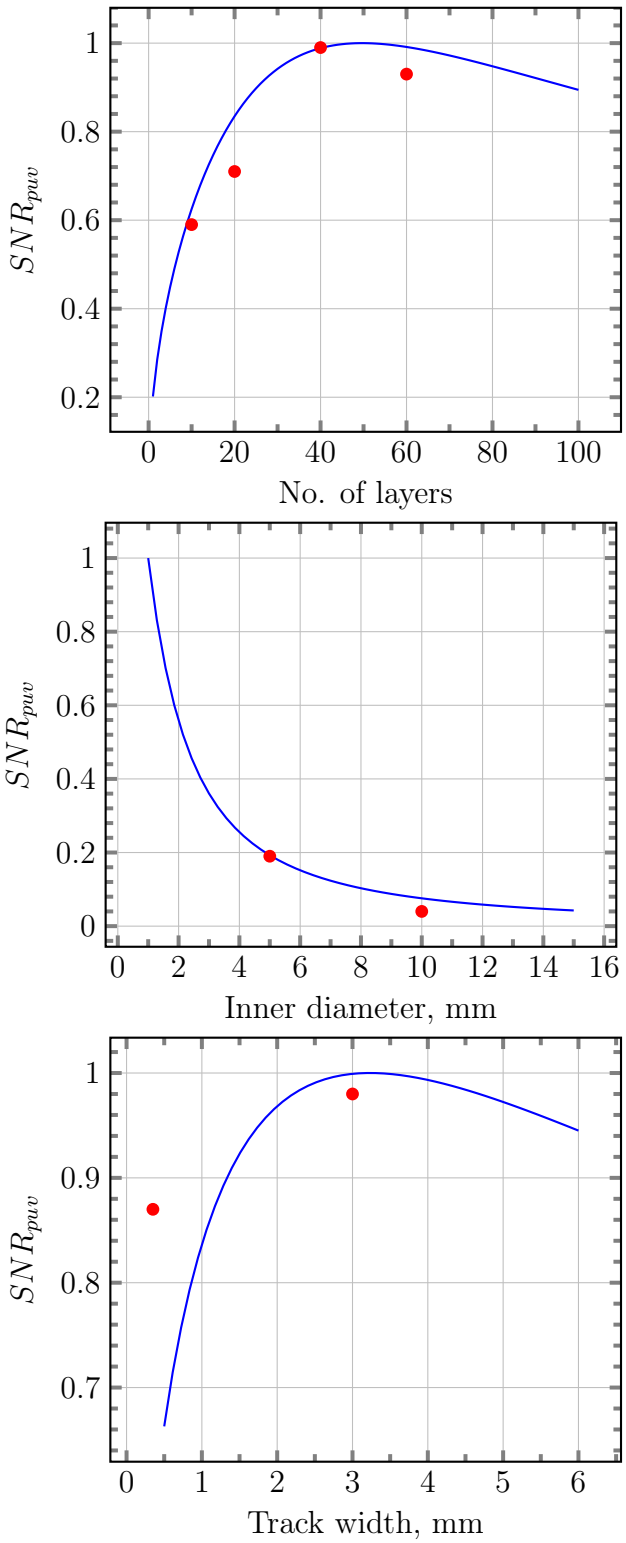

Figure 6.4: SNR_{puv} of 3D quasi solenoidal coils for various geometry parameters. Blue line depicts analytical model while the red dots show the actual NMR measurement data. All SNR values are normalized.

Table 6.3: NMR measurement data comparison for microcoil of inner diameter (0.85 mm), 12 layers, track width (150 µm), spacing between the layers (125 µm) and copper wire of inner diameter (5 mm), 20 windings and wire width (150 µm).

	Sample volume, cm^3	No. of averages, N_{avg}	Max. signal, mV	RMS noise, mV	$SNR_{puv}/\sqrt{N_{avg}}$
Microcoil	10^{-3}	100	550	14.45	3806.2
Cu wire	0.5	20	196	1.1	79.6

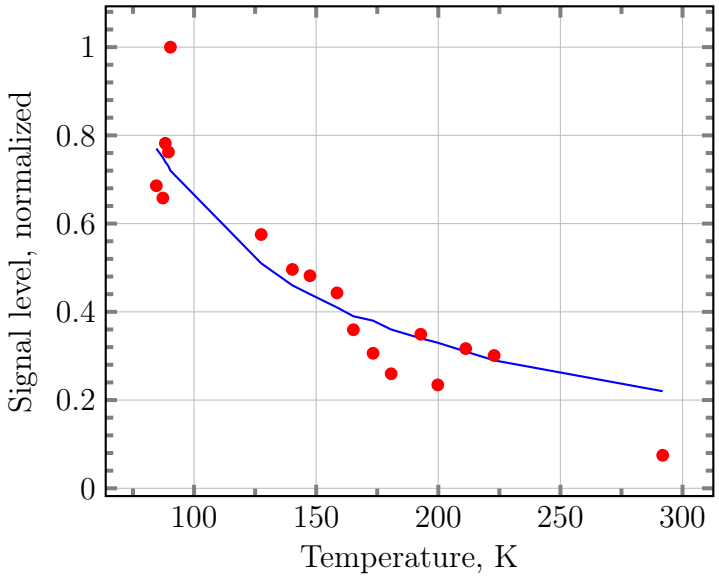

Figure 6.5: NMR signal in dependence on temperature. As expected from Chapter 2, induced signal (red dots) follows the $1/T$ law (blue line).

sample. The intrinsic NQR frequency of ^{63}Cu in CuO depends slightly on temperature, so LC-resonator is tuned at each temperature to match the NQR frequency. The matching, on the other hand, is only adjusted at room temperature and it varies with the temperature, mainly due to the temperature dependence of the resistivity of the coil. At each temperature the signal was measured at the resonance frequency with the other NMR parameters constant.

The cryogenic probe measurement results are depicted in figure 6.5. A series of measurements from 80 to 290 K has been executed and signal processed. Signal had to be normalized due to the different receiver attenuations and number of averages per each step. Finally, echo amplitude is plotted against the temperature and $1/T$ nature of Curie's law of paramagnetism is clearly seen. Because of the temperature dependent shift of the Larmor frequency, the amplitude was extracted from the Fourier transformed signal. The plot diverges from the ideal $1/T$ curve from reasons of strong temperature dependence of probe-head electronics.

As always, SNR_{puv} has been calculated taking in the account different averages per each temperature measurement, and plotted in figure 6.6. The SNR_{puv} doesn't follow the same temperature dependence as signal amplitude because of non-linear temperature behavior of the coil's resistance, i.e. thermal noise. However, improvement of the SNR by reducing the temperature of the sample is proven by this measurement.

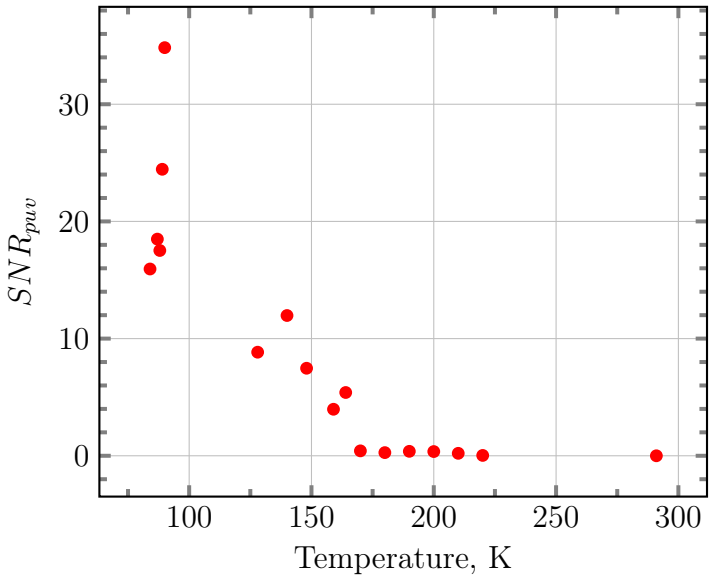

Figure 6.6: SNR_{puv} in dependence on temperature. The SNR_{puv} doesn't follow the same temperature dependence as signal amplitude because of non-linear temperature behavior of the coil's resistance.

Chapter 7

Conclusion

Discussion

The aim of this research has been to design a coil in a low temperature co-fired ceramics technology that may be implemented in NMR spectrometer probe heads. NMR spectrometry is a material examination technique that has inherent lack of sensitivity due to the extremely small magnetic moments of active nuclei within the sample under test. The sensitivity may be improved by changing some experimental parameters like magnetic field or sample temperature or, as in the case of this thesis, by manipulating geometrical properties and the design of the coil. The main reasons why the LTCC technology was employed are the low dielectric losses of ceramic substrate and the superior thermo-mechanical stability of ceramics.

Multiple coil sets that have been fabricated can be divided in two major groups: three-dimensional (3D) and two-dimensional (2D) coils. The principal difference between these two groups is that in 3D coils the NMR sample is encapsulated within the coil substrate, while in 2D coils the sample is placed above the coil plane. These coils were realized in different commercially available LTCC materials, e.g. Heraeus CT708, CeramTape GC and silver pastes TC7304 and TC7306. Electric and magnetic properties of these materials were known from previous research as explained in chapter 3. Each coil design was preceded by mathematical analysis and finite element method simulation the goal of which was to get a deeper understanding of coil performance. Most importantly, it was examined how geometrical parameters influence the quality of the NMR experiment, quantifiable by signal-to-noise ratio. It has been found that for a given sample size certain coil parameters, like number of windings and track width, deliver local maximum for SNR (Figures 4.15, 4.25 and 4.8). It was also shown how the magnetic field homogeneity of the coils varies for different geometries. Finally, best geometrical values in terms of number of windings, track width, diameter, etc. were chosen and coils fabricated accordingly.

Because of diverse coil types, from micro-sized to 60-layered coils, a lot of deviations from standard LTCC fabrication procedure were required and needed to be experienced. All the production details are presented and discussed. The electrical characterization of the coils yielded results confirming assumptions as theoretically predicted in chapter 2: the inductance rises linearly with the number of layers and exponentially with the number of windings per layer. In contrast, the Q factor is independent of most parameters investigated and decreases significantly only with increasing number of tracks per layer and number of layers. Reasons for that are the eddy current losses within the conductive tracks and the resistance of the vias, whose number grows with the number of layers. As can be seen on the micro-sections depicted in figures 5.11 and 5.12 the vias seem to have larger surface on the top than on the bottom. This is a consequence of the conical shape of the laser beam and

results in slightly higher via resistance. This might be avoided by using different laser profiles where multiple laser cuts lead to a cylindrical via shape.

From the electrical characterization the reproducibility of the LTCC process can be evaluated. The measurements of the produced coils show deviations from nominal values of up to 10 %, as shown in wireless microcoil measurement (Figure 5.24). This happens because of the production at the lower end of possible dimensions in LTCC technology. An additional reason is that each coil has been produced individually by manually driven processes with respective tolerances. Certain deviations in production parameters like screen printer speed or firing profile lead to certain deviations in the final outcome.

NMR measurements were supposed to be final supporting step of this research. Ideally, all produced coils would have been embedded in the NMR probe head and their *SNR* measured, and compared in similar manner as in the simulation chapter . But, due to the limited span of probe head's tuning range not all of the coils could be tuned to the frequency of the NMR experiment. Two resonant frequencies were used in the study: 26 MHz for CuO samples and 213 MHz for Co samples. The spectrometer delivered a spin echo response from the sample, which was later processed on a PC. The primary interest was to extract the NMR signal amplitude and average noise delivered on the receiver side together with the NMR related parameters which have an influence on the signal amplitude but not on the root-mean-square noise amplitude. The results are presented in the chapter 6.

Due to the limited number of tested coils, the figures are somewhat unsatisfying in a way that they do not show exact curves as the ones from the simulation section. However, the important trends from the theoretical calculations are confirmed as the graphs in figures 6.4 depict. The coils indeed do follow the general rule for maximum SNR_{puv}, which is in good agreement with the mathematical analysis. It is reasonable to expect that this rule would be supported if more samples were available.

The "big" coils were fabricated and tested in NMR spectrometer mainly for one purpose: validating mathematical model analysis. However, the true advantages of LTCC technology arise from the design of specialized microcoils. The sample which was tested in NMR spectrometer yielded convincingly the highest SNR_{puv} of all coils and is comparably better than the copper wire coil that is being usually employed in this field (Table 6.3). That was the true intention of this thesis – developing high quality NMR coil in ceramic technology. Apart from *SNR*, there are many other reasons for using LTCC in this field: first of all being thermal stability at the temperatures as low as 80 K, what has been proven in section 6.2.2. Knowing that typical field pulse amplitude is about 50 mT, and that a typical NMR coil has an inductance of 1 µH it is easily shown that at the frequency of few tens of MHz a current of few tens of amperes flows through the coil developing a voltage of few kilovolts across the coil terminals. Such extreme working conditions prove superiority of LTCC over other thick film technologies.

Outlook

Although the core topic of this thesis was the development of NMR coils, not all of the advantageous possibilities of LTCC technology were exploited. Since the LTCC enables development of various structures, the whole LC circuit could have been fabricated on a single substrate. That would, however, require powerful RF simulation tool and different RF circuit designs that would cover various research fields. One important limitation of the embedded passive components is a comparatively low electric breakdown. During the excitation pulse the substrate is exposed to the voltages of few kV, which could lead to the destruction of an LTCC capacitor, the values of which would be in pF range, for the thickness of few hundreds of micrometers.

Additionally, small active semiconductor circuits, e.g. pre-amplifier, could be embedded within the substrate. In case of embedding such devices there is a certain possibility of electromagnetic interference originating from the power supply cables. It is very undesirable to have any active circuitry within the probe head next to the sensor that produces small voltage output.

Finally, micro-channels are a very attractive field of study in both NMR and LTCC technology, as explained in the Introduction. A design of two planar coils in Helmholtz configuration with the channel in between was suggested by the author in [13]. However, a successful research would presuppose the availability of a fluid NMR spectrometer.

Generally, this coil design is not necessarily limited for NMR applications. There are countless examples where the proposed design of quasi-solenoidal coil may be used, starting from the general purpose inductors to the high power RF transformers.

Acknowledgments

Firstly, I would like to express my sincere gratitude to my first advisor Prof. Dr. Nicolics for the continuous support of my Ph.D study and related research, for his patience, motivation and immense knowledge. Most of all, I am thankful for giving me a full freedom to research the subject I had my scientific interest in.

Special thanks go to my second supervisor, Prof. Dr. Pieper without whom this Ph.D. would not be possible. His NMR spectrometer served for the crucial measurements made within this research and his guidance helped me in all the time of research and writing of this thesis. His insightful comments have always lead me to navigate through this research in the best way.

My sincere thanks also goes to my fellow workmates for the stimulating discussions, perceptive comments, and encouragement. Special thanks to my colleagues Goran Mišković, Michael Unger, Manuela Franz and Heinz Homolka for helping me out with the most sensitive elements of the research. I am grateful to my former colleagues Dr. Goran Radosavljević and Dr. Michael Weilguni for introducing me to the laboratory and LTCC technology. Many thanks to my colleague Dr. Paul Fulmek for his always present will to help with the most challenging problems I encountered.

My sincere thanks to Prof. Dr. Holger Arthaber from IEMCE for stepping forward in the time when I desperately needed help to build a NMR spectrometer for the completion of this thesis.

I would like to thank my family for firmly believing in me and all the moral support they provided through my time as a Ph.D. student and generally in life.

Finally, to my Helena who has been there for me in every moment of doubt and always pulled the best out of me.

Bibliography

[1] D.I Hoult and R.E Richards. The signal-to-noise ratio of the nuclear magnetic resonance experiment. *Journal of Magnetic Resonance (1969)*, 24(1):71–85, 1976.

[2] Tim L. Peck, R. L. Magin, and P.C Lauterbur. Design and analysis of microcoils for nmr microscopy. *Journal of Magnetic Resonance*, 108:114–124, 1995.

[3] H. Vesselle and R. E. Collin. The signal-to-noise ratio of nuclear magnetic resonance surface coils and application to a lossy dielectric cylinder model - part i: Theory. *IEEE Transactions on Biomedical Engineering, vol. 42, No. 5. May 1995*, 42(5):497–506, 1995.

[4] H. Vesselle and R. E. Collin. The signal-to-noise ratio of nuclear magnetic resonance surface coils and application to a lossy dielectric cylinder model - part ii: The case of cylindrical window coils. *IEEE Transactions on Biomedical Engineering, vol. 42, No. 5. May 1995*, 42(5):507–520, 1995.

[5] AJ. Blodgett and D. R. Barbour. Thermal Conduction Module: A High-Performance Multilayer Ceramic Package. *IBM Journal of Research and Development*, 26(1):30–36, Jan 1982.

[6] Yoshihiko Imanaka. *Multilayered Low Temperature Cofired Ceramics (LTCC) Technology*. Springer, 2005.

[7] Fred D. Barlow and Aicha Elshabini. *Ceramic interconnect technology handbook*. CRC Press/Taylor & Francis, 2007.

[8] A. Fathy, V. Pendrick, G. Ayers, B. Geller, Y. Narayan, B. Thaler, H.D. Chen, M.J. Liberatore, J. Prokop, K.L. Choi, and M. Swaminathan. Design of embedded passive components in low-temperature cofired ceramic on metal (ltcc-m) technology. In *IEEE MTT-S International Microwave Symposium Digest*, volume 3, pages 1281–1284 vol.3, June 1998.

[9] E. Loskot, V. Kondratiev, I. Vendik, E. Jakku, and S. Leppavuori. Design of resonators and filters based on ltcc lumped components. In *IEEE Proc. of 30th European Microwave Conference*, pages 1–4, Oct 2000.

[10] L.K. Yeung, K.-L. Wu, and Y.E. Wang. Low-temperature cofired ceramic lc filters for rf applications [applications notes]. *Microwave Magazine, IEEE*, 9(5):118–128, Oct 2008.

[11] G. Radosavljevic, A. Maric, L. Zivanov, and W. Smetana. Realization of high quality RF inductors using LTCC technology. In *Telecommunications Forum (TELFOR), 2011 19th*, pages 984–987, Nov 2011.

[12] Andrea Marić, Nelu Blaž, Ljiljana Živanov, and Goran Radosavljević. Fine tuning of 3d ltcc inductor properties using combination of different ferrite and dielectric tapes. *International Journal of Applied Ceramic Technology*, 2014.

[13] P. Krivic, M. Weilguni, and G. Radosavljevic. Realization of three-dimensional solenoidal microcoils with air core in low temperature co-fired ceramics technology. In *IEEE Proc. of 36th International Spring Seminar on Electronics Technology (ISSE)*, pages 59–63, May 2013.

[14] Erick Kim, Young-Shin Lee, Chan-Sei Yoo, Woo-Seong Lee, and Jong-Cheol Park. A power amplifier module with fully embedded passive components in a LTCC substrate for K-PCS band mobile phone. In *IEEE Proc. 33rd European of Microwave Conference, 2003.*, volume 1, pages 253–256 Vol.1, Oct 2003.

[15] V. Napijalo, V. Cojocaru, and T. Yokoyama. 24 GHz LTCC Amplifier Using Packaged HEMTs. In *IEEE Proc. of European Microwave Integrated Circuit Conference (EuMIC)*, pages 462–465, Oct 2008.

[16] D. Heo, A. Sutono, E. Chen, Y. Suh, and J. Laskar. A 1.9-GHz DECT CMOS power amplifier with fully integrated multilayer LTCC passives. *Microwave and Wireless Components Letters, IEEE*, 11(6):249–251, June 2001.

[17] G. Radosavljevic, L. Zivanov, A. Maric, L. Nao, W. Smetana, and M. Unger. Performance improvement of a resonant pressure sensor by means of model based design optimisation. In *Sensors, 2008 IEEE*, pages 1008–1011, Oct 2008.

[18] G.J. Radosavljević, L.D. Zivanov, W. Smetana, A.M. Marić, M. Unger, and L.F. Nad. A Wireless Embedded Resonant Pressure Sensor Fabricated in the Standard LTCC Technology. *Sensors Journal, IEEE*, 9(12):1956–1962, Dec 2009.

[19] M. Hrovat, D. Belavic, H. Ursic, J. Kita, Janez Holc, S. Drnovsek, J. Cilensek, Marija Kosec, and R. Moos. An Investigation of thick-film materials for temperature and pressure sensors on self-constrained ltcc substrates. In *Electronics System-Integration Technology Conference, 2008. ESTC 2008. 2nd*, pages 339–346, Sept 2008.

[20] D. Belavic, M.S. Zarnik, S. Macek, M. Jerlah, M. Hrovat, and M. Pavlin. Capacitive Pressure Sensors Realized with LTCC technology. In *IEEE Proc. of 31st International Spring Seminar on Electronics Technology (ISSE)*, pages 269–272, May 2008.

[21] I. Atassi, W. Smetana, E. Gaubitzer, M. Edetsberger, and G. Kohler. Evaluation of Flow Characteristics of Fluids in a Microperfusion Cell by Means of Finite Element Analyses. In *Electronics Technology, 30th International Spring Seminar on*, pages 106–111, May 2007.

[22] X.S. Wang, B. Balluch, W. Smetana, and G. Stangl. Optimization of cavity fabrication for micro-fluidic systems. In *IEEE Proc. of 31st International Spring Seminar on Electronics Technology, (ISSE)*, pages 414–419, May 2008.

[23] M. Weilguni. *Force Sensors for the Measurement of Finger Forces in Clarinet Playing.* PhD thesis, Vienna University of Technology, May 2013.

[24] M. Weilguni, W. Smetana, G. Radosavljević, J. Nicolics, A. Hofmann, and W. Goebl. A ring-shaped LTCC/HTCC sensor for detection of finger forces in clarinet playing. In *IEEE Sensors*, pages 1–4, Oct 2012.

[25] P. Karioja, K. Kautio, J. Ollila, K. Keranen, M. Karppinen, V. Heikkinen, T. Jaakola, and M. Lahti. MEMS, MOEMS, RF-MEMS and photonics packaging based on LTCC technology. In *Proc. of Electronics System-Integration Technology Conference (ESTC)*, pages 1–6, Sept 2014.

[26] Chandrakant Patel, Adwaita Jadhav, Sudhir Lone, Vivek Rane, Varsha Chaware, Vijaya Giramkar, and Girish Phatak. Miniaturization of LTCC based hot plates for gas sensors application. In *1st International Symposium on Physics and Technology of Sensors (ISPTS)*, pages 83–86, March 2012.

[27] I. Giangu, V. Buiculescu, G. Konstantinidis, K. Szacilowski, A. Stefanescu, F. Bechtold, K. Pilarczyk, A. Stavrinidis, P. Kwolek, G. Stavrinidis, J. Mech, and A. Muller. Acoustic wave sensing devices and their LTCC packaging. In *Proc. of International Semiconductor Conference (CAS)*, pages 147–150, Oct 2014.

[28] A. Abragam. *Principles of Nuclear Magnetism*. Oxford University Press, 1961.

[29] Zhi-Pei Liang and Paul C. Lauterbur. *Principles of Magnetic Resonance Imaging: A Signal Processing Perspective*. Wiley-IEEE Press, 1st edition, 1999.

[30] C.P. Slicher. *Principles of Magnetic Resonance*. Springer, 3rd edition, 1992.

[31] E. L. Hahn. Spin echoes. *Phys. Rev.*, 80:580–594, Nov 1950.

[32] J.D. Jackson. *Classical Electrodynamics*. Wiley-IEEE Press, 3rd edition, 1998.

[33] T. P. Das and E. Hahn. *Nuclear quadrupole resonance spectroscopy*. New York : Academic Press, 1st edition, 1958.

[34] D.I Hoult. The principle of reciprocity. *Journal of Magnetic Resonance*, 213(2):344–346, 2011.

[35] S. Eroglu, G. Friedman, and R. L. Magin. Estimate of losses and signal-to-noise ratio in planar inductive micro-coil detectors used for nmr. *IEEE Transactions on Biomedical Engineering, vol. 37, No. 4. July 2001*, 37(4), 2001.

[36] P. J. M. van Bentum, J. W. G. Janssen, and A. P. M. Kentgens. Towards nuclear magnetic resonance microspectroscopy and microimaging. *Analyst*, 129(9):793–803, 2004.

[37] S. Eroglu, S. C. Grant, G. Friedman, and R. L. Magin, editors. *Investigation of RF Spiral Surface Coils for NMR Spectroscopy*. IEEE, 2000.

[38] Kevin R. Minard and Robert A. Wind. Solenoidal microcoil design. part i: Optimizing rf homogeneity and coil dimensions. *Concepts in Magnetic Resonance*, 13(2):128–142, 2001.

[39] Kevin R. Minard and Robert A. Wind. Solenoidal microcoil design. part ii: Optimizing winding paramteres for maximum signal-to-noise performance. *Concepts in Magnetic Resonance*, 13(2):128–142, 2001.

[40] Frank Engelke. Electromagnetic wave compression and radio frequency homogeneity in nmr solenoidal coils: Computational approach. *Concepts in Magnetic Resonance*, 15(2):129–155, 2002.

[41] Andrew G. Webb. Radiofrequency microcoils in magnetic resonance. *Progress in Nuclear Magnetic Resonance Spectroscopy*, 31(1):1–42, 1997.

[42] Sertac Eroglu, Barjor Gimi, Brian Roman, Gary Friedman, and Richard L. Magin. Nmr spiral surface microcoils: Design, fabrication, and imaging. *Concepts in Magnetic Resonance*, 17(1):1–10, 2003.

[43] C. Massin, F. Vincent, A. Homsy, K. Ehrmann, G. Boero, P.-A Besse, A. Daridon, E. Verpoorte, N.F de Rooij, and R.S Popovic. Planar microcoil-based microfluidic nmr pobes. *Journal of Magnetic Resonance*, 164, 2003.

[44] C. Massin, C. Azevedo, N. Beckmann, P.-A Besse, and R.S Popovic, editors. *Magnetic Resonance Imaging using Microfabricated Planar Coils*, 2002.

[45] C. Massin, G. Boero, F. Vincent, J. Abenhaim, P.-A Besse, and R.S Popovic. High-q factor rf planar microcoils for micro-scale nmr spectroscopy. *Sensors and actuators*, 2002.

[46] C. Massin, S. Eroglu, F. Vincent, B. S. Gimi, P.-A Besse, R. L. Magin, and R.S Popovic, editors. *Planar Microcoil-based Magnetic Resonance Imaging of Cells*, Piscataway and N.J, 2003. IEEE.

[47] Tim L. Peck, Richard L. Magin, J. Kruse, and M. Feng. Nmr microspectroscopy using 100 um planar rf coils fabricated on gallium arsenide substrates. *IEEE Transactions on Biomedical Engineering, vol. 41, No. 7. July 1994*, 41(7):706–709, 1994.

[48] Tim L. Peck, J.E Stocker, Z. Chen, L. LaValle, and R. L. Magin, editors. *Application pf Planar Microcoils fabricated on glass substrates to NMR Micropectroscopy*. IEEE, 1997.

[49] Barjor Gimi, Sertac Eroglu, Lara Leoni, Tejal A. Desai, Richard L. Magin, and Brian B. Roman. Nmr spiral surface microcoils: Applications. *Concepts in Magnetic Resonance*, 18(1):1–8, 2003.

[50] K. Ehrmann, M. Gersbach, P. Pascoal, F. Vincent, C. Massin, D. Stamou, P.-A Besse, H. Vogel, and R.S Popovic. Sample patterning on nmr surface microcoils. *Journal of Magnetic Resonance*, 178(1):96–105, 2006.

[51] N. Baxan, A. Rengle, J.-F Chateaux, A. Briguet, G. Pasquet, P. Morin, and L. Fakri-Bouchet, editors. *NMR Planar Micro coils for micro spectroscopy: Design and characterization*, 2006.

[52] N. Baxan, A. Rengle, G. Pasquet, J.-F Chateaux, A. Briguet, P. Morin, and L. Fakri-Bouchet, editors. *Investigation of NMR limits of detection for implantable microcoils*, [Piscataway and N.J.], 2007. IEEE.

[53] M. Grant Carter, C. Barry ynd Norton. *Ceramic Materials: Science and Engineering*. Springer-Verlag New York, 2007.

[54] M. Unger, W. Smetana, and W. Ehrenzweig. Mechanical Characteristics of LTCC (Low Temperature Cofired Ceramics) - Tapes for Mechanical Application. In *IEEE Proc. of 30th International Spring Seminar on Electronics Technology (ISSE)*, pages 59–64, May 2007.

[55] G. Miskovic, L. Vuckovic, J. Fernandez, H. Homolka, M. Unger, and G. Radosavljevic. Investigation on Physical and Electrical Behaviour of LTCC Dielectric Tapes. In *IEEE Proc. of 37th International Spring Seminar on Electronics Technology (ISSE)*, pages 237–242, May 2014.

[56] M. Franz, I. Atassi, A. Maric, B. Balluch, M. Weilguni, W. Smetana, C.P. Kluge, and G. Radosavljevic. Material characteristics of the LTCC base material CeramTape GC. In *IEEE Proc. of 35th International Spring Seminar on Electronics Technology (ISSE)*, pages 276–281, May 2012.

[57] M. Unger, J. Fleig, M. Ahrens, W. Smetana, and G. Radosavljevic. Permittivity and conductivity of various LTCC tapes at high temperature. In *IEEE Proc. of 33rd International Spring Seminar on Electronics Technology (ISSE)*, pages 93–98, May 2010.

[58] James F. Shackelford and Robert H. Doremus. *Ceramic and Glass Materials: Structure, Properties and Processing*. Springer, 2007.

[59] L. J. van der Pauw. A method of measuring specific resistivity and hall effect of discs of arbitrary shape. Technical Report 13, Philips, 1958.

[60] G. Fasching. *Werkstoffe für die Elektrotechnik*. Springer, 1984.

[61] S. Berberović. *Teorijska elektrotehnika: odabrani primjeri*. Graphis Zagreb, 1998.

[62] Patrick Gonord and Siew Kan. Twin–horseshoe resonator—An investigation. *Review of Scientific Instruments*, 65(2):509–510, 1994.

[63] COMSOL AC/DC Module User's Guide. Technical report, Comsol AB., 2010.

[64] A. Buttari A. Guermouche G. Joslin J.-Y. L'Excellent X. S. Li A. Napov F.-H. Rouet M. Sid-Lakhdar S. Wang C. Weisbecker Agullo, P. Amestoy and I. Yamazaki. Recent Advances in Sparse Direct Solvers. In *22nd Conference on Structural Mechanics in Reactor Technology*, 2013.

[65] Luisier L. Kuzmin, A. and O. Schenk. Fast Methods for Computing Selected Elements of the Green's Function in Massively Parallel Nanoelectronic Device Simulations. In *19th International Conference on Parallel Processing (Euro-Par)*, pages 533–544, 2013.

[66] R. Nopper, Niekrawietz, and L. R., Reindl. Wireless readout of passive lc sensors. *In IEEE Trans. on Ins. and Meas.*, 59(9), 2010.